GAIT OPTIMIZATION FOR MULTI-LEGGED WALKING
ROBOTS, WITH APPLICATION TO A LUNAR HEXAPOD

A DISSERTATION

SUBMITTED TO THE DEPARTMENT OF AERONAUTICS AND
ASTRONAUTICS

AND THE COMMITTEE ON GRADUATE STUDIES

OF STANFORD UNIVERSITY

IN PARTIAL FULFILLMENT OF THE REQUIREMENTS

FOR THE DEGREE OF

DOCTOR OF PHILOSOPHY

Daniel Chávez-Clemente

January 2011

I certify that I have read this dissertation and that, in my opinion, it is fully adequate in scope and quality as a dissertation for the degree of Doctor of Philosophy.

_____

(Stephen M. Rock)   Principal Adviser

I certify that I have read this dissertation and that, in my opinion, it is fully adequate in scope and quality as a dissertation for the degree of Doctor of Philosophy.

_____

(J. Christian Gerdes)

I certify that I have read this dissertation and that, in my opinion, it is fully adequate in scope and quality as a dissertation for the degree of Doctor of Philosophy.

_____

(Jean Claude Latombe)

Approved for the University Committee on Graduate Studies

_____

Abstract

The interest in using legged robots for a variety of terrestrial and space applications has grown steadily since the 1960s. At the present time, a large fraction of these robots relies on electric motors at the joints to achieve mobility. The load distributions inherent to walking, coupled with design constraints, can cause the motors to operate near their maximum torque capabilities or even reach saturation. This is especially true in applications like space exploration, where critical mass and power constraints limit the size of the actuators. Consequently, these robots can benefit greatly from motion optimization algorithms that guarantee successful walking with maximum margin to saturation.

Previous gait optimization techniques have emphasized minimization of power requirements, but have not addressed the problem of saturation directly. This dissertation describes gait optimization techniques specifically designed to enable operation as far as possible from saturation during walking. The benefits include increasing the payload mass, preserving actuation capabilities to react to unforeseen events, preventing damage to hardware due to excessive loading, and reducing the size of the motors.

The techniques developed in this work follow the approach of optimizing a reference gait one move at a time. As a result, they are applicable to a large variety of purpose-specific gaits, as well as to the more general problem of single pose optimization for multi-limbed walking and climbing robots.

The first part of this work explores a zero-interaction technique that was formulated to increase the margin to saturation through optimal displacements of the robot's body in 3D space. Zero-interaction occurs when the robot applies forces only

to sustain its weight, without squeezing the ground. The optimization presented here produces a swaying motion of the body while preserving the original footfall locations. Optimal displacements are found by solving a nonlinear optimization problem using sequential quadratic programming (SQP). Improvements of over 20% in the margin to saturation throughout the gait were achieved with this approach in simulation and experiments. The zero-interaction technique is the safest in the absence of precise knowledge of the contact mechanical properties and friction coefficients.

The second part of the dissertation presents a technique that uses the null space of contact forces to achieve greater saturation margins. Interaction forces can significantly contribute to saturation prevention by redirecting the net contact force relative to critical joints. A method to obtain the optimal distribution of forces for a given pose via linear programming (LP) is presented. This can be applied directly to the reference gait, or combined with swaying motion. Improvements of up to 60% were observed in simulation by combining the null space with sway.

The zero-interaction technique was implemented and validated on the All Terrain Hex-Limbed Extra-Terrestrial Explorer (ATHLETE), a hexapod robot developed by NASA for the transport of heavy cargo on the surface of the moon. Experiments with ATHLETE were conducted at the Jet Propulsion Laboratory in Pasadena, California, confirming the benefits predicted in simulation. The results of these experiments are also presented and discussed in this dissertation.

Acknowledgments

Although this thesis shows my name as the single author, many people have contributed to making it possible and have made my time at Stanford a great adventure.

First I would like to acknowledge the important role of my adviser, Steve Rock. From him I have learned many technical and non-technical things, most importantly how to be an independent researcher. I especially admire his patience, and his resolve to motivate students to strive for excellence and integrity in their work. Working with him has been a faaan-tastic learning experience. Next, I wish to thank the other members of my reading committee: Chris Gerdes and Jean-Claude Latombe, who took time out of their busy schedules to read this thesis and provide insightful feedback. I also thank Prof. Monic Sun for agreeing to chair my oral defense.

This work would literally not have been possible without the interest and support of the people in the Intelligent Robotics Group at NASA Ames Research Center. Terry Fong gave me the opportunity to fulfill my dream of working at NASA, and diligently cut through the layers of red tape to make it happen. He also took the time to participate in my oral defense committee. Vytas SunSpiral welcomed me into the ATHLETE FootFall project, and became a great mentor and friend. His infectious enthusiasm, creativity, and passion for life multiplied my joy of being at NASA manyfold. DW Wheeler did a terrific job at leading the FootFall project during the later part of my time at Ames, and helped with code and logistics for my thesis experiments. Together we learned a lot about robots in the real world. My research also benefited from collaboration with Tristan Smith, Javier Barreiro, David Smith and Jeremy Frank of the Planning and Scheduling Group at NASA Ames.

At JPL I had the fortune of collaborating with Dave Mittman, who spent many

me from naming here individually, I offer a big, heartfelt Thank You.

☽

The inspiration to pursue this PhD came to me initially on July 4, 1997, at around midnight. The specific event that triggered it was the landing of the Pathfinder spacecraft on Mars, which I followed live on CNN as it unfolded. I was irrevocably bitten by the space bug when some of the first images arrived, showing the Sojourner rover descending to the surface and making the first-ever wheel tracks on Mars. It seems fitting to start this thesis with the image that first got me on this exciting path. Perhaps one day this work might contribute to making the first robotic footprints on another planet.

Contents

List of Tables

List of Figures

Nomenclature

$\{W\}$	World frame of reference
$\{R\}$	Robot frame of reference
$\{L\}$	Leg frame of reference
$\{T\}$	Tool frame of reference
$\vec{r}_{0,i}, \vec{r}_{f,i}$	Position of foot i before and after sag, in $\{W\}$
$\vec{r}_{0,CG}, \vec{r}_{f,CG}$	Position of the center of mass before and after sag, in $\{W\}$
$\Delta\vec{r}_i, \Delta\vec{r}_{CG}$	Displacement of foot i and the CG due to sag
K_{inv}	Diagonal contact stiffness matrix
k_{xx}, k_{yy}, k_{zz}	Contact spring constants in the x, y, z directions
n	Total number of legs
n_c	Number of feet in contact
$\rho_{max,i}$	Maximum reach for leg i at the current body position
$\vec{\rho}_i$	Location of the foot relative to the leg's joint i, in {L}
x_b, y_b, z_b	Position of the robot's body expressed in the World frame
ϕ_b, θ_b, ψ_b	Orientation (roll, pitch, yaw) of the robot's body
$\Delta x_b, \Delta y_b, \Delta z_b$	Change in position of the robot's body for optimization purposes
$\Delta\phi_b, \Delta\theta_b, \Delta\psi_b$	Change in body orientation (roll, pitch, yaw)
J	Optimization cost function OR
	Jacobian matrix for a robotic leg
$\tau_{\%i}$	Torque ratio (percentage) of joint i
$\hat{z}_i$	The z axis of joint i – for revolute joints it is also
	the axis of rotation
$\tilde{S}_i$	Screw for joint i
ρ_i	Location of the foot relative to joint i, expressed in {L}
$S_{i,j}$	Sensitivity of joint i's torque to variations in force j
$S_{\%i,j}$	Sensitivity of $\tau_{\%i}$ to variations in force j
θ	A parameter for NESM calculation, see Equation 3.7
γ	A parameter for NESM calculation, see Equation 3.8
ε	Specific resistance

g	Gravity constant
m	Robot mass OR
	Number of joints per leg
P	Power
R	Leg stroke
K_m	Kinematic margin
λ	Robot's stride
σ	Length of a body shift
β_i	Duty factor of leg i
ϕ_i	Phase of leg i (not to be confused with the roll angle ϕ_b)
Δh_i	Distance that a foot has been lifted from its original position
$\vec{r}_{C,i}(z)$	Position of contact point i, in $\{W\}$
Φ	Matrix formed of n_c 3×3 identity matrices, see Equation 2.23
C_i	Cross-product matrix, see Equation 2.27
Γ	Balance matrix, resulting from stacking the Φ and C matrices. See Equation 2.29

Abbreviations

AP	Ankle Pitch joint
AR	Ankle Roll joint
ATV	All-Terrain Vehicle
ARC	Ames Research Center
ATHLETE	All Terrain Hex-Limbed Extra-Terrestrial Explorer
CG	Center of Gravity
CM	Center of Mass
CGU	Carnegie Mellon University
CPS	Conservative Polygon of Support
CPG	Central Pattern Generator(s)
DFS	Depth First Search

DOF	Degree(s)-Of-Freedom
EAP	Education Associates Program (at NASA Ames)
EKF	Extended Kalman Filter
ESM	Energy Stability Margin
FPS	Full Polygon of Support
GUI	Graphical User Interface
IK	Inverse Kinematic(s)
IMU	Inertial Measurement Unit
IRG	Intelligent Robotics Group (at NASA Ames)
JPL	Jet Propulsion Laboratory
LM	Levenberg-Marquardt
LP	Linear Program(ming)
LQR	Linear Quadratic Regulator
NASA	National Aeronautics and Space Administration
NESM	Normalized Energy Stability Margin
ODE	Open Dynamics Engine
POS	Polygon of Support
PQP	Proximity Query Package
PRM	Probabilistic Road Map
PS	Polygon of Support
SBL	Single-Query Bi-Directional Probabilistic Roadmap Planner with Lazy Collision Checking
SNOPT	Sparse Nonlinear OPTimizer
SQP	Sequential Quadratic Programming
SSM	Static Stability Margin
UNC	University of North Carolina

Leg Joints

HY	Hip Yaw joint

HP	Hip Pitch joint
KP	Knee Pitch joint
KR	Knee Roll joint
AP	Ankle Pitch joint
AR	Ankle Roll joint

Internal Components of the Leg Joints

MT	Motor Tube
M	Motor
P	Planetary Reduction Stage
B	Magnetic Brake
E+	Incremental Encoder
HD	Harmonic Drive
FS	Flexspline (of harmonic drive)
WG	Wave Generator (of harmonic drive)
CS	Circular Spline (of harmonic drive)
CT	Coupling Tube
C	Coupling between motor and harmonic drive
OT	Output Tube
Ea	Absolute Encoder

Chapter 1

Introduction

This chapter introduces walking robots and describes the problems addressed in this work.

§**1.1** motivates the use of walking robots.

§**1.2** outlines the history of development of walking robots and gaits.

§**1.3**-**1.4** discuss the advantages and disadvantages of walking robots.

§**1.5** outlines the problem addressed in this work and why it is important.

§**1.6** summarizes the main contributions of this research.

§**1.7** provides an outline of the rest of this thesis.

The focus of this dissertation is the development of gait optimization techniques to prevent joint saturation in legged robots. The problem of saturation is encountered when the torque or force demanded from the actuators reaches or exceeds their maximum capacity.

The use of walking machines is interesting for various applications, including cargo transport, entertainment, education, land mine removal, forestry and space exploration. Their versatility allows them to access challenging terrains with minimum impact and high safety. Many of these applications are likely to cause saturation, for example when they are used to transport heavy cargo (e.g. [Wilcox 07]). Even robots that do not normally operate at the limit of saturation can benefit from gaits that place lower demands on their motors. Potential benefits include higher payload, increased durability, better reaction to unsafe conditions like slippage, and the

possibility of using smaller motors.

The remainder of this chapter will discuss the motivation for developing and using walking robots, some of their limitations, and an outline of the problems being addressed in this dissertation.

1.1   Why Use Walking Robots?

Walking robots have many desirable characteristics. They are capable of omnidirectional motion without the need for turn-in-place maneuvers. Their variable geometry allows them to fit through tight spaces or fold compactly for transportation in small vehicles (a useful capability in space exploration). They also benefit from a lower impact on the terrain because they progress via discrete contacts instead of a continuous track. This is especially important in dangerous environments like mine fields, or where it is essential to keep the terrain largely undisturbed for scientific reasons. One of their most useful characteristics is their versatility to access a wide variety of terrains. Boulder fields, steep slopes and loose, sandy areas can all be traversed by walking, in addition to any location accessible to wheeled vehicles.

Because of these benefits, suitable applications for walking robots include land mine removal, planetary exploration, forestry, cargo transport on rugged terrain, entertainment, and personal assistance in home or office environments. Figure 1.1 shows three examples of walking robots developed for space exploration, de-mining and forestry applications.

| (a) Space (ATHLETE) | (b) De-mining (SILO 6) | (c) Forestry (Timberjack) |

Figure 1.1:   **Three applications of walking robots.**

An increasing amount of collaboration between biologists and roboticists has improved the understanding of legged locomotion, and provided inspiration for the design of new robots. For example, biological research on the locomotion of cockroaches has revealed that leg springiness plays the important role of passively compensating for external disturbances that knock the insect out of stride [Full 02]. As a result, successful motion in challenging situations is possible without the intervention of a powerful brain. The lesson has been incorporated into the design of RHex [Altendorfer 01], a running hexapod with compliant 1-degree-of-freedom (*DOF*) legs (Figure 1.2).

Figure 1.2: **The RHex robotic platform, a biologically inspired walking robot (Credit: Kod*lab, Univ. of Pennsylvania).**

Another example is the work of McGhee and Frank on the stability properties of quadrupedal machines [McGhee 68b]. Their research found that a certain class of gaits referred to as "wave gaits" maximizes stability along the direction of motion (longitudinal stability). Interestingly, this type of gait is commonly used by 4-legged animals during slow walking, suggesting that nature sometimes favors stability over other possible benefits like energy conservation.

1.2 Historical Sketch of Walking Robots

Undoubtedly the interest in understanding and replicating walking locomotion has existed for a very long time. According to Zielinska [Zielinska 04] historical evidence of this interest dates back to antiquity, in the form of descriptions of mechanical

elephants in India and a variety of articulated toys and decorative figures from Egypt (circa XX century B.C.) and Greece (III century B.C.).

The earliest walking machine designed for a practical application appears to be the Steam Man of Dederick and Grass [Dederick 68], shown in Figure 1.3. Patented and actually built in 1868, the Steam Man was attached to the front of a carriage and pulled it by means of steam power. It was kept balanced by the support structure attaching it to the carriage, and the inventors estimated that their contraption would be capable of speeds of up to $60\frac{mi}{hr}$:

> "As the engine is capable of making more than a thousand evolutions a minute, it would get over the ground, on this calculation, at the rate of a little over a mile a minute. As this would be working the legs faster than would be safe on uneven ground or on broad street cobble stones, it is proposed to run the engine at the rate of five hundred revolutions per minute, which would walk the man at the modest speed of half a mile a minute." — Zadock Dederick, in a 1868 interview with the Newark (N.J.) Advertiser [Buckley 07]
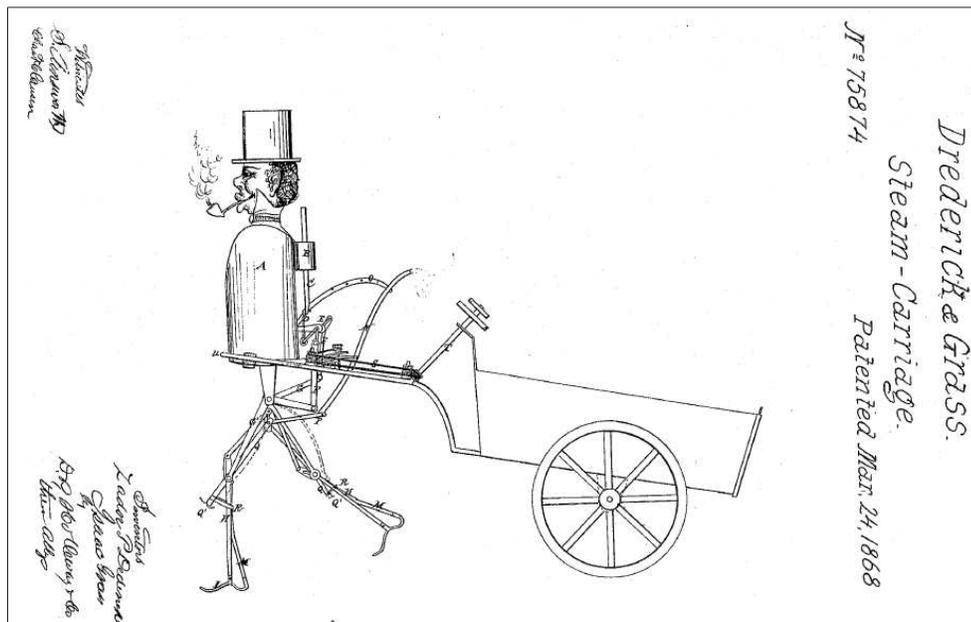
Figure 1.3: **The Steam Man of Dederick and Grass.** *From US Patent 75874 [Dederick 68]*

It is not clear how far Dederick and Grass took their invention, but they seem to have inspired other people to develop similar machines. They envisioned a variation in the form of a Steam Horse, which according to them would "do the duty of twelve ordinary creatures of the same species". The design for such a machine was patented by L.A. Rygg in 1893 [Rygg 93], and is shown in Figure 1.4. Rygg's mechanical horse was to be human-powered, and although it was never built there seems to be a consensus that it constitutes the first design of a quadrupedal mobile machine.
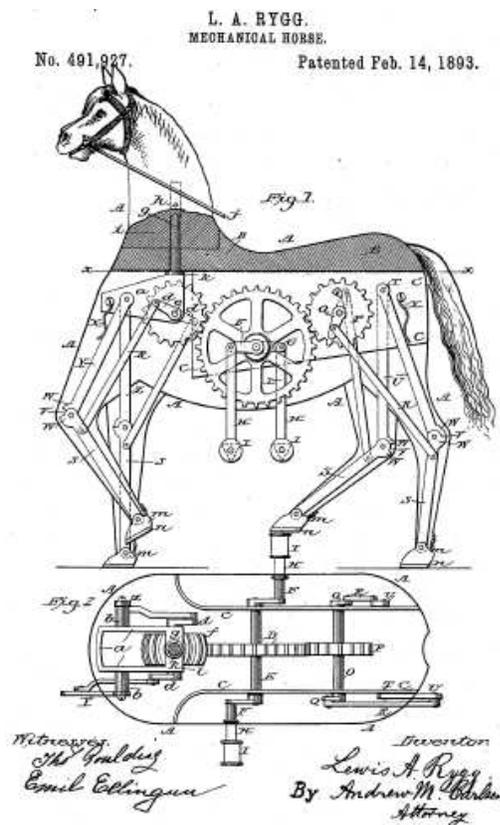
Figure 1.4: **The Mechanical Horse of L.A. Rygg.** *From US Patent 491927 [Rygg 93]*

Between the late 1800's and the mid 1900's the construction of walking machines did not progress much. On the other hand the formal study of gaits got truly underway with the pioneering efforts of Eadweard Muybridge, a photographer born in England who lived for many years in the American west. Muybridge was well known in California as a landscape photographer. According to his biographers (e.g.
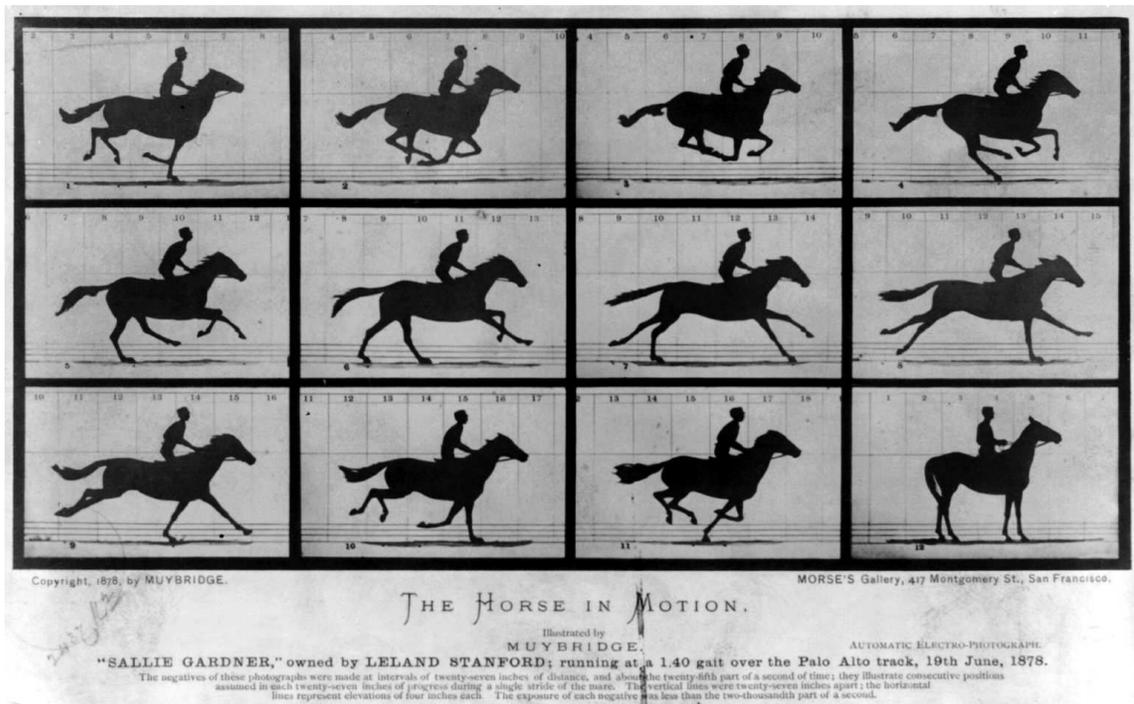
Figure 1.5: **The Horse in Motion, by E. Muybridge** *(now public domain).*

[Solnit 04]), he was recruited in 1872 by Leland Stanford – former governor of Califor-
nia and founder of Stanford University – to help settle a popular question at the time:
whether the hooves of a horse ever leave the ground all at the same time. Muybridge
developed techniques to photograph Stanford's own galloping horse at a high frame
rate, and found that there were indeed intervals when all of the horse's hooves were
in the air (Figure 1.5). Having perfected these photographic techniques, Muybridge
embarked on further studies of animal locomotion, including a more comprehensive
look into horses, bisons and people [Muybridge 87, Muybridge 57]. His photographic
sequences remain useful references in the study of gaits.

The mathematical study of gaits was pioneered in the 1960's by Tomovic and
Karplus [Tomovic 61]. Shortly thereafter Hildebrand [Hildebrand 65] created the con-
cept of the *gait formula* to be discussed in §3.5, which was later perfected by McGhee
[McGhee 68a]. Also in this period the discovery of the stability optimality of wave
gaits was made by McGhee and Frank [McGhee 68b].

In the meantime, the development of walking machines acquired new momentum, spurred partly by the advances in computer technology brought about by the space program. It is hardly surprising that the creation of the first truly successful walking robots had to wait until the advent of modern computers, given the complexity of the mechanisms and the coordination required for their motion. Notable robots from this period include the Iron Mule Train [Morrison 68], the GE Walking Truck [Mosher 68], the Phoney Pony [McGhee 67] and the Big Muskie [Cox 70].

The 1970's and 1980's saw further advances in robot development and gait studies. The first bipedal robot – WABOT 1 – was created by Kato around 1973 [Kato 73]. With biped robots came the need to formalize the study of dynamic stability, and in 1972 Vukobratovic introduced the concept of Zero Moment Point *(ZMP)*, which has remained an essential tool in the study of biped locomotion [Vukobratovic 04].

Multi-legged robots also moved forward – the first European walking robot was developed at the University of Rome in 1972 [Petternella 74], and others were built in Russia as well [Okhotsimski 79, Okhotsimski 80]. In the United States, the OSU Hexapod was created in 1977 by McGhee [McGhee 79], followed by the much larger Adaptive Suspension Vehicle by Waldron and McGhee in 1985 [Waldron 86b]. In Japan, Hirose developed the PV II, a sophisticated quadruped which was the precursor of the impressive Titan family of robots still under development at the Tokyo Institute of Technology [Hirose 85, Hirose 91, Hirose 99, Kato 01]. Gait study benefited from the introduction and development of *free gaits* by Kugushev and Jaroshevskij [Kugushev 75], and *adaptive gaits* by Kumar and Waldron [Kumar 89].

An enormous body of research has been generated thereafter. The main developments after the 1990's have focused primarily on biped locomotion, dynamic walking and running, with an emphasis on surmounting the speed and efficiency disadvantages that affect walking robots. Research on new types of actuators like artificial muscles has also received significant attention.

More details on the history of walking robots can be found in the publications by Song and Waldron [Song 89], Zielinska [Zielinska 04], González de Santos et al. [de Santos 06], and Liu et al. [Liu 07]. A good overview of the history of bipeds is also provided in [Siciliano 08], Chapter 16.

1.3 Advantages of Walking Robots

Legged robots have many characteristics desirable for terrestrial and space applications, including omnidirectional motion, variable geometry, discrete contact points, access to diverse terrain and unique modes of locomotion.

Omnidirectional Motion

Wheeled rovers, like automobiles, are subject to non-holonomic motion constraints. This restricts them to move in certain directions permitted by the alignment of their wheels, and limits the trajectories that they are able to follow. The addition of degrees of freedom (DOF) through independently steerable or omnidirectional wheels can help alleviate this problem to some extent, but the motion might still require in-place turning, and in the case of omni wheels the possibility of roller jamming caused by debris can easily arise.

In contrast, legged robots can be designed to be inherently omnidirectional, by incorporating sufficient degrees of freedom per leg. As a result, they are able to accelerate in any direction as long as the legs remain within their geometric and torque constraints. This added versatility can facilitate traversal of challenging terrain by following any path necessary.

Variable Geometry

The legs of a walking robot change geometry as the joint angles are varied. As a result, the configuration of the robot is very adaptable and can help it fit through tight spaces, such as when walking through a canyon or forest. It also enables a very large robot to fold compactly for transportation, an ability that is essential in planetary exploration where the robot must fit inside the launch vechicle's payload compartment.

This is illustrated in Figure 1.6, which shows the TriATHLETE robot developed by NASA for heavy cargo transport on the moon. The robot is nearly 4m tall when deployed, but is able to fit atop the lunar lander by folding its legs tightly. Once on the moon it can self-deploy by re-extending its legs and stepping off the lander.

Figure 1.6: **The TriATHLETE robot unfolding from a compact configuration atop a prototype of a lunar lander** *(Credit: David Mittman, JPL)*

Discrete Contact Points

Walking robots propel themselves by making contact with the ground at discrete contact points along their path, instead of leaving behind continuous tread marks characteristic of rolling. This can be advantageous for a number of reasons.

Figure 1.7 shows the SILO 6 robot, developed for the detection of buried land mines. This application clearly benefits from a discontinuous contact pattern because the robot can place its feet at carefully selected locations to avoid triggering a mine. Thus an entire field can be surveyed robotically without danger to people.

Discrete contacts are also essential for traversing dense boulder fields, where stepping on rocks might be unsafe.

Finally, when exploring locations where the terrain itself is a target of scientific interest, it is convenient to disturb it as little as possible. This can easily be accomplished with legged robots.

Figure 1.7: **The SILO 6 robot with a scanning manipulator for land mine detection** *(Credit: Center for Automatic Control, Spain)*

Access to Diverse Terrain

Perhaps the main advantage of legged robots over their wheeled counterparts is their ability to explore a wide variety of easy and challenging terrains. Any ground accessible to wheeled rovers is also traversable by legged ones. Additionally, cluttered environments, boulder fields, steep slopes, soft sand and even walls can be accessed by means of limbs. The diversity of terrains that are potentially encountered on other planetary bodies (Figure 1.8) makes walking robots particularly attractive for space exploration.

(a) Lunar landscape at the Apollo 17 landing site

(b) Martian landscape near the Pathfinder landing site
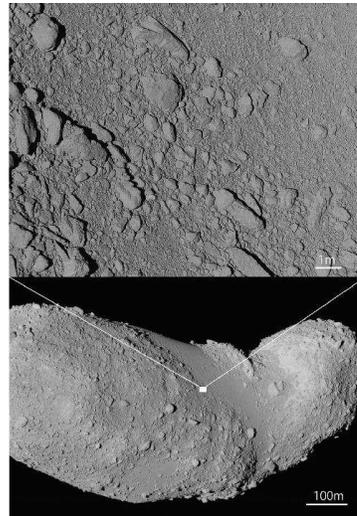
(c) Asteroid Itokawa photographed by the Hayabusa spacecraft

Figure 1.8: **Diverse terrains encountered in planetary exploration** *(Credit: NASA, JAXA)*

Unique Modes of Locomotion

The possibility of combining legs and wheels has already been exploited in a number of robots. The wheels can be actuated or passive, resulting in unique modes of locomotion. For example, Hirose and Takeuchi [Hirose 95] developed the Roller-Walker hybrid robot shown in Figure 1.9. The robot is equipped with passive wheels and an ingenious mechanism to rotate their axle 90° so that one side of the wheel is in contact with the ground and functions as a regular foot. In this configuration the robot behaves as a walker. If the wheels are rotated to the rolling position, the robot moves forward by a skating motion. This type of locomotion is only possible because of the wheel-leg combined design.

For legged robots equipped with actuated wheels, a combined walking+rolling motion is possible. In this mode some or all the wheels can provide traction, while the legs change shape to avoid obstacles by either making the wheel drive around them or picking up the foot to go over. Terms like *rollking* have been coined to describe this mode of locomotion, which combines the speed and efficiency advantages of rolling with the versatility of robotic legs.
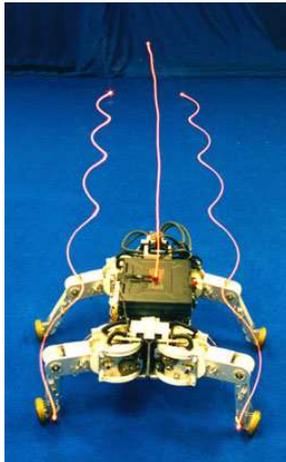
Figure 1.9:   **The Roller-Walker hybrid robot has passive wheels and can move by rollerblading** *(Credit: Hirose-Fukushima Robotics Lab)*

1.3.1 Applications of Walking Robots

The special characteristics of walking robots mentioned above make them well suited for many applications. Below are some examples of legged robots that have been developed for a variety of missions.

Land Mine Detection and Removal

Manual detection and removal remains the leading technique for clearing land mines from locations around the world. This is a slow process that carries a very high risk for humans. Legged robots are particularly well suited for this application.

As previously mentioned, they are able to place their feet at carefully selected points on the ground, and can be equipped with adequate sensors for detecting the mines. These can then be destroyed by the robot itself by a number of different approaches.

Robotic de-mining practically eliminates all risk for human operators, and the process can be sped up by using multiple robots simultaneously. Some robots are being developed for this purpose. Figure 1.7 shows the SILO 6, under development by the Department of Automatic Control of the Spanish CSIC [Cobano 08]. The Tokyo Institute of Technology is also experimenting with the Titan VIII robot [Hirose 98], and its specialized successor – the Titan IX [Kato 01]– both shown in Figure 1.10.
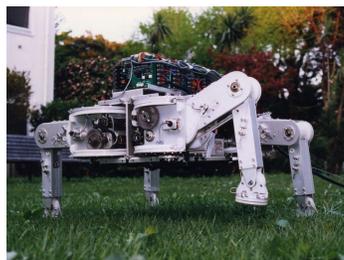
(a) Titan VIII   (b) Titan IX

Figure 1.10: **Legged robots for de-mining applications** *(Credit: Hirose-Fukushima Robotics Lab)*

Forestry

Forest management includes activities such as timber harvesting, which often takes place in remote locations that are difficult to access. An option is to create roads for trucks and other vehicles to reach the areas of interest, but this has a higher impact on the forest because it requires removal of trees that would otherwise not be harvested. An alternative is to use legged robots, because they can traverse the difficult and cluttered terrain separating a road from an area of interest.

The Finnish company Plustech Oy (now part of John Deere) developed the Timberjack precisely for this application (Figure 1.11). The robot is powered by hydraulic actuators and can transport downed trees using its crane boom.

Figure 1.11: **A legged robot for forestry applications** *(Credit: John Deere)*

Military Cargo Transport

The idea of using legged robots as cargo "mules" is also actively being explored. A quadruped called Big Dog has been developed by Boston Dynamics to assist soldiers in carrying equipment out on the battlefield [Playter 06]. Its successor, LS3, is currently under development and is intended to carry up to 180 kg of payload (Figure 1.12)

Entertainment and Education

Legged robots have also successfully entered the realm of entertainment. The Aibo is a well known robotic pet developed by Sony (Figure 1.13(a)), and has become

Figure 1.12: **The LS3 military cargo robot** *(Credit: Boston Dynamics)*

popular not only as a toy but also a research and education testbed. A version of the famous RoboSoccer tournament is played with these robots, which offer interactive capabilities for research on sensing, planning and mobility.

Sony also developed QRIO, a small humanoid robot with voice and video sensing as well as very good mobility (Figure 1.13(b)). Although never commercialized by Sony, similar robots are under development by other companies and will soon enter the market.

A third example, the PLEO "robotic companion" from Innvo Labs (Figure 1.13(c)) is an interactive robot dinosaur designed to function as a pet. The robot is capable of visual, audio and infrared sensing, as well as exhibiting different pre-programmed and customizable personality traits. A growing community of developers exists who use the PLEO in artificial intelligence research.

(a) Sony Aibo   (b) Sony QRIO   (c) Innvo Labs PLEO

Figure 1.13: **Entertainment and educational robots** *(Credit: Sony, Innvo Labs)*

Personal Assistants

Because of their ability to move in cluttered environments, walking robots are being considered as home or office assistants to perform a variety of tasks. These include domestic chores like cleaning, carrying and delivering packages, and assisting handicapped and elderly people in their daily lives.

Humanoid robots, like the Honda Asimo (Figure 1.14(a)), have been under development for many years, and are gradually achieving the necessary level of maturity to perform well in domestic environments. Multi-legged robots are also being developed. For example, the ZeroCarrier from the Tokyo Institute of Technology (Figure 1.14(b)) is capable of ascending and descending stairs with a person on top.

(a) ASIMO humanoid robot

(b) ZeroCarrier stair climber

Figure 1.14: **Personal assistant robots** *(Credit: Hirose-Fukushima Robotics Lab, Honda)*

Planetary Exploration

Space agencies have considered legged robots for planetary exploration missions due to their high versatility. The designs vary in complexity, including for example the Canadian Space Agency's simple wheel-leg rover Prompt (Figure 1.15(a)), NASA's large and complex ATHLETE cargo robot (Figure 1.15(b)), the versatile walking/climbing Lemur robot also from NASA (Figure 1.15(c)), and the German Aerospace Center's highly sophisticated Crawler (Figure 1.15(d)). While no legged robots have thus far ventured into space, advances in their development will undoubtedly make them strong contenders as primary or secondary payloads in the future.

(a) Prompt (CSA)

(b) ATHLETE (NASA)

(c) Lemur (NASA)

(d) Crawler (DLR)
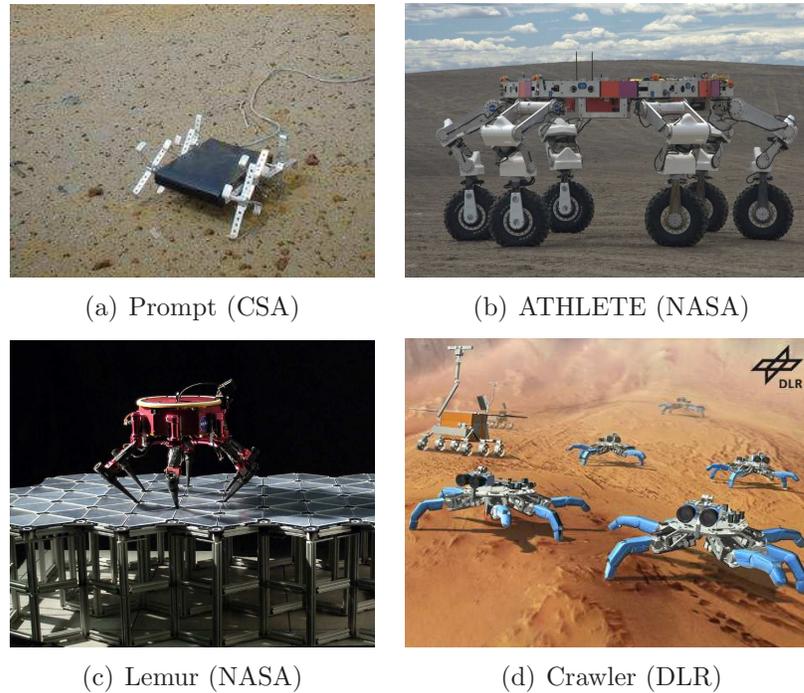
Figure 1.15: **Some robots designed for planetary exploration.** *Credit: CSA, NASA, DLR*

1.4   Disadvantages of Walking Robots

The above applications are very compelling, but challenges remain before walking robots can see a more widespread use. Some of their current disadvantages include higher complexity and cost, low energy efficiency, and low speed.

High Complexity and Cost

Walking robots are complex and expensive machines with many static and moving parts. Each leg is usually composed of several rigid elements connected by articulated joints. The joint assemblies can be fairly complex mechanical systems, consisting of actuators, sensors, transmission gears and supporting structure.

Because of the many DOF, motion planning and execution are quite involved for a walking robot. For example, moving forward in a straight line requires execution of a sequence of steps and body shifts. These moves require careful planning to take the legs safely through the necessary configurations, as exemplified in Figure 1.16.

As the number of DOF grows the computational cost increases.
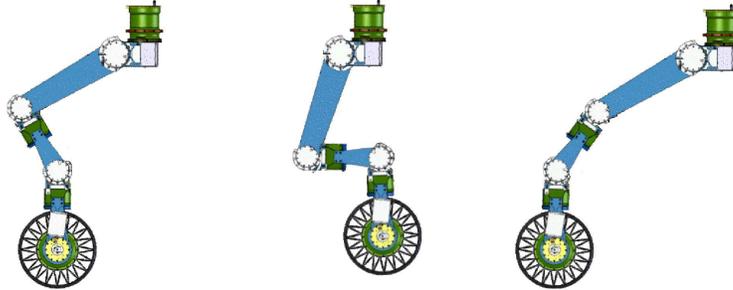
Figure 1.16: **A robot's leg must move through a sequence of configurations to execute a step.**

Another source of complexity is the possibility of *motor saturation*. The consequences of saturation can be serious, ranging from interrupted motion to robot instability and hardware damage. In addition to this, if the objective of the robot is to transport cargo, actuator limitations are critical because they establish an upper bound on the payload mass that can be successfully carried.

The need to prevent saturation greatly complicates the planning process, and requires special motion techniques that are the focus of this dissertation.

Low Energy Efficiency

Efficiency estimates for several walking and driving machines have revealed that walking is less energy-efficient on benign terrain than rolling. To enable comparison of diverse modes of locomotion, Gabrielli and von Kármán [Gabrielli 50] introduced the concept of specific resistance as a metric of energy efficiency, a concept later extended by Gregorio et al. [Gregorio 97] to allow comparisons at different speeds. [1]

---

[1]Specific resistance is a dimensionless quantity computed as the power required (P) divided by the product of weight times speed (mgv):

$$\varepsilon = \frac{P}{mgv}$$

Since the ratio of power to speed $\frac{P}{v}$ represents a force known as the *tractive force*, specific resistance is the tractive force per unit of weight. A lower value of ε means less power is required to move at a given speed, for some given vehicle mass. Since lower ε corresponds to more efficient locomotion, this metric represents the equivalent of a drag coefficient, hence the name "resistance".
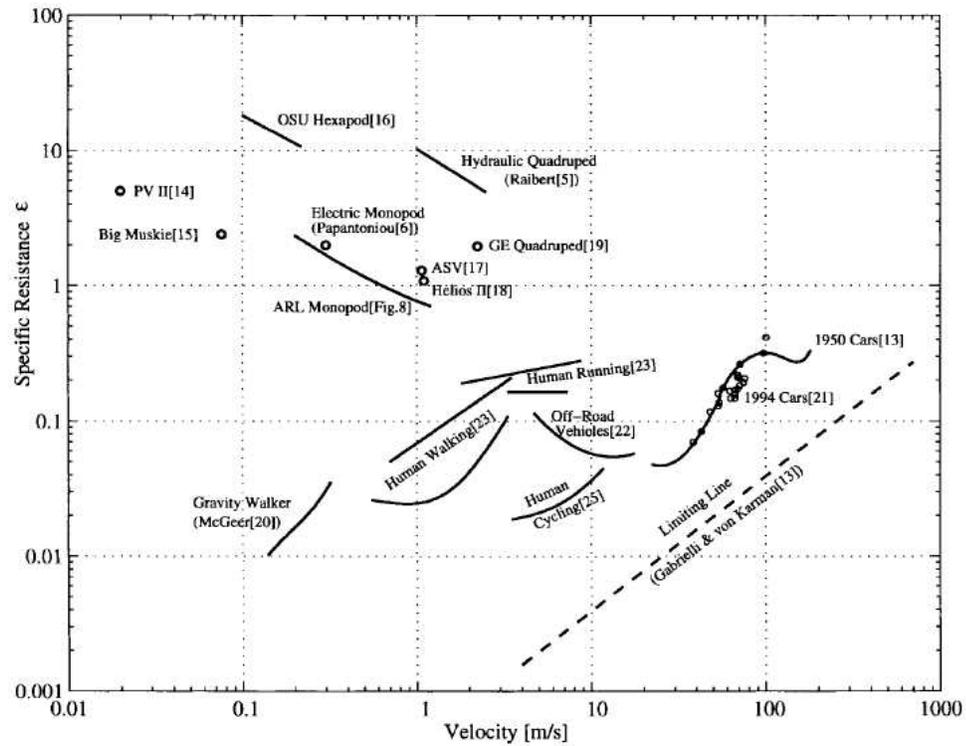
Figure 1.17: **The specific resistance of various machines as a function of speed (from [Gregorio 97]).**

Gregorio used this metric to compare the efficiency of several wheeled and legged vehicles at various speeds of their operational envelopes. The results are summarized in Figure 1.17. Here, more efficient locomotion is toward the bottom of the plot. Points near the bottom right represent very fast and efficient locomotion, and are very desirable. Cars lie in the proximity of this region, while legged robots are closer to the top left (slow and inefficient). In spite of this, the large payoffs that can be obtained from legged robots motivate their continued development.

Low Speed

Referring again to Figure 1.17, it is possible to see that all walking robots developed to date fall in the "very slow" category comparatively speaking (that is, near the left half of the plot).

(a) Petman – $7.1\frac{km}{h}$

(b) Shelley – $100 - 200\frac{km}{h}$

(c) ATHLETE – $0.006\frac{km}{h}$

(d) MER – $1.8\frac{km}{h}$
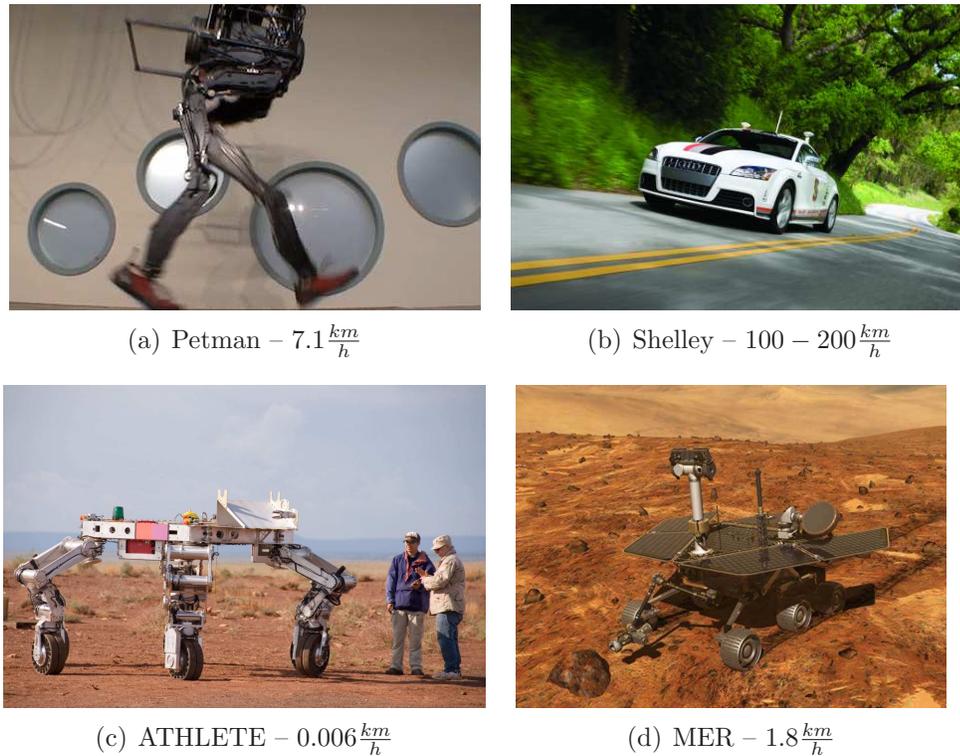
Figure 1.18: **Speed comparison between wheeled and legged robots** *(Credit: Boston Dynamics, Stanford University's Dynamic Design Lab, NASA)*

An interesting quantitative comparison can be made with some specific examples, shown in Figure 1.18. As of October 2010, the fastest legged robot on Earth is Petman developed by Boston Dynamics, capable of running at $7.1\frac{km}{h}$. In contrast, Stanford University's autonomous car Shelley has demonstrated speeds in excess of $200\frac{km}{h}$ on the Salt Flats at Bonneville, and has successfully negotiated the challenging Pikes Peak hill climb at speeds surpassing those of many drivers [Blackman 10].

So far no legged robot has made the trip to another planet. However, test data available for the ATHLETE lunar robot sets its current walking speed at about $0.006\frac{km}{h}$. By comparison, the Mars Exploration Rovers are capable of $1.8\frac{km}{h}$.

Significant advances are required to improve the speed of legged machines. Dynamic walking and running have thus become popular areas of research, and certainly a main thrust in the development of legged robots. The fastest legged animal on Earth

– the cheetah – is capable of speeds as high as 120 $\frac{km}{h}$, and developing a robot able to move at similar speeds will likely remain an exciting challenge for years to come.

1.5   Research Motivation

The goal of this thesis is to develop techniques for optimizing the gait of a walking robot to prevent saturation with the largest margin possible. The benefit of maximizing the margin to saturation include:

- The payload that the robot can carry with a given set of actuators is maximized.

- Damage to the hardware due to over-torque situations is prevented.

- Actuation capabilities are preserved for the purpose of reacting to unexpected situations like foot slippage.

- The possibility of saturation due to unmodeled environment characteristics (e.g. bumps, slopes) is reduced.

- Useful information is obtained about the lower bound of actuation with which a gait can be executed. This translates into the smallest motors that can potentially be used on the robot.

Depending on the situation, different techniques can be pursued to maximize the margin to saturation. One possibility is to take advantage of the multiplicity of force combinations that satisfy static equilibrium (collectively referred to as a *null space*). This means that the robot can squeeze the ground or its own body to direct the net force at each foot in an optimal way relative to critical joints. Contrary to intuition, important torque reductions can be obtained from using this null space of forces. Chapter 6 will describe a technique to find the optimal distribution of forces for statically-stable walking robots.

It is also possible to move away from saturation by displacing the robot's center of gravity (CG) to modify the vertical distribution of forces. In this case, a *zero-interaction* gait is executed. This means that no squeezing of the ground or chassis

takes place, and the vertical forces are adjusted by means of body offsets. The result is a zig-zagging motion of the body referred to as *sway*. Zero-interaction optimization is the safest alternative when the contact friction coefficient is unknown. Chapter 4 describes how the optimal displacements of the body are determined, and how they are applied to improve a reference gait.

In fact, body sway and null-space utilization can be combined to achieve the highest possible actuation margin for a given gait. This avenue is also explored in Chapter 6.

To guarantee that the full benefit of these optimization techniques is obtained, it is necessary to equip the robot with closed-loop force control capabilities so that the contact forces can be adjusted precisely. In the absence of force control the actual benefit is determined by a number of factors, including terrain characteristics, contact mechanics and transmission non-backdrivability. These issues are analyzed in Chapter 5.

1.6   Summary of Contributions

The research described in this dissertation makes the following main contributions to the field of gait generation for walking robots:

- Development and testing of a zero-interaction gait optimization technique that makes use of body sway to prevent joint saturation in walking robots. Improvements of $\geq 20\%$ in saturation margin were achieved in simulations and experiments with NASA's ATHLETE robot, a hexapedal wheel-in-leg rover for lunar exploration. The details of this technique are introduced in Chapter 4.

- Development of a gait optimization technique that takes advantage of the null space of ground contact forces. This technique determines the optimal force distribution via linear programming, and applies it to a reference gait by itself or in combination with body sway to maximize actuation margin. A total improvement of $\geq 60\%$ in actuation margin was observed in simulations of the

ATHLETE robot executing a reverse wave gait. This technique is described in Chapter 6.

- Development of a method to compute robot sag and contact forces simultaneously. The new technique allows accurate calculations with heterogeneous contact stiffnesses, and analysis of the gradual force redistribution that occurs during foot lifting and dropping transitions. The method is described in Chapter 2.

1.7   Organization of Dissertation

The rest of the dissertation is organized as follows:

Chapter 2 describes the ATHLETE robot testbed, and outlines the model and techniques used to compute contact forces and joint torques.

Chapter 3 outlines the process of gait generation and provides a detailed description of related work.

Chapter 4 discusses gait optimization under zero-interaction assumptions. A method to obtain optimal body displacements is presented, and its use for the purpose of optimizing the robot's gait to take advantage of sway is discussed. The chapter also presents simulation results for the ATHLETE robot.

Chapter 5 presents a sensitivity analysis and a discussion of the effects of contact force variations on joint saturation. Insights into how these variations translate into terrain characteristics are also provided. The analysis contained in this chapter is relevant to understand the impact that these external factors can have on the zero-interaction optimized gait in the absence of closed-loop force control.

Chapter 6 discusses gait optimization techniques that make use of the nullspace of contact forces to increase the margin to saturation further. A method to obtain the optimal force distribution for any given pose of the robot is presented. The

method can be applied directly to a reference gait, or combined with body sway for largest benefit. Both cases are discussed, and simulation results for the ATHLETE robot are presented.

Chapter 7 presents experimental results for the zero-interaction sway optimization technique on the ATHLETE robot. The experiments were conducted on the Mars Yard at the Jet Propulsion Laboratory in Pasadena, California, and confirmed the reduction in torque percentages achieved by body sway.

Chapter 8 summarizes the contributions and lessons learned, and describes avenues for future research.

Chapter 2

Description and Modeling of the Robot

This chapter describes the solution technique developed for force calculations on robots with compliant contact points, and explains the procedure to calculate joint torques. It also introduces the ATHLETE hexapod robot, which was the testbed for this research.

§**2.1** describes the ATHLETE robot.

§**2.2** follows with a discussion of the traditional technique for calculation of contact forces, and introduces a new method for simultaneous solution of forces and sag.

§**2.3** explains the method to compute joint torques.

§**2.4** explores the existence of nullspaces of forces and torques, with emphasis in the relation between the nullspace and the number of legs/DOF.

§**2.5** discusses future improvements that can be made to the model.

2.1   Testbed Description

The experiments presented in this thesis were conducted on JPL's All-Terrain Hex-Limbed Extra-Terrestrial Explorer (ATHLETE) robot (Figure 2.1). ATHLETE is a wheel-in-leg robot with six legs, designed to carry heavy cargo and crew members on the surface of the Moon. The total mass of the robot without payload is 895kg.

Each leg has six degrees of freedom and a wheel at the end, which can also be used to power tools using a mechanical adapter. The design of ATHLETE as a

Figure 2.1: **The ATHLETE robot at Moses Lake, WA. Note scale relative to operator.**

walker/roller allows it to traverse the entire spectrum of terrains it would encounter on the moon, using various modes of locomotion. The robot is capable of rolling like a standard rover in benign terrain, or applying the brakes and walking across difficult terrain. The joints of each leg are equipped with highly-geared electric motors in order to transmit sufficient torque while maintaining a reasonably small and lightweight design, a challenge that is common to all robots for space applications. The specifications of each joint are summarized in Table 2.1.

	Joint	Angle Limits		Gear	τ_{max}
		Min [°]	Max [°]	**Ratio**	[N-m]
1.	Hip Yaw (HY)	-100	220	13100:1	1530
2.	Hip Pitch (HP)	-90	90	13100:1	1530
3.	Knee Pitch (KP)	-200	155	6591:1	738
4.	Knee Roll (KR)	-115	115	3640:1	497
5.	Ankle Pitch (AP)	-110	110	4150:1	497
6.	Ankle Roll (AR)	-115	115	3640:1	497

Table 2.1: **Main specifications for the joints of an ATHLETE leg.**

2.1.1 Robot Sensing

Cameras

The sensor suite on ATHLETE includes a total of 11 stereo camera pairs, organized in three groups: 6 navcam pairs mounted on each of the six outside faces of the chassis, 3 hazcam pairs mounted on three non-consecutive internal corners of the chassis, and finally two toolcam pairs, mounted near the wheel of legs 1 and 6. The navcams are setup with overlapping fields of view in order to provide a full 360° coverage of the ground around the robot. The view provided by the navcams is most useful for driving because of the slightly higher aim. The hazcams look toward the inside of the robot and provide a view of the ground directly underneath it. These cameras are also able to see the legs, and a certain distance beyond them. Finally the toolcams are intended for use during more dexterous operations such as drilling or manipulation when the appropriate end-effectors are attached to the axle of the wheels. Figure 2.2 shows the combined field of view of the navcams and hazcams.
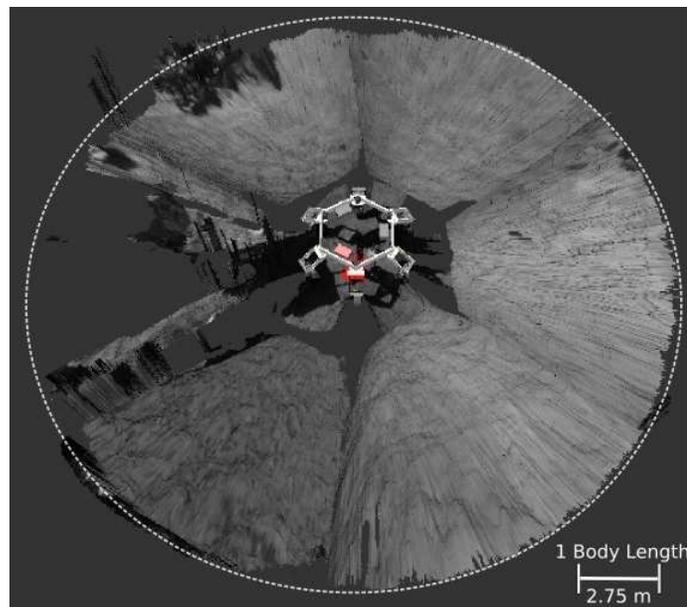
Figure 2.2: **The ATHLETE field of view provided by the cameras extends to a radius of approximately 3 body lengths. Blind spots are caused by occlusions and self-imaging.**

Torque Sensors

The ATHLETE robot is equipped with indirect torque sensing at each joint. These measurements are based on estimation of the torsional deformation of each joint by means of two encoders located at the input and output of the joint [Collins 07]. A schematic of the knee pitch joint is shown in Figure 2.3. This joint connects the thigh and shin of each leg, and is assembled in the following way:
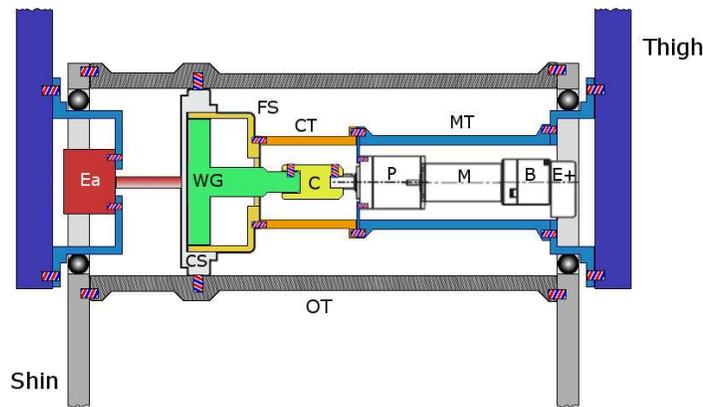
Figure 2.3: **Components of an ATHLETE joint.**

A motor tube (MT) is attached to the thigh, and contains the motor assembly which consists of the motor (M), planetary reduction stage (P), magnetic brake (B) and incremental encoder ($E+$). The planetary gear provides the first stage of reduction; the rest is introduced by a harmonic drive, which in turn consists of three parts: a flexspline (FS), a wave generator (WG) and a circular spline (CS). The flexspline is rigidly attached to the motor tube via a coupling tube (CT). This keeps the flexspline from rotating, and leaves the harmonic drive in a configuration with reduction ratio $R + 1$, where R is the reference ratio provided by the manufacturer [LLC 08]. Thus the input to the harmonic drive becomes the wave generator (connected to the motor via a coupling C), and the output is the circular spline. Therefore to transmit motion to the shin, the CS is connected to an output tube (OT) which is rigidly attached to

the shin. Finally, the output of the harmonic drive is also connected to an absolute encoder (Ea).

The difference between the angle indicated by the incremental and absolute encoders is a measure of the torsional deformation of the joint. In order to infer the torque, a calibration routine is followed to obtain stiffness curves for each of the 36 joints, by applying known torques to them. The torque measurement system is discussed in detail in [Collins 07].

Inertial Measurement Unit

In addition to the cameras and torque sensors, the robot is equipped with an Inertial Measurement Unit (IMU) manufactured by MicroStrain (Figure 2.4). The work presented in this thesis makes use of the IMU only to determine the spatial orientation of the body of the robot, via the attitude quaternion reading.

Figure 2.4: **The IMU on ATHLETE. Each side is 6cm long.**

2.1.2   Frames of Reference

The operation of legged robots requires the definition of a number of reference frames attached to the robot and the environment. Starting with the robot, one commonly selects a body or robot frame – {R} – which is usually attached to the centroid of the body or some other convenient part of it. Since each limb is itself a robotic manipulator, it is also convenient to define the base frame for each leg, referred to as the {L_i} frame, where i is the leg number. It is also necessary to define a frame

attached to the end-effector (in this case the foot) of each leg. This is referred to as a foot or tool frame, and represented as $\{T_i\}$ for each of the robot's feet. Finally, a fixed reference frame is attached to the ground at some convenient location (often the starting location of the robot). This inertial frame serves as a reference to define quantities such as distance covered and robot orientation, and is labeled the world frame $\{W\}$. Other reference frames can be defined as the application requires.

Figure 2.5 shows the frames selected the ATHLETE robot.
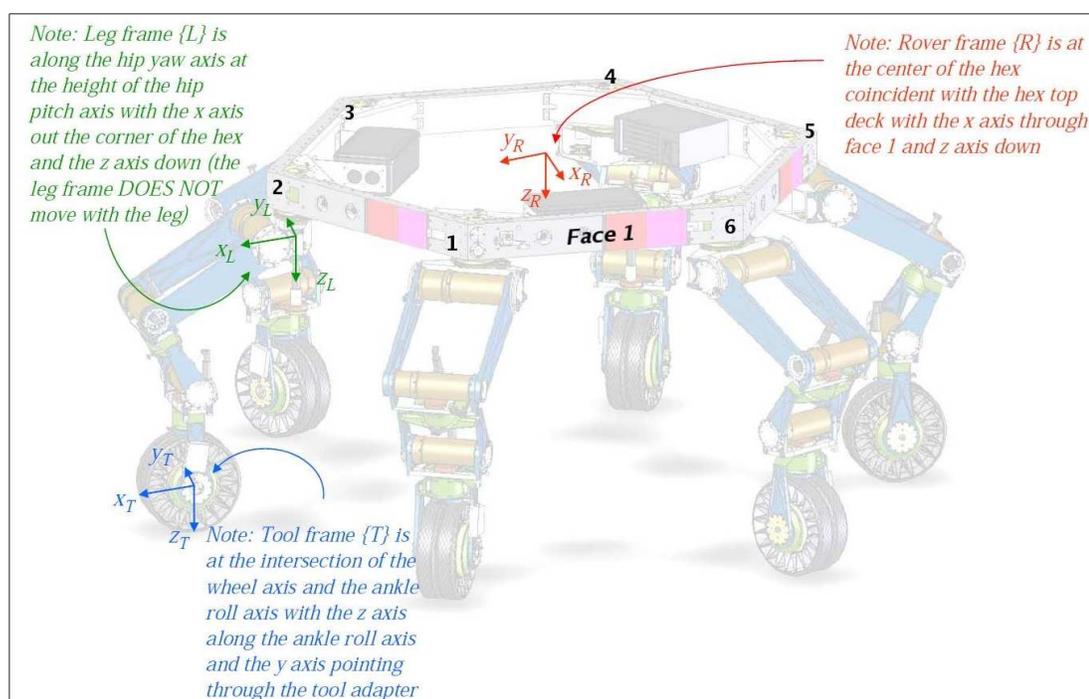
Figure 2.5: **Reference frames for the ATHLETE robot** (Image by Matthew Heverly, Courtesy NASA, Jet Propulsion Laboratory, California Institute of Technology)

2.2 Calculation of Contact Forces

When calculating the contact forces for a robot in static equilibrium with n_c feet on the ground there are $3n_c$ force components to solve for, but only 6 obvious equations to write: the sums of forces and moments on the robot. This means that the system of equations is under-specified, and it is not possible to solve for the reaction

forces without making special assumptions or adding constraints. The most common assumptions are that the robot and ground are rigid, and the tangential forces at the contact points are zero. As will be discussed below these are not always good assumptions, especially in robots with physical or contact compliance.

2.2.1   Pseudo-Inverse Approach

The calculation of contact forces is traditionally done by solving the system of 6 equations representing the balance of forces and moments on the robot. This system is underconstrained, since there are only 6 equations for $3n_c$ unknown force components, when n_c feet are in contact with the ground. Therefore, the standard procedure is to use the pseudoinverse solution, which has been proven to yield the *least-norm zero-interaction* case [Waldron 86a, Kumar 90]. This means that if a line is drawn connecting any two feet in contact, the difference of the projections of their reaction forces along that line will be zero; i.e., the legs are not squeezing.

Figure 2.6 shows the bottom view of a legged robot. In order to have zero inter-action, the difference of forces along any of the indicated dashed lines must be zero. This is not the case in the example shown because of the blue tangential forces. On **horizontal** ground, zero-interaction happens iff all tangential forces are exactly zero. On **slopes**, iff they are all parallel and have the same norm.
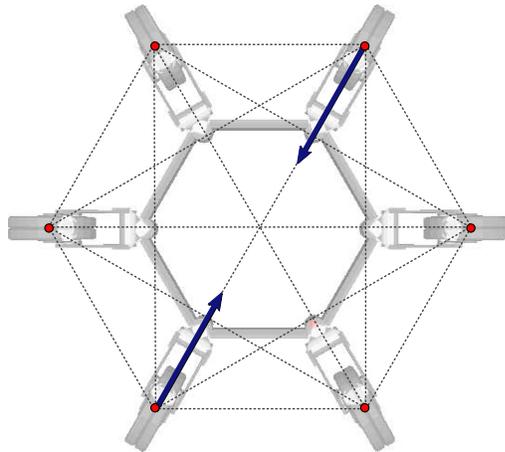
Figure 2.6: **A robot that is not in zero interaction**

When applied to robots with compliant contact points, some disadvantages exist with the pseudoinverse technique. First, the balance of forces and moments is done assuming perfectly rigid contacts, so the effect of compliance is not captured. In other words, the pseudo-inverse solution is an approximation that assumes zero sag.

Second, the technique is unable to capture the gradual redistribution of forces that occurs while lifting or placing a foot. It can be desirable to model this effect for pose optimization or sag mitigation.

Finally, the pseudoinverse becomes inaccurate if the stiffness of the contact points is different. In real life the load carried by each leg is proportional to its contact stiffness, an effect that is not accounted for in the traditional pseudoinverse solution.

Figure 2.7 illustrates this with a simple example of an "M"-shaped 3-legged robot. In the first case, all contact points have equal stiffness k_z and each leg carries $\frac{1}{3}$ of the weight. When the stiffness of the middle contact point is reduced by 50% the force carried by this leg decreases by the same amount relative to the other two, since the spring deformations are all the same. The correct solution is the one shown in Figure 2.7(b). However the pseudoinverse formulation would always return the distribution from Figure 2.7(a), because the spring constants are not used in the calculation of forces.

(a) Same spring constants   (b) Different spring constants
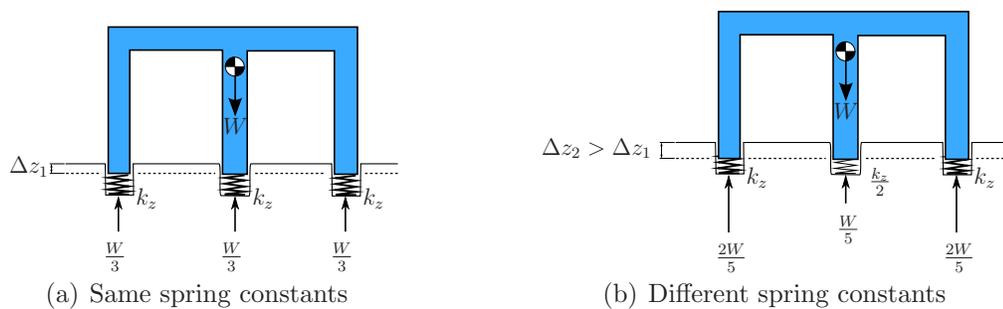
Figure 2.7: **The pseudo-inverse method always returns a force distribution that assumes the same stiffness at every contact point (left). The correct force distribution depends on the individual spring constants (right).**

2.2.2 Spring-Mass Force Model

In order to address these drawbacks, the contact points are modeled here as arrays of 3 springs oriented with the tangential-normal frame of reference as shown in Figure 2.8. A system of equations that are functions of the reaction forces can then be written. The resulting system is nonlinear and must be solved numerically.
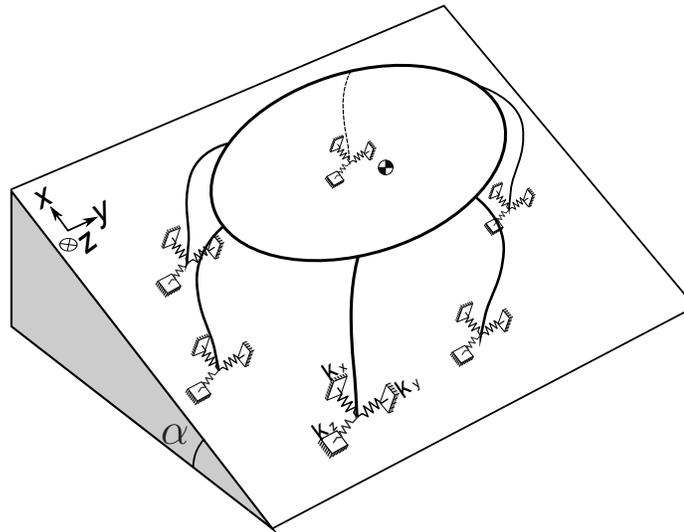
Figure 2.8: **Spring-mass model for reaction force and sag calculations.**

Similar models have been used in the past by a few authors (e.g. [Silva 05]). However there is a key difference in the way it has been used: authors that have modeled the contact points as springs usually calculate the reaction forces first using the pseudo-inverse formulation, and *then* use the spring equation to compute sag. In this dissertation the springs are included directly in the force calculations, with the advantages that have already been outlined.

Figure 2.9 shows the positions of the feet and CG before and after sag, expressed in a fixed reference frame (in this case {W}). These are given by Equations 2.1-2.2.

(a) Before sag (tires undeformed)   (b) After sag (tires deformed)
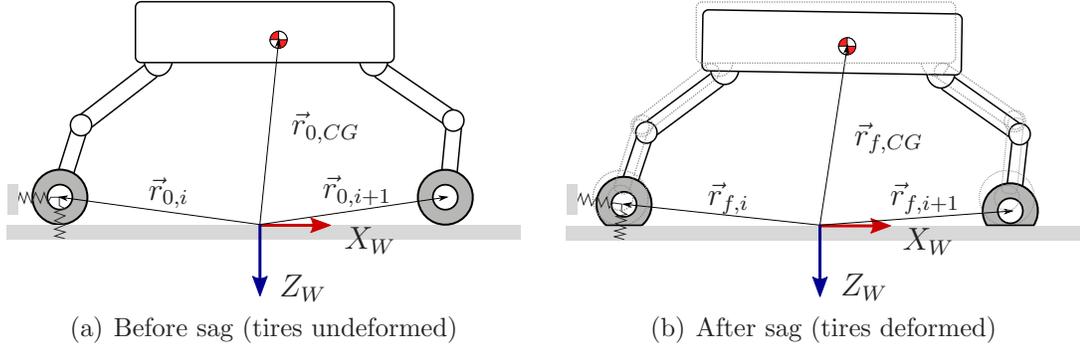
Figure 2.9: **Springs before and after sag.**

$$Before \quad : \quad \vec{r}_{0,i}; \tag{2.1}$$

$$: \quad \vec{r}_{0,CG}$$

$$After \quad : \quad \vec{r}_{f,i} = \vec{r}_{0,i} + \Delta\vec{r}_i; \tag{2.2}$$

$$: \quad \vec{r}_{f,CG} = \vec{r}_{0,CG} + \Delta\vec{r}_{CG}$$

Where for a linear spring the displacements in the (X, Y, Z) directions are given by:

$$\Delta\vec{r}_i = K_{inv} \cdot \vec{f}_i \tag{2.3}$$

Here K_{inv} is a diagonal stiffness matrix, defined in Equation 2.4. This matrix can be different for each foot if the spring constants are not all the same, as would be the case when different inflation pressures have been set at each foot. This also applies when a robot is transitioning from one kind of terrain to another, in which case some feet might be on stiffer ground than others.

$$K_{inv} = \begin{bmatrix} \frac{1}{k_{xx}} & 0 & 0 \\ 0 & \frac{1}{k_{yy}} & 0 \\ 0 & 0 & \frac{1}{k_{zz}} \end{bmatrix} \tag{2.4}$$

Now it is possible to write the sum of forces and moments about the fixed frame

of reference. This results in the first 6 balance equations:

$$\sum_{Contact} \left(\vec{f_i} \right) + m\vec{g} = \mathbf{0} \tag{2.5}$$

$$\sum_{Contact} \left(\vec{r}_{f,i} \times \vec{f_i} \right) + \vec{r}_{f,CG} \times m\vec{g} = \mathbf{0} \tag{2.6}$$

Assuming all the compliance is at the contact points and the robot is rigid otherwise, one can next write equations that constrain the geometry of the robot before and after spring deformation. With n_c feet in contact, the next n_c equations state that the distance between consecutive feet (i.e. between feet i and $i+1$) remains constant:

$$\|\vec{r}_{0,1} - \vec{r}_{0,2}\| - \|\vec{r}_{f,1} - \vec{r}_{f,2}\| = 0 \tag{2.7}$$

$$\|\vec{r}_{0,2} - \vec{r}_{0,3}\| - \|\vec{r}_{f,2} - \vec{r}_{f,3}\| = 0$$

$$\vdots$$

$$\|\vec{r}_{0,6} - \vec{r}_{0,1}\| - \|\vec{r}_{f,6} - \vec{r}_{f,1}\| = 0$$

That is, referring to Figure 2.9, the distance between the centers of wheels i and $i+1$ is the same in Figure 2.9(a) and Figure 2.9(b). This is actually true between *any* pair of feet on the robot, and can be repeated for non-consecutive feet until the robot's geometry has been fully constrained. Proceeding in this manner, the next block of equations comes from the constant distance skipping one foot (i.e. between feet i and $i+2$), for the load-bearing feet:

$$\|\vec{r}_{0,1} - \vec{r}_{0,3}\| - \|\vec{r}_{f,1} - \vec{r}_{f,3}\| = 0 \tag{2.8}$$

$$\|\vec{r}_{0,2} - \vec{r}_{0,4}\| - \|\vec{r}_{f,2} - \vec{r}_{f,4}\| = 0$$

$$\vdots$$

$$\|\vec{r}_{0,6} - \vec{r}_{0,2}\| - \|\vec{r}_{f,6} - \vec{r}_{f,2}\| = 0$$

At this point a total of $3n_c$ equations with $3n_c$ unknown force components for the feet in contact are available. However, closer inspection of Equation 2.6 reveals an additional dependency on the final position of the CG. This position needs to be calculated as well, and strictly speaking 3 more equations are needed which define the CG location before and after spring deformation. In practice, it was found that overconstraining the system by adding more CG equations results in better numerical convergence. For this reason n additional equations are used which indicate the spacing between the CG and each foot of the n-legged robot:

$$\|\vec{r}_{0,CG} - \vec{r}_{0,1}\| - \|\vec{r}_{f,CG} - \vec{r}_{f,1}\| = 0 \qquad (2.9)$$
$$\vdots$$
$$\|\vec{r}_{0,CG} - \vec{r}_{0,6}\| - \|\vec{r}_{f,CG} - \vec{r}_{f,6}\| = 0$$

Equations (2.5) through (2.9) are solved numerically using the Levenberg-Marquardt algorithm, with the optimization variables being the reaction force components and the final location of the CG. Note that the model outlined above can be used for any combination of feet in the air and on the ground. Some observations can be made:

1. In some cases the calculated reaction forces might require a foot to pull down. While physically impossible for ATHLETE, this is a correct calculation, and would not be out of the question for a robot with hooks or other grappling end-effectors (e.g. a climbing robot). If it is desired to eliminate solutions that pull, additional constraints can be added to enforce $f_{z,i} \geq 0$ or $f_{z,i} \leq 0$, depending on how the reference frames where chosen.

2. The problem becomes more difficult to solve as the spring constants get stiffer. Numerically, this is caused by the elements of K_{inv} approaching zero. Physically, this means that the robot approaches the unrealistic situation of perfectly rigid contact points. Note that as $K_{inv} \to 0$ Equations 2.7-2.9 effectively vanish and only the balance equations remain. If the robot under consideration adjusts to this model, the pseudoinverse solution is a better choice.

Incorporating Lift/Drop Transitions

Despite the generality of the above model, it still fails to capture the force redistribution that occurs when lifting or setting down a foot. In other words, it assumes that a foot is either fully loaded or bears no load. This is sufficient for many situations. However, if it is desired to explore the redistribution of loads to mitigate the effects of sag, an extension to account for lift/drop transitions is needed.

For this purpose, contact points for each foot are defined and denoted by $\vec{r}_{C,i}$. That is, $\vec{r}_{C,i}$ represents the location of *foot i*, expressed in the inertial reference frame, at which the bottom of tire i touches the ground and starts bearing load. On an arbitrary terrain, these contact points are $(x_i, y_i, z_{gnd@(x_i,y_i)} + R_{tire})$, and change for a given foot only when its (x, y) coordinates change. The contact points can be visualized as the fixed attachments of the springs to the ground in Figure 2.8

Now the force exerted by a given foot is redefined in terms of the contact points. Let the distance that foot i has been lifted off the ground (assuming no sag) be:

$$\Delta h_i = \vec{r}_{C,i}(z) - \vec{r}_{0,i}(z) \tag{2.10}$$

Note that $\Delta h_i > 0$ if the leg has been lifted ($+Z$ is down). Assuming a flat plane, the contact springs are affected differently – X and Y are able to apply their full forces as long as the tire is in contact and the foot does not slip. Z, however, has constantly diminishing action as the leg is lifted. This must be adequately portrayed in the corresponding equations. Thus for the linear spring model the forces will be given as follows:

$$f_i(x) = \begin{cases} -k_{xx} \cdot \Delta \vec{r}_i(x), & \text{if in contact} \\ 0, & \textit{otherwise} \end{cases} \tag{2.11}$$

$$f_i(y) = \begin{cases} -k_{yy} \cdot \Delta \vec{r}_i(y), & \text{if in contact} \\ 0, & \textit{otherwise} \end{cases} \tag{2.12}$$

$$f_i(z) = \begin{cases} -k_{zz} \cdot (\Delta \vec{r}_i(z) - \Delta h_i), & \text{if in contact} \\ 0, & \textit{otherwise} \end{cases} \tag{2.13}$$

Where the contact condition is provided by:

$$\text{In contact} = \begin{cases} \text{true,} & \text{if } \Delta\vec{r}_i\left(z\right) \geq \Delta h \\ \text{false,} & otherwise \end{cases} \tag{2.14}$$

Instead of solving for the reaction forces and final location of the CG, it is more convenient to choose the design variables of Levenberg-Marquardt to be the displacements of each foot and the CG. The force at each foot is computed internally using Equation(2.11). The geometry constraints guarantee that the foot displacements satisfy the rigidity assumption. With this method the number of equations remains constant because contact or lack thereof is now detected automatically.

2.2.3 Experimental Verification of Spring Constants for ATHLETE

In order to use the previously outlined force model on ATHLETE, it was necessary to determine the spring constants for the contact points. The robot is equipped with tires (either pneumatic or Michelin Tweels$^{©}$, Figure 2.10), so the spring constants are given by the stiffness of these tires when the robot is on hard ground like concrete, and by a combination of tire and soil stiffness when on compliant ground. Since all the experiments were conducted indoors or on the Marsyard at JPL which has fairly rigid soil, the spring constants were chosen to be the ones for the tires.

| (a) A Michelin Tweel$^{©}$ | (b) Maxxis pneumatic tires |

Figure 2.10: **Tweels$^{©}$ and tires on ATHLETE**

The manufacturer of the tires (Maxxis) provided force-deformation curves for different inflation pressures. The slope of these curves provides the stiffness constant for each spring. Tires were inflated to 8psi and the robot was moved through a series of poses in order to verify these constants, as well as the sag calculations. It was found that the tires were less stiff than the data sheets indicate. Most likely this is due to wear and tear, as well as physical variations in individual tires during manufacturing. The stiffness values are in the range of 3-5$\frac{kgf}{mm}$.

In the case of the Tweels, their approximate vertical stiffness was obtained from Michelin. The Tweels behave as two-stage springs, with higher rigidity above 500 kgf of load when the outer spokes are fully compressed and the inner hub begins to deform. The vertical stiffness is 7.5$\frac{kgf}{mm}$ from 0 to 500 kgf, and 40$\frac{kgf}{mm}$ from 500 kgf to 2500 kgf. The Tweels were not used for any of the experiments presented in this thesis.

2.3 Joint Torques

Given the forces at the feet, the joint torques that exactly balance them are obtained via the transpose of each leg's Jacobian matrix, as follows:

$$\vec{\tau}_{ext} = J^T \vec{F} \tag{2.15}$$

Where:

$\vec{\tau}_{ext}$ is the vector of joint torques that balance the external forces applied at the foot.

$\vec{F}$ is the vector of applied forces/moments at the foot, i.e. $\vec{F} = \{f_x, f_y, f_z, M_x, M_y, M_z\}^T$.

J^T is the transpose of the Jacobian matrix, expressed in the *leg* frame.

The Jacobian can be obtained by the cross-product method or screw theory as outlined in [Fu 87, Collins 07], as follows:

$$J = \left[\tilde{S}_1 \tilde{S}_2 \tilde{S}_3 \tilde{S}_4 \tilde{S}_5 \tilde{S}_6 \right] \tag{2.16}$$

Where $\tilde{S}_i$ are joint screws, defined as

$$\tilde{S}_i = \left\{ \begin{array}{c} \hat{z}_i \times \vec{\rho}_i \\ \hat{z}_i \end{array} \right\} \tag{2.17}$$

Here,

$$\vec{\rho}_i = \vec{r}_{foot} - \vec{r}_i \tag{2.18}$$

That is, $\vec{\rho}_i$ is the location of the *foot* with respect to *joint i*, expressed in the *leg frame*, and $\hat{z}_i$ is the rotation axis of revolute joint i, also expressed in the leg frame. [1]

For robots with massless legs, Equation 2.15 represents the total joint torques. If the mass of the legs is significant as with ATHLETE, the torques due to gravity must also be included, and the total torques become:

$$\vec{\tau}_{tot} = \vec{\tau}_{ext} + \vec{\tau}_{grav} \tag{2.19}$$

The calculation of gravity torques is outlined in [Collins 07] for the ATHLETE robot.

2.4 Multiplicity of Force/Torque Solutions — The Null Space

The objective of this section is to describe the relation between the null space of contact forces and the number of legs/DOF of the robot. The dimensions of the following two linear systems provide the necessary information:

1. The force-torque correspondence for an individual leg (Equation 2.15): $\vec{\tau} = J^T \vec{F}$

2. The force-moment balance for the whole robot (Equations 2.5 and 2.6):
   $\sum \vec{F} = \mathbf{0}, \sum \vec{M} = \mathbf{0}$

---

[1]Actually the equations can be expressed in any reference frame, as long as consistency is maintained throughout. For example, if the Jacobian is expressed in the *tool* frame, the external forces must also be expressed in that frame.

2.4.1   Solutions for Individual Legs

Referring to Equation 2.15 the dimensions of each component are as follows:

- $\vec{\tau}$: $m \times 1$, where m is the number of joints in the leg.

- J^T: $m \times 6$

- $\vec{F}$: 6×1

In these equations the applied wrench $\vec{F}$ is *always* a vector with 6 components. These include the 3 cartesian components of the net applied external force, and the 3 components of the net external moment. Some of these elements are sometimes known to be zero, for example in the case of a robot whose contact points are unable to transmit moments.

Number of solutions

The linear system $J^T \vec{F} = \vec{\tau}$ relates to the number of force and torque solutions as follows:

- The dimensions of J^T indicate how many combinations of external forces and moments produce the same set of joint torques.

- Conversely, the dimensions of $(J^T)^{-1}$ indicate how many possible combinations of joint torques would result in a desired force/moment at the end effector.

The solution of the system in either direction is of interest in walking robots: output forces from applied joint torques relate to control (e.g. force control), while torques from forces relate to sensing (e.g. estimated set of joint torques that a given load will produce).

From the above discussion, the following can be concluded about the number of possible solutions:

- If $m < 6$, then J^T is fat and the system has fewer DOF than variables to control. This means that: *(a)* there is an infinite number of external force/moment

combinations that yield the same joint torques, and conversely *(b)* it might not be possible to find a set of joint torques to achieve a desired force/moment. In other words, the system is underactuated.

- If $m = 6$, then J^T is square and a unique solution exists in either direction, assuming no singularities are encountered.

- If $m > 6$, then J^T is skinny and redundancy exists: more than one combination of joint torques can be found to achieve a desired force/moment output. However there might not be any force/moment combination that results in a given set of torques.

The above holds under the assumption that J^T is full-rank. If that is not the case it means that one or more of the components of $\vec{F}$ have no effect on the joint torques. Conversely, if $(J^T)^{-1}$ is not full rank, there will be one or more joints that have no effect on the output force/moment.

The ATHLETE robot is equipped with 6 joints per leg, and thus falls into the case of 1:1 correspondence between forces and torques. The majority of walking robots in existence today fall into the $m \le 6$ category. Smaller robots tend to use 3 joints per leg (hip yaw, hip pitch and knee pitch). This is the minimum number of joints that allows simultaneous control of all 3 cartesian coordinates of the foot. Walking robots with only one DOF per leg exist (e.g. RHex), but this constrains their locomotion capabilities to the use of less traditional wheel-legs and the corresponding regular gaits that are possible with these. An example in the $m > 6$ category is the TriATHLETE robot currently under development at NASA's Jet Propulsion Laboratory, which is equipped with 7 joints per leg.

2.4.2 Solutions for the Complete Robot

To examine the nullspace for the entire robot it is necessary to rewrite Equations 2.5 and 2.6 in matrix form.

Balance Equations

Let $\vec{f}$ be a vector of reaction forces at the feet in contact expressed in the robot frame {R}, and $\vec{f_g}$ be the weight vector, also in the {R} frame. Let n_c be the number of feet in contact, then:

$$\vec{f} \quad = \quad [f_{x1}, f_{y1}, f_{z1}, \ldots, f_{xn_c}, f_{yn_c}, f_{zn_c}]^T \tag{2.20}$$

$$\vec{f_g} \quad = \quad m\vec{g} \tag{2.21}$$

Equation 2.5 can be rewritten as follows:

$$\Phi\vec{f} = -\vec{f_g} \tag{2.22}$$

Where the matrix Φ is composed of as many 3×3 identity matrices as feet are in contact with the ground:

$$\Phi = [I| \ldots |I]_{3 \times 3n_c} \tag{2.23}$$

In order to write the net moment about the CG of the robot, the matrix form of the cross product of two vectors is useful:

$$\vec{r} \times \vec{f} = C_i\vec{f} \tag{2.24}$$

Where C_i is the cross-product matrix:

$$C_i = \begin{bmatrix} 0 & -r_z & r_y \\ r_z & 0 & -r_x \\ -r_y & r_x & 0 \end{bmatrix} \tag{2.25}$$

Equation 2.6 can now be rewritten in matrix form as follows, assuming the moments are taken about the CG and the reaction forces are given in the {R} frame:

$$C\vec{f} = \mathbf{0} \tag{2.26}$$

Where the matrix C is the collection of the cross-product matrices for the feet in contact:

$$C = [C_1| \ldots |C_{n_c}]_{3 \times 3n_c} \tag{2.27}$$

Combining Equations 2.22 and 2.26 produces the system of static equilibrium equations: [2]

$$\Gamma \vec{f} = \begin{bmatrix} -\vec{f_g} \\ \mathbf{0} \end{bmatrix} \tag{2.28}$$

Where Γ results from stacking the Φ and C matrices:

$$\Gamma = \left[\begin{array}{c|c|c} I & \cdots & I \\ \hline C_1 & \cdots & C_{n_c} \end{array} \right]_{6 \times 3n_c} \tag{2.29}$$

Number of Solutions

The matrix Γ in Equation 2.28. is of dimension $6 \times 3n_c$. Thus for any robot with more than *two* legs on the ground, Γ is fat and a nullspace of contact forces exists.

In the tangential (X, Y) direction this says that the robot can hold up its weight while squeezing the ground with arbitrary force, as long as these squeezing forces cancel each other out (Figure 2.6).

A nullspace of forces can also exist in the vertical direction. To analyze this, the tangential forces in Equation 2.28 are assumed to have known, fixed values. Since f_x and f_y are no longer unknowns, Equation 2.20 reduces to the following:

$$\vec{f} = [f_{z1}, \ldots, f_{zn_c}]^T \equiv \vec{f_z} \tag{2.30}$$

At the same time, the matrix Γ is affected as follows:

- Each submatrix I loses the first two rows and columns. In other words, the only force balance that remains is the balance in the z direction, which makes

---

[2]Note that Equation 2.28 is a fat linear system, whose Moore-Penrose pseudoinverse is the traditionally used *zero-interaction solution* mentioned at the beginning of this chapter.

sense.

- Each submatrix C_i loses the first two columns because the moments due to f_x and f_y have already been accounted for. It also loses the last row, since the remaining force component f_z is unable to apply any moments about the z axis.

After discarding all these rows and columns, the force and moment balance for the robot reduces to the following:

$$\Gamma_z \vec{f_z} = \begin{bmatrix} -f_{gz} \\ 0 \\ 0 \end{bmatrix} \tag{2.31}$$

Where the reduced matrix Γ_z is now:

$$\Gamma_z = \begin{bmatrix} 1 & \vdots \cdots \vdots & 1 \\ r_{y1} & \vdots \cdots \vdots & r_{yn_c} \\ -r_{x1} & \vdots \cdots \vdots & -r_{xn_c} \end{bmatrix}_{3 \times n_c} \tag{2.32}$$

The conclusion is that if $n_c = 3$, a nullspace does not exist in the vertical direction (i.e. a tripod has no vertical nullspace). However if $n_c > 3$, then Γ_z is fat and a nullspace exists.

The implications of these nullspaces will be discussed in the following section.

2.4.3 Load Redistribution in Walking Robots

It is now possible to discuss what options exist to redistribute loads between the joints of a walking robot. As implied in §2.4.1, the **first** possibility is to transfer torques from one joint to another *within the same leg* without modifying the applied load. This is only possible if $m > 6$.

The **second** possibility is to change the load distribution among the legs of the robot without changing the joint angles or the equilibrium conditions. This is made possible by the existence of the tangential and normal nullspaces, and can be accomplished through the commanded torques. In reality flexible contact points will deform

as the load changes, causing some changes in geometry. The more rigid the contacts, the smaller these changes will be.

The **third** possibility is to change the force distributions by applying small changes to the joint angles, for example moving one foot up or down so that it pushes more or less on the ground. This is a more viable way of carrying out force control, and is usually possible for most walking robots because it relies on cartesian motion of the foot rather than on direct torque control. The changes in the configuration of the robot are usually also small in this case.

Because little or no change is made to the configuration of the robot, the previous three cases are referred to as *internal* load redistribution. The **fourth** and final possibility is to modify the load distribution by displacing the robot's CG. This can be accomplished by moving or rotating the body without changing the contact points of the feet, resulting in simultaneous changes of the loads and the joint angles. This approach has a bigger impact on the leg Jacobians than internal redistribution techniques.

Chapter 4 will make use of the 4th approach, while the optimization setup in Chapter 6 will assume rigid contact points as in the 2nd approach.

2.5   Future Model Improvements

While the spring-mass model presented in this chapter has proven sufficient for this research, a number of improvements can be made in the future. Some of these are summarized below.

1. Relaxation of the assumption that all outward normals at the feet are the same. This would allow more realistic analysis on terrains with bumps. This is a minor extension which involves additional transformation matrices applied to the reaction forces when expressing them in the robot frame.

2. A closed-form linear approximation that incorporates spring constants. One possibility is to write linear approximations to Equations 2.7–2.9. Some thought has been given to using linear combinations of the 1-norm and the ∞-norm, but

this has not yet incorporated into the model. Another possibility is to use a Weighted Least Norm (WLN) solution instead of the standard least norm.

3. A more detailed compliance model of the robot. Although the assumption of concentrated compliance at the feet has provided enough accuracy for this work, this might not be true of robots with more flexible limbs or body. The improved model would incorporate the load-displacement behavior of the different parts of the robot, which can be obtained by manual calculation in some cases, or FEM analysis for complex geometries. Zoppi and Molfino [Zoppi 06] have taken some steps in this direction, but plenty of work remains.

4. Currently the calibration of spring constants is done manually: the robot is moved through a series of symmetric and asymmetric configurations, and laser measurements are taken of the tire compressions and height above the ground of the corners of the chassis. It would be desirable to be able to do this calibration automatically. For this, the height of the corners can be approximately calculated from knowledge of the body geometry and measurements of height and tilt obtained with the IMU. Determining the compression of the tires automatically is a more difficult problem. With the sensors currently on the robot, the only way to estimate this seems to be through computer vision techniques. This is expected to be reasonably accurate on solid ground like concrete, but if the ground is deformable a problem arises in differentiating between wheel sinkage and tire compression, and important distinction particularly on highly compliant ground with nonlinear force-sinkage behavior. A rough estimate of spring constants could be made using only the sag of the body. However additional sensing to measure tire compression directly would probably be needed for better accuracy.

Chapter 3

Background on Gaits

This chapter describes the related work and other necessary background information.

§**3.1** defines the terminology used in the context of gait research.

§**3.2** presents the leg numbering conventions.

§**3.3** describes the stability metrics applicable to this work.

§**3.4** outlines the procedure used to plan and execute individual steps.

§**3.5** describes the complete process of gait generation for walking robots.

§**3.6** summarizes the most relevant related work.

3.1 Definitions

This section provides some basic definitions related to gait generation that will be helpful in future discussions.

Gait: A sequence of steps and body shifts that a legged robot executes to achieve motion. A gait might consist of a repeating pattern, in which case it is known as a *regular* or *periodic* gait. However, non-repeating patterns may be preferable in some cases, and these are known as *free* gaits. Finally, it is also possible to follow a regular gait most of the time and apply changes to it only when necessary, for example to avoid stepping on a forbidden area. In this case, the robot is said to be executing an *adaptive* gait.

Continuous gait: A gait in which body shifts and steps are allowed to take place simultaneously. As a result the body of the robot is constantly in motion, often at a constant speed.

Discontinuous gait: In this gait the steps happen when the body is stationary, and similarly the body is shifted only when all feet are in contact with the ground. That is, steps and body shifts are not allowed to happen simultaneously, resulting in a speed that oscillates between zero and some maximum value.

Crawl gait: A discontinuous gait in which only one foot is moved at a time. The name points at the fact that this gait is very slow and deliberate. Its main advantage is that it is very safe.

Crab gait: A gait where the body of the robot remains pointed in the same direction regardless of the actual direction of motion.

Turning gait: In contrast to the crab gait, this gait maintains the body aligned with the direction of motion. If a curved path is being followed, then the body will be oriented tangentially to that path at all times. Turning gaits are more difficult to plan because the legs must be coordinated to provide forward progress as well as body rotation. It is a better gait if the robot's sensing is limited to the forward direction.

Support phase: Period of time during the motion in which a given foot is on the ground.

Transfer phase: Time period when a given leg is executing a step, and is thus not in contact with the ground.

Transfer time: Amount of time required to complete the transfer phase of a given leg.

Leg stroke (R): Distance through which the foot is translated relative to the body during the support phase (see Figure 3.1).

Kinematic margin (K_m): Distance from the current foot location to the rear of its reachable space, along the desired direction of motion (See Figure 3.1).

Static stability margin (SSM): Shortest distance of the vertical projection of CG to the boundaries of support pattern. This and other stability metrics will be covered in §3.3.

Step: Motion of a leg to place the foot at a new location.

Timestep: Each of the moves that constitute a gait (steps, body shifts, or discrete waypoints in the execution of these).

Pose: A full robot configuration – $x_b, y_b, z_b, \phi_b, \theta_b, \psi_b$ plus 36 joint angles.

Body pose: The position and orientation of the body – $x_b, y_b, z_b, \phi_b, \theta_b, \psi_b$.
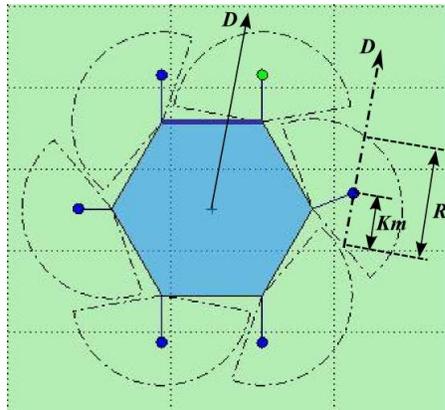
Figure 3.1: **Leg stroke and kinematic margin for a legged robot. D is the direction of motion.**

3.2   Leg Numbering Conventions

Traditionally, the numbering of the legs of a walking robot follows the convention shown in Figure 3.2(a). This convention originated in research that used robots with elongated bodies and a clearly preferred direction of motion. The odd-numbered

(a) Even-odd   (b) Circular
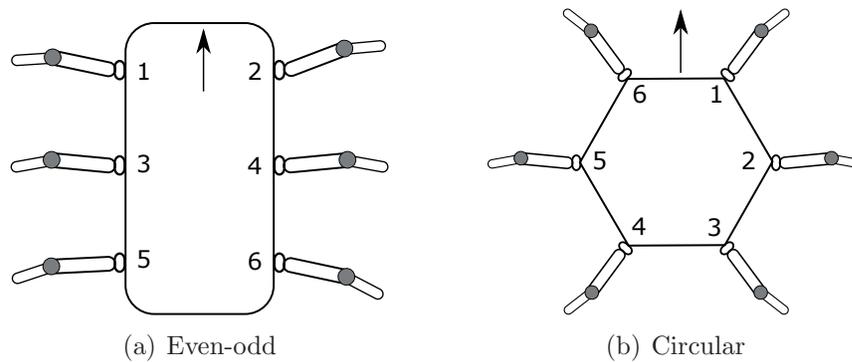
Figure 3.2: **Leg numbering conventions for walking robots, with direction of motion indicated by the arrows.**

legs are on the left side of the body, and the even-numbered ones on the right side, assuming motion in the preferred direction.

For robots that don't have a preferred direction of motion, the above convention has also been used, but its significance is lost as soon as the robot walks in a direction other than the one used for numbering. An alternative convention is to number the legs in a clockwise or counter-clockwise sequence around the body, as shown in Figure 3.2(b). The actual direction is selected to follow the right-hand rule about the vertical $(\hat{Z})$ body axis.

In both cases, the numbering of legs can either start at 0 or 1, more commonly the latter. Ultimately the selection of a numbering sequence is a matter of choice, but adjusting to one of these two conventions can be advantageous when relating to other work in the field, particularly in the context of gait generation.

3.3   Stability Metrics

3.3.1   Static Stability Margin

The Static Stability Margin *(SSM)* is illustrated in Figure 3.3. The SSM is found by first constructing the polygon of support *(POS)*, which is the convex hull of the ground contact points, assuming all the contact points lie on a plane. The SSM is then the minimum distance of the projection of the CG onto this plane to any of

(a) Full Polygon (b) Conservative Polygon
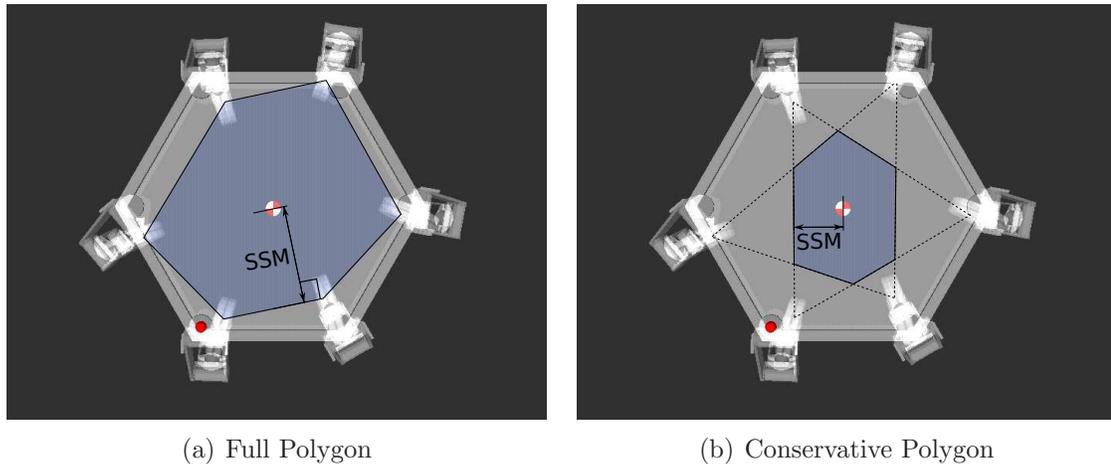
Figure 3.3: **Polygons of support and the SSM, with 6 feet in ground contact.**

the edges of the POS (Figure 3.3(a)). To obtain gaits which are more conservative in terms of stability it is also possible to use a reduced or conservative polygon of support. This polygon is the intersection of all support polygons drawn with the feet in contact *minus one*, to simulate the failure of one of the supporting legs (Figure 3.3(b)). [1]

The SSM is a common stability metric which is easy to compute, and provides a realistic assessment of stability if dynamic effects do not play a role and the ground is flat and horizontal.

A variation of this metric, the Longitudinal Stability Margin *(LSM)* is sometimes used for faster calculation. The LSM is the distance from the projected CG to the support polygon along the direction of motion. This simplified metric must be used with care to ensure that stability is not accidentally violated in the lateral direction. The study of wave gaits has made extensive use of the LSM, and the work of McGhee and Frank [McGhee 68b], Bessonov and Umnov [Bessonov 73], Sun [Sun 74], and Song and Waldron [Song 89] demonstrated that the LSM is in fact maximized by this type of gait for 2n-legged robots $(n > 1)$.

---

[1] In these figures, all feet are assumed to be on the ground, with contact points at the bottom of the tires.

3.3.2   Energy Stability Margin

As mentioned above, the SSM is appropriate when walking on horizontal ground but not when the robot is negotiating a slope. This can be understood by mechanical energy considerations. In order for the robot to topple over, it must rotate about one of the edges of the POS. The maximum potential energy is observed when the CG is directly above the axis of rotation. Therefore a tipping event requires an increase in potential energy to achieve this maximum value.

If a robot is on a slope with its CG at the center of the support polygon, it can roll over more easily in the downhill direction because the required change in potential energy is smaller than in the uphill direction. Thus, a more stable configuration can be achieved by shifting the CG uphill, away from the "bottom" of the POS. Humans seem to have an intuitive understanding of this, since it is what we tend to do to become more stable when walking uphill.

The Energy Stability Margin *(ESM)*, proposed by Messuri and Klein [Messuri 85], is calculated by the same energy considerations — it is the *minimum* increase in potential energy to rotate the robot about any of the edges of the POS is computed. In order to make the metric independent of robot mass the ESM is usually scaled by the robot weight as proposed by Hirose et al. [Hirose 01], leading to the Normalized ESM *(NESM)*. The calculation of the NESM is described in [Hirose 01, Garcia 02], and is summarized below. The NESM is defined as follows:

$$NESM = min(\Delta h_i) \tag{3.1}$$

Here, each Δh_i is the necessary height change of the robot's CG to tumble about rotation axis i, and is defined as:

$$
\begin{aligned}
\Delta h_i &= h_{max,i} - h_0 & (3.2)\\
&= \|\vec{R_i}\|(1 - \cos\theta)\cos\gamma & (3.3)
\end{aligned}
$$

Where

$h_{max,i}$ is the maximum height reached by the CG when the robot rotates about edge i of the POS.

h_0 is the initial height of the CG.

$\vec{R}_i$ is the shortest vector from the CG to the rotation axis.

θ is the angle between $\vec{R}_i$ and the vertical plane.

γ is the inclination of the rotation axis relative to the horizontal plane.

Let $\hat{L}_i$ be the unit vector representing edge i of the POS, defined by the difference of the locations in $\{W\}$ of two consecutive feet $(i, i+1)$:

$$\vec{L}_i = \vec{r}_{i+1} - \vec{r}_i \tag{3.4}$$

$$\hat{L}_i = \frac{\vec{L}_i}{\|\vec{L}_i\|} \tag{3.5}$$

The angle θ between $\vec{R}_i$ and the vertical plane that contains $\hat{L}_i$ can be calculated as follows: we first find the unit normal to the vertical plane of interest with Equation 3.6.

$$\hat{n}_i = \hat{L}_i \times -\hat{Z} \tag{3.6}$$

And then the angle θ with Equation 3.7

$$\theta = \frac{\pi}{2} - \arccos\left(\frac{\vec{R}_i \cdot \hat{n}_i}{R_i}\right) \tag{3.7}$$

The angle γ between the rotation axis and the horizontal plane is itself determined by means of Equation 3.8.

$$\gamma = \frac{\pi}{2} - \arccos\left(-\hat{L}_{i,Z}\right) \tag{3.8}$$

A contour of NESM for the ATHLETE robot on a $10°$ slope is shown in Figure 3.4. The contour represents the value of NESM as a function of body position. Uphill

is in the $+X$ direction, toward the right of this image, and the maximum stability value is achieved by shifting the body uphill.

(a) Side View

(b) Contour Plot (top view)
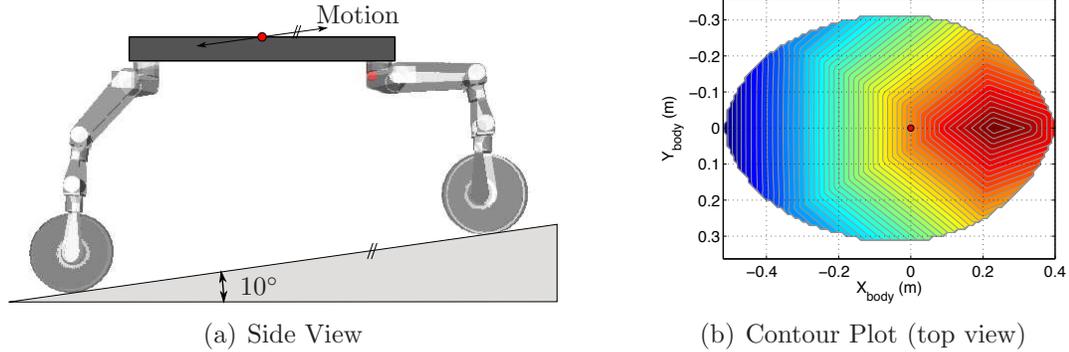
Figure 3.4: **NESM variation for ATHLETE on a 10° slope as a function of body position. (a)The body can be moved parallel to the ground without moving the feet, (b)The contour of NESM indicates that stability is maximized by shifting the body uphill 0.22m (initial position is shown by the red dot, and uphill is to the right).**

3.4 Motion Planning of Individual Steps

The sequence of configurations that an individual leg must follow to get the foot from one point to another during a step is called a *motion plan* [2]. Depending on the complexity of the leg and the surrounding environment, this can be done following different approaches.

One approach is to pre-define the trajectory in 3D space that the foot must follow. Parabolic paths are popular because they are easy to calculate and can be executed with smooth variations in motor speeds. If the robot is expected to move only in certain directions, the sequence of configurations for these discrete sets of directions can be pre-computed and saved as a library that is referenced at run time. This con-siderably speeds up the process because repeated inverse kinematics (IK) calculations are only done when building the library.

The above technique is only applicable on planar, unobstructed terrain. If there exist bumps on the ground or footfall locations to be avoided, steps must be adapted

---

[2]More precisely, it is the sequence of intermediate configurations to get the leg from an initial to a final configuration, or set of joint angles.

accordingly. Stretching of the original paths in configuration space has been explored by Hauser [Hauser 08a] and others. An alternative is to plan the motion using a grid-based or randomized technique that incorporates joint angle limitations, a terrain model and a robot model to find a feasible plan that prevents collisions with the environments and other parts of the robot.

For the simulations and experiments presented in this dissertation three approaches were implemented and compared: a grid-based planner in cartesian space, another grid-based planner in joint space, and a randomized planner. For both grid-based cases the well-known A^* algorithm was used. In the randomized case, the SBL planner developed by Sánchez and Latombe [Sanchez 01] was used. In all cases, smoothing was applied to the motion plan via iterative bisection and Dijkstra simplification.

The comparison of motion planning approaches is explained in detail in Appendix A. As a result of this comparison the SBL technique with smoothing was selected for use on the ATHLETE robot. A^* in cartesian space was found to be a suitable alternative with approximately equal performance.

3.5 General Procedure for Statically-Stable Gait Design

Walking gaits are in essence sequences of steps and body shifts to be executed by the robot. This section discusses two cases: first the case of gaits with constantly repeating motion patterns known as periodic gaits. Second, gaits where the motion parameters change from cycle to cycle.

3.5.1 Periodic Gaits

On flat, unobstructed terrain no obstacles are encountered and a periodic gait can be executed. The advantage of regular gaits is that they require limited computation due to their repeating nature. A structured framework for regular gait specification and analysis was initially devised by McGhee et al. [McGhee 85a, McGhee 85b]. They introduced the concept of a *gait formula*, which consists of a collection of parameters

that uniquely define a periodic gait. The use of the gait formula is explained in the books by Song and Waldron [Song 89] and Gonzalez de Santos et al. [de Santos 06].

At a high level, it is necessary to define the sequence and timing of moves to be executed by the robot for walking. The process begins by deciding between a *continuous* or *discontinuous* gait, as defined in §3.1.

In the **continuous** case, the body is constantly in motion (usually at a constant speed). Body shifts need not be specified because of the continuous motion of the body, but the sequence and timing of steps is necessary. For example, in the simplest case a possible choice is to step with only one leg at a time, requiring specification of the step sequence. A popular sequence is the *wave*, which moves the legs on one side from back to front, followed by the other side from back to front.

The sequence, however, does not uniquely define a gait – timing information is also required. Take for example the first two steps of a wave gait: after completing the first step, one possibility is to initiate the second step immediately. Another possibility is to continue shifting the body for some time with all feet on the ground before initiating the second step.

In the context of McGhee's framework, the sequence and timing are encoded by two parameters:

Duty factor (β_i): The fraction of a gait cycle that leg i is in contact with the ground (i.e. in the support phase).

Leg phase (ϕ_i): The fraction of a gait cycle by which the *placement* of leg i lags behind the placement of leg 1. Here leg 1 is the actual physical number of the leg on the robot, and not the first leg that takes a step. This means that a leg's phase may be negative if its placement occurs before that of leg 1, or positive if it happens after leg 1.

With this in mind, the simplest specification of a gait for a robot or animal with n legs is given by the *gait formula* in Equation 3.9. It is possible for all the legs to have the same duty factor, in which case only one value of β is specified.

$$g = \{\beta_1, \ldots, \beta_n, \phi_1, \ldots, \phi_n\} \tag{3.9}$$

For example, if a walking robot like the one in Figure 3.2(b) executes the sequence of steps {6-5-4-1-2-3} (a reverse wave sequence), with one step at a time, and each step starting immediately after the previous one ends, the gait is defined by Equation 3.10. Note that all feet spend the same amount of time in the support phase.

$$g_{RW} = \{\beta = \tfrac{5}{6}, \phi_{1...6} = 0, \tfrac{1}{6}, \tfrac{1}{3}, -\tfrac{1}{6}, -\tfrac{1}{3}, -\tfrac{1}{2}\} \tag{3.10}$$

Because β_i and ϕ_i are dimensionless fractions of the time it takes to execute a full gait cycle, the speed at which the robot moves can be specified independently, without any change to the gait formula.

Note that Equation 3.9 specifies only the "big picture" of a gait. It says nothing about the length of the individual steps, the selection of footfall locations, or the path followed by the foot when executing a step. A more detailed gait specification was created by McGhee et al. to include the initial and final position of each foot *relative to the body*, in addition to the values of β_i and ϕ_i. This is known as the *kinematic gait formula*, and is also explained in [Song 89].

For ATHLETE a **discontinuous** gait has been selected, due to its ease of implementation that requires less sophisticated coordination during stepping. This is a common choice for walking robots. In the discontinuous gait, the steps are executed with the body stationary, and conversely the body is shifted with all feet on the ground. A reverse wave sequence has been chosen, in which the placement of the feet runs from front to rear, with the left side being 180° out of phase with respect to the right side. The reverse wave sequence was selected because it maximizes the distance between consecutive feet, preventing situations like the one shown in Figure 3.5.

Discontinuous gaits can also be specified via the gait formula, but now the length and direction of body shifts must be specified too. It is possible to make certain assumptions, such as equal-length body shifts in the direction of motion, in which case the length σ of each body shift for a legged robot with n legs is specified by Equation 3.11 once the robot has settled into a regular gait.

$$\sigma = \frac{\lambda}{n} \tag{3.11}$$
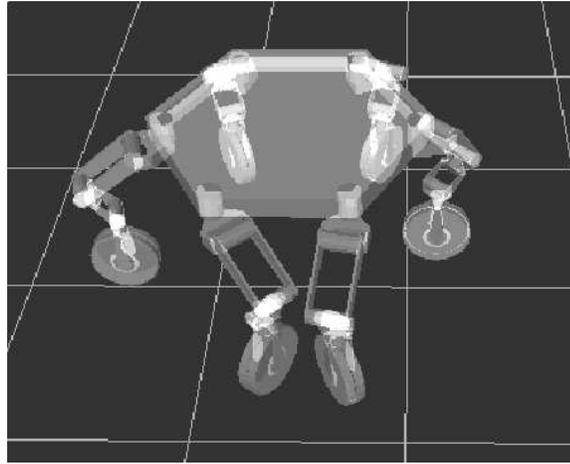
Figure 3.5: **Risky positions prevented by the reverse wave gait.**

Where λ is the robot's *stride*, i.e. the distance that the body advances after a complete gait cycle.

3.5.2 Non-periodic Gaits

In the previous section a general procedure for periodic gait design was provided. In many situations these repeating motion patterns are not appropriate primarily because of forbidden areas in the environment where the robot may not step (e.g. rocks, crevices).

In this case it is not possible to provide a general procedure for gait design, because the best approach depends on the specific conditions that the robot will face. The extensive body of literature on *adaptive* and *free* gaits covers many techniques for cases where periodic gaits are inadequate, for example when crossing a boulder field. Figure 3.6 shows a simulation of a hexapod crossing a field with fairly dense boulder distribution. A periodic gait was found to result in collisions between the feet and a number of obstacles. A simple adaptation consisting of shortening the steps when a collision is foreseen resulted in successful traversal of the boulder field. This means that non-periodic gaits need not be too complex – they can be constructed by following a periodic gait most of the time, with local adaptations only when necessary.
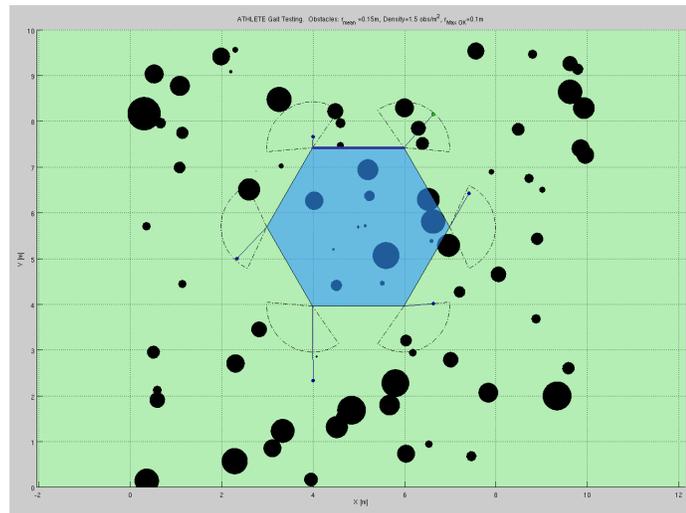
Figure 3.6:   **Traversal of a boulder field usually requires an adaptive or free gait.**

As the terrain becomes more complex, so does the gait design process. For very unstructured terrain, the challenge often becomes one of feasibility because valid motions are difficult to find. General motion planning approaches for this kind of situation have been developed for walking and climbing robots by Bretl [Bretl 05, Bretl 06] and Hauser et. al. [Hauser 08a, Hauser 08b], and have been validated experimentally on the Lemur and Capuchin robots, and in simulation for the ATHLETE robot. These planners search for feasible motions directly in the 42-dimensional configuration space of the robot, and as a result carry a high computational cost. However, their ability to find viable motion plans in highly constrained situations makes them suitable for extreme terrains.

3.5.3   The Skeleton Gait

Whether a periodic or non-periodic gait is selected, it is convenient to decompose the process in two parts:

Skeleton Gait: This consists of the sequence of robot configurations without the details on how each individual step is executed.

Step Planning: From the skeleton gait the information on the initial and final configuration of the leg during a step can be obtained. A motion planner is then applied to determine the sequence of waypoints that individual legs must follow to complete a step, as previously described in §3.4.

The above breakdown is advantageous because the optimization can be applied to the skeleton gait directly. Note that, since the robot poses may be modified by the gait optimizer, existing step plans would need to be discarded to take into account the new start and end leg configurations.

3.6   Gait Optimization and Related Work

The focus of this dissertation is on optimal gaits for slowly-moving, statically-stable walking robots. The main thrust of research on legged robots has shifted in recent years to dynamically-stable walking or running. In that context new control techniques have been developed that are capable of dealing with very challenging terrains (e.g. BigDog [Playter 06] and SandBot [Li 09]), take advantage of the dynamics introduced by robot compliance [Silva 03], and propel the robot at higher speeds.

However, this body of work relies on actuation capabilities with high mechanical power (e.g. hydraulics, artificial muscles) to accomplish locomotion. While impressive, the inherent assumptions of these approaches make them unsuited for robots with weak actuators, which are the ones most prone to saturation. Using powerful actuators is not always possible due to various limitations like mass, electrical power and even cost. The remaining exploration of related work focuses on gait generation under quasi-static assumptions with weak actuators.

3.6.1   Actuator Limitations in Walking Robots

The focus of gait optimization involving joint torques has been on energy efficiency, without emphasis on distance to saturation. The motivation is clear and reasonable: legged robots require electrical power to move, and this power must be carried

aboard in the form of batteries or obtained from alternative sources such as solar pan-els. Because the system must be ideally self-contained (i.e. no long extension cords required), a reduction in power consumption will increase the range or autonomy of the robot. Therefore, the majority of papers describing torque-related optimization focus on minimization of power.

The motivation for improving actuation margin instead is one of feasibility and robustness. Legged robots intended for cargo or scientific applications can, by design, be required to operate close to saturation. Therefore adequate gaits are needed to maximize the useful payload and guarantee continuous motion. The reader is asked to keep this distinction in mind through the remainder of this dissertation.

Having said this, energy minimization approaches deal with functions of the joint torques, and contain lessons that can be incorporated when dealing with gaits for preventing saturation.

The cost metrics commonly used are functions of the joint torques and angular velocities – $J_1(\tau\dot\theta)$ (for minimization of mechanical power), or of the square of the torques – $J_2(\tau^2)$ (for minimization of electrical power).[3] These are referred to as *type J_1* and *type J_2* functions in the discussion that follows.

OPTIMIZATION WITH ACTUATION MARGINS

The idea of achieving a comfortable margin away from saturation has been partially addressed in the literature through the use of safety margins. For example, Kerr and Roth [Kerr 86] applied safety margins to the friction and joint torque constraints of a LP force optimization, in the context of fingered grasps. Their work develops a general LP framework for finding optimal force distributions through minimization of various possible cost functions, subject to linear constraints. One such possibility, which they apply to grasping, is to minimize a linear combination of torque ratios and friction cone margins. The selection of appropriate weights for each component

---

[3]The mechanical power for a rotating motor is defined as $P_m = \tau\dot\theta$. On the other hand, the electrical power for a motor can be expressed in its simplest form as $P_e = I^2R$, and the motor stall torque is given by $\tau = K_tI$, where I is the current, R the resistance, and K_t the motor torque constant. Combining these expressions, the electrical power can be rewritten as $P_e = \frac{R}{K_t^2}\tau^2$.

of the cost function is not discussed.

As compared to the work of Kerr and Roth, joint torques in our case are affected by body motion *as well as* optimal force distribution. This makes it applicable to a wider spectrum of robots, with or without active force control capabilities.

The use of fixed safety margins has also been applied to torque constraints. Fixed margins of safety can decrease the robot's susceptibility to saturation, but their adequate selection is far from easy. This is especially true for a robot operating near the upper or lower bounds of the torque regime. In the first case, one risks selecting a margin that is too small. In the second case, requiring an overly large margin might render the optimization infeasible, while realistically there is a solution. In this context, the work presented in this dissertation can be understood as a maximization of safety margin at different stages of the gait.

POSE-BY-POSE ENERGY OPTIMIZATION

Most of the literature involving torques has focused on energy efficiency through minimization of appropriate cost metrics. The most common approach is to select foot force distributions that minimize energy consumption or mechanical power for particular gaits.

Some force-based approaches specifically geared toward walking robots choose to optimize the force distribution at individual *fixed* poses throughout the gait. For example, Cheng and Orin [Cheng 91] developed a fast Linear-Programming technique for optimization of force distribution for general multiple-chain robots, with application to a variety of grasping tasks. The technique is shown to work for different linear cost functions. Of special interest is their optimization for *minimum effort*, defined by a summation of normal force components at the contact points. This cost function is not of type J_1 or J_2, but like them lacks the explicit distancing from saturation. The LP approach naturally arises as the appropriate solution technique in the second part of this dissertation, for the case of robots with force control capabilities. However, it is not applicable when the joint torques are nonlinear functions of the optimization variables, as in the first half of this work.

Marhefka and Orin [Marhefka 98] used a different setup based on quadratic programming to achieve the same objective on walking machines, with specific focus on reducing the energy used by the motors. Quadratic programming is mandated by the use of a J_2 cost function. Their work incorporates constraints on joint torques based on current and voltage limitations of the motors and associated circuitry. However, no attempt to maximize actuation headroom is made.

The work presented in this dissertation follows the pose-by-pose philosophy of the above approaches but differs from them in that the torque redistribution is achieved by lateral, longitudinal and rotational body motion as opposed to internal redistribution with a fixed pose.

ENERGY OPTIMIZATION THROUGH GAIT PARAMETERS

In contrast, other force-based approaches aim to minimize energy consumption by manipulating some of the gait parameters (duty cycle, body height, step length, etc). These are applicable only to regular gaits, for which it is possible to quantify energy consumption per cycle for comparison purposes. For example Marhefka and Orin [Marhefka 97] applied a dynamic simulation technique to select optimal gait parameters of a generic hexapod robot. The authors report energy reductions of up to 50% after modifying the initial gait parameters.

Silva, Machado and Lopes [Silva 06] analyzed the energy efficiency of periodic gaits for quadruped robots as a function of robot velocity. Their focus is on adjusting gait parameters to minimize mean absolute energy density and hip trajectory tracking error. The energy metric is of type J_1, and thus for a given robot velocity would potentially reduce joint torques. This approach is not applicable to discontinuous gaits where the robot does not move at constant speed. It also does not take advantage of swaying motion. Similarly Sufi-Erden and Leblebicioğlu [Erden 06] optimized gait parameters for a wave gait in order to minimize a dissipation function of type J_2. Their approach achieves energy reductions via the modification of gait parameters, and they conclude that the *ipsilateral* [4] phase difference of the standard wave gait must be modified in order to reduce energy dissipation.

---

[4]ipsilateral: same side of the body

BIO-INSPIRED APPROACHES

In the realm of bio-inspired approaches, Kar, Issac and Jayarajan [Kar 01] based their technique on biomechanical studies of cockroaches, which suggest that directing the contact forces toward the *coxal* (hip) joint minimizes joint torques in these insects. The objective to be minimized is the power consumption, but torque limits are not considered. As will be explained later in this dissertation, directing the forces toward the hip can drive some joints closer to saturation, exacerbating the problem being addressed in this dissertation.

Several approaches are based on the use of Central Pattern Generators (CPG). For example, Tsujita, Kawakami and Tsuchiya [Tsujita 04] used simulated annealing to choose appropriate phase differences between CPG oscillators in order to minimize a function of type J_2. Unfortunately this family of techniques assumes very specific de-centralized robot architectures not available in many robots.

DIRECT OPTIMIZATION OF TORQUES

More recently a few approaches have been published that work directly with joint torques instead of forces. Jiang, Liu and Howard [Jiang 04] compared force-based and torque-based approaches, using different pseudo-inverse formulations to determine optimal force distributions between the supporting feet to apply a desired force/torque on the body. The torque-based approach was found to present optimality benefits as measured by the sum of the torques squared.

Similarly, Sufi-Erden and Leblebicioğlu [Erden 07] undertook an energy formulation using joint torques directly, and compared it with the more common foot force distribution setup. The objective was to minimize $Power=J(\tau^2)$ subject to friction constraints for some given, pre-defined gait by redistributing torques among the joints. Their comparison suggests that an optimization based on joint torques directly results in more energy-efficient motions than one dealing with force distributions. For example, a comparison of a full cycle of an alternating tripod gait results in a gait that is almost twice as efficient using the torque approach. One drawback of their approach, however, is that it makes no attempt to avoid motor saturation. In other words,

power minimization does not necessarily imply reducing proximity to saturation.

The above two approaches make use of the fact that it is possible to redistribute torques among the joints of a robotic leg without affecting the force distribution, if sufficient joints are available and rigid contact points are assumed. Therefore better solutions might be found by working directly in the torque domain rather than indirectly through forces.

Gonzalez de Santos et al. [de Santos 05, de Santos 06] included joint torques and electrical power consumption as part of a new stability metric – the global quasi-static stability margin (GSSM), which groups the geometric, torque and electrical current stability margins. The GSSM was then used to select optimal footholds in a free crab gait for quadrupeds and hexapods. As with other approaches that involve weighted combinations of cost, selection of these weights is critical. Also, use of electrical current as an optimization metric is difficult, requiring a sufficiently accurate model of the robot's electrical system in order to be trustworthy. Their work makes extensive use of normalized margins with possible values in the range $[0, 1]$, a philosophy adopted in this dissertation because it provides consistent scaling for cost functions in an optimization setting.

CLIMBING ROBOTS

Some related work also exists in the climbing robots literature. Of note is the work by Miller, Bretl and Rock [Miller 06] on torque redistribution via real-time convex optimization. Here, an optimal distribution of contact forces is found by solving a LP, subject to constraints on the joint torques. The cost function is the weighted sum of torque ratios, and the contact forces are controlled directly via the individual joint torques. As previously mentioned, the second part of this work makes use of a similar optimization setup, but with a different emphasis: maximizing actuation headroom.

SWAY COMPENSATION

None of the above approaches tried to exploit lateral motion or other deviations from a nominal trajectory to reduce torques. To the author's knowledge the only precedent of this is the work of Kurazume et al. [Kurazume 03] on energy efficiency of a quadruped robot. Though not directly dealing with torques, their work introduces 2D and 3D *sway compensation* for the purpose of smoothing out accelerations during dynamically-stable gaits of a quadruped robot (Titan VIII). The authors report reductions in energy consumption (Joules per gait cycle) as compared to a dynamic trot without swaying.

It should be noted that evaluation of robot performance has been traditionally carried out under the assumption of hip trajectories executed at constant velocity. However, as suggested by Silva and Machado [Silva 07], and Alexander [Alexander 84, Alexander 89], hip oscillation is present in animals potentially due to efficiency benefits, and its application in walking machines merits further study.

Chapter 4

Zero-Interaction Gait Optimization

This chapter describes the new optimization procedure that was developed to prevent actuator saturation in walking robots, without making use of the nullspace of forces. The technique finds optimal changes to the body's spatial DOF to alter the force distribution and leg geometry in a way that reduces proximity to saturation. The chapter is organized as follows:

§**4.1** gives some opening remarks.

§**4.2** provides a high-level outline of the approach.

§**4.3** discusses selection of optimization variables.

§**4.4** formalizes the optimization framework.

§**4.5** presents simulation results for individual poses and complete gaits.

§**4.6** discusses how the granularity of the optimization can be increased.

§**4.7** gives a summary of findings and motivates a sensitivity analysis.

4.1   Introduction

Various approaches are possible for gait optimization, depending on the intended objective and available capabilities of the robot. In this work the choice is made to optimize the gait one pose at a time.

This chapter describes the first of the two approaches developed over the course of this research. Its essence is to seek a zero-interaction solution, taking advantage of modifications to the spatial DOF of the robot's body. The technique does not make

use of the nullspace of contact forces. The zero-interaction approach is the safest one in situations where the contact friction coefficients and/or mechanical properties are not well known. The utilization of the null space will be discussed in detail in Chapter 6.

If precise force control is available, the full benefit of the zero-interaction optimized gait can be obtained. In the absence of it, there are limitations on the kind of terrain that can be traversed. The characteristics of the traversable ground will be studied in Chapter 5.

4.2   Outline of Approach

Due to the wide variety of gaits that legged robots may follow in specific situations, the technique presented here is designed to modify an existing gait rather than construct one from scratch. The process begins with the generation of this *reference gait*. A vast literature exists on different approaches to gait generation for specific needs, and a good overview is presented in [de Santos 06]. The optimization is applicable to any statically-stable, discontinuous gait regardless of the number of legs that step simultaneously (applicability to continuous gaits is discussed in Chapter 8).

The reference gait provides a sequence of poses and footfall locations followed by the robot. Of the reference gait, the footfall locations will be preserved intact, but the poses will be modified. Preserving the footfall locations is important in the case of environments with forbidden areas, such as boulder fields.

The modification of poses can be applied at any desired level of *granularity*. For example, during the execution of a step the CG of the robot shifts as the leg is swung forward. A high-granularity approach would optimize the body pose for many intermediate waypoints of the step, resulting in a continuous displacement of the body as the step is executed. It is useful, however, to realize that the peak loads on the legs and joints generally occur during the execution of steps, when one or more feet are in the air. For this reason, a low-granularity approach is followed in the remainder of this work, finding ideal body poses *before* each step is executed such that when the corresponding foot is picked up the maximum observed torque ratio is as low as

possible. A discussion on how to increase the optimization granularity is provided in §4.6.

After applying the optimization to individual steps along the gait, consecutive optimized poses can be connected by straight line body motions that constitute the new body shifts.

In order to avoid unnecessary computations the optimization is applied to the *skeleton* gait. That is, the gait that contains all the footfall locations and body shifts, but for which the individual steps haven't been planned in detail using SBL or any other motion planner (see §3.5). The reason is that the swaying motion applied by this optimization changes the configuration of the robot and its position relative to the ground and obstacles, which would require individual steps to be replanned anyway in order to prevent collisions.

The following example further clarifies the zero-interaction optimization process. Figure 4.1(a) shows the top view of a robot about to step with leg 6 (top right). The contour plot shows the variation of $\tau_{\%,max}$ over all the joints of the legs in contact as a function of the body position (x_b, y_b). The center of the body is indicated by the green dot, and starts at $(0, 0)$. If no optimization is applied the step would be executed from this original pose. However, as the contour plot shows, the maximum torque ratio can be reduced if the center of the body is shifted to the position indicated as $(x_b, y_b)^*$ before executing the step, as shown in Figure 4.1(b).

The procedure shown in the previous figure is applied to each of the steps along the desired traverse, resulting in a sequence of optimal poses for the execution of the steps. The motion of the body needed to connect two consecutive optimal poses constitutes the new body shift between steps, as shown in Figure 4.2.

Note that the precise shape of the $\tau_{\%,max}$ contour depends on the force distribution and the geometry of the legs. These change every time the robot moves, so the optimal offsets $(\Delta x_b, \Delta y_b)^*$ must be found by an optimization for each step. This is explained in the rest of this chapter.

The optimal body pose is generally *not* located at the centroid of the support polygon. The reason is that the value of torque depends on the load distribution as well as the geometry of the legs. Thus even though centering the CG inside the

(a) Before body shift   (b) After body shift
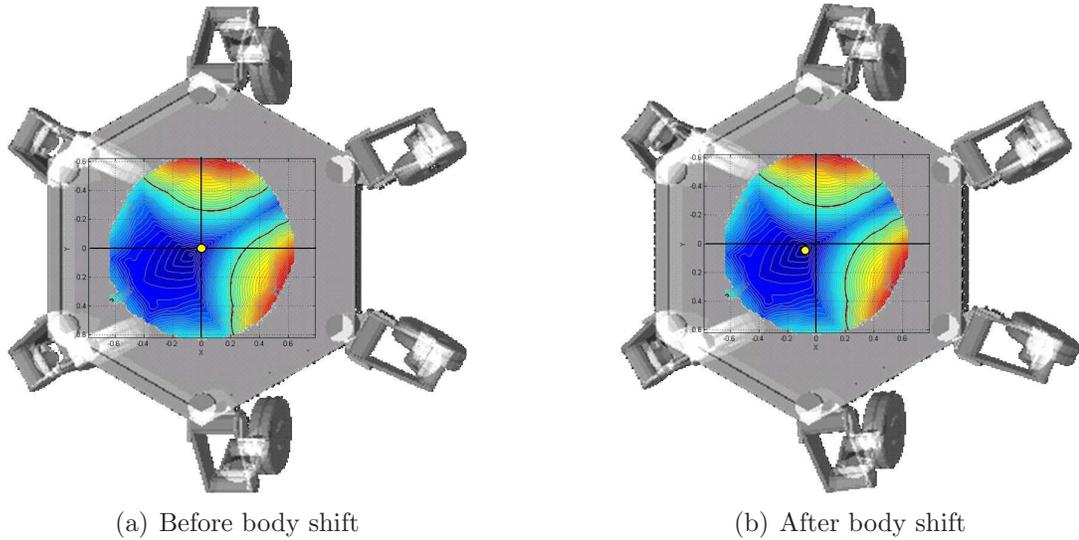
Figure 4.1: **Contours of $\tau_{\%,max}$ for the first step of a gait. To move away from saturation, the body is shifted to $(x_b, y_b)^*$ before executing the step.**

support polygon would result in an even distribution of forces, the geometry of each of the legs will in general be different, producing different sets of torques.

4.3 Optimization Variables

The body of a walking robot has 6 spatial degrees of freedom (DOF). It is possible to harness as many of these DOF as appropriate to prevent saturation.

If the robot is transporting inert cargo, variations in chassis tilt and height might be acceptable. In this case it would be acceptable to exploit all six DOF and use $(\Delta x_b, \Delta y_b, \Delta z_b, \Delta \phi_b, \Delta \theta_b, \Delta \psi_b)$ as the design variables. On the other hand manned applications may require maintaining a steadier platform, in which case it would be more appropriate to use $(\Delta x_b, \Delta y_b, \Delta \psi_b)$, or perhaps only $(\Delta x_b, \Delta y_b)$ as optimization variables while maintaining the other DOF constant.

If lateral motion is deemed undesirable for reasons of crew comfort or traversal of a narrow passage, a benefit can still be obtained from an optimization on Δx_b only. The result is a gait whose body shift lengths are adjusted to decrease torque requirements. This will be illustrated in §4.5 when simulation results are presented.

(a) 1$^{\text{st}}$ optimal pose   (b) 2$^{\text{nd}}$ optimal pose
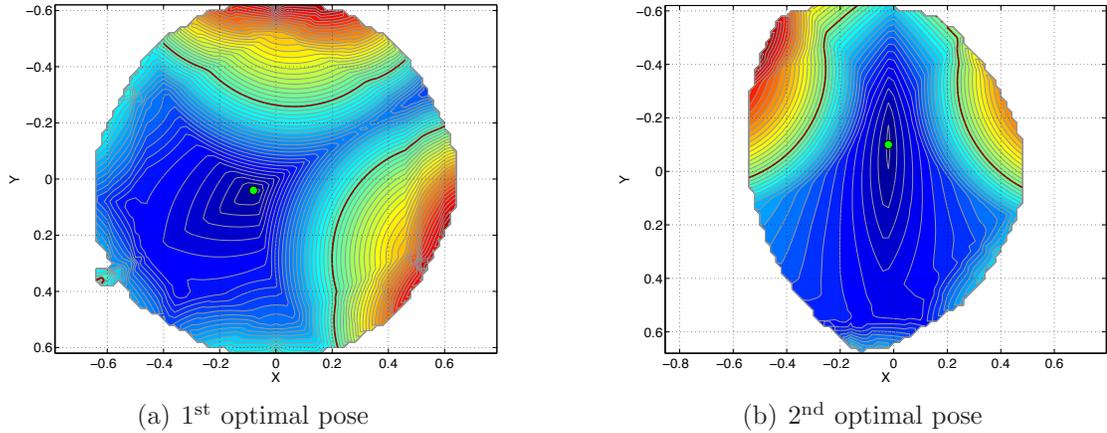
Figure 4.2: **Connection of two consecutive optimal poses results in the new body shift for the swaying gait**

Regarding the use of Δz_b, the height of the body above the ground has a direct impact on a leg's reachable area. A larger reach can allow bigger $(\Delta x_b, \Delta y_b)$ body shifts which may reduce torques further. Therefore for a given start configuration and target footfall there is an optimal body height or range of heights that enable larger torque reductions. A gait that includes optimization over Δz_b would present cyclical variations of body height as the robot walks.

The present work was carried out in the context of a manned robot, so it has been deemed desirable to keep (z_b, ϕ_b, θ_b) constant for crew comfort, and take advantage of $(\Delta x_b, \Delta y_b, \Delta \psi_b)$ for optimization. The approach, however, is valid in the general case of using all the body DOF subject to appropriate constraints.

It is noted that the benefit obtained from the rotational degrees of freedom can be expected to be comparatively small. This is primarily because they do not shift the CM of the robot considerably if at all, so the force distribution sees little change. The benefit of these DOF comes from the modification of the leg geometries and the different set of moment arms that result. In some cases they also extend the body translations that are possible, enabling a greater benefit from $(\Delta x_b, \Delta y_b, \Delta z_b)$.

The achievable reduction in $\tau_{\%,max}$ for a given step largely depends on the geometry of the legs in contact and how much motion of the body they allow. For example, Figure 4.3 shows a very constrained pose for the ATHLETE robot, informally called

(a) ATHLETE in MSP pose

(b) Contour of $\tau_{\%,max}$
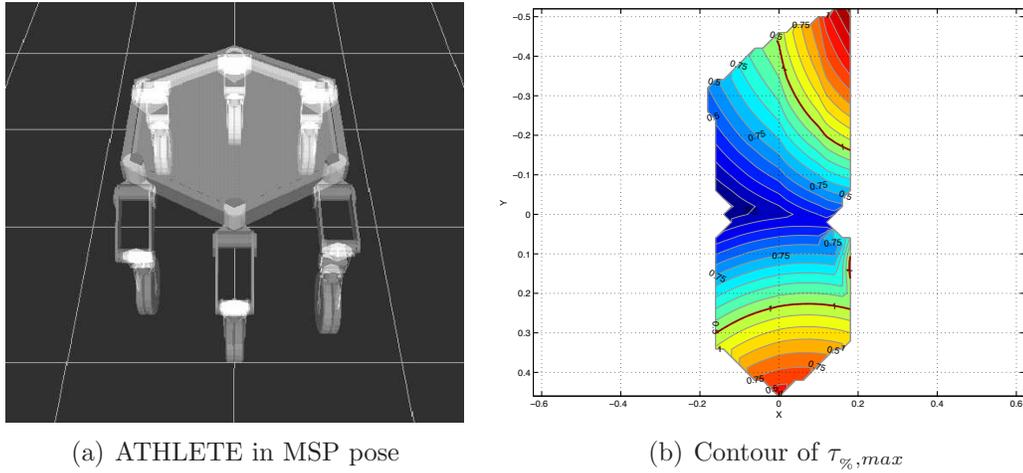
Figure 4.3: **A very constrained configuration for a legged robot can prevent motion in a direction of interest and limit the possible reduction in $\tau_{\%,max}$.**

the Marsyard Standard Pose (MSP). In this example, four of the legs are tucked in to narrow the form factor of the robot so that it can be stored in a reduced space. Because these legs are close to some of their joint limits, displacement is limited along the X direction (left-right here) and the minimum torque achievable is pegged at the extreme of motion. Had the joint angle limits been less constrained, it might have been possible to move further from saturation.

The above discussion suggests the interesting possibility that one might exploit the multiple inverse kinematic (IK) solutions that exist for a 6-jointed leg to reach the same point in space. By selecting a different IK solution for some of the legs it might be possible to shift the body further in a beneficial direction. Generally speaking these multiple IK solutions are not connected in configuration space; in other words, except in special cases it is not possible to take the leg from one IK solution to another without moving the foot or hip. Therefore, a sequence of body moves might be necessary to achieve this extra benefit. The utilization of IK multiplicity was not explored in this work.

4.4 Optimization Framework

To begin, the torque ratio for joint i is defined as follows, assuming that the maximum available torque is the same in the positive and negative directions:

$$\tau_{\%,i} = \left| \frac{\tau_i}{\tau_{max,i}} \right| \qquad (4.1)$$

The torque ratio represents the percentage of maximum torque capacity being requested from a certain joint. By extension, the actuation margin for the same joint is defined as follows:

$$M_{\tau,i} = 1 - \tau_{\%,i} \qquad (4.2)$$

The actuation margin is a metric of how *far* from saturation a given joint is. A value of $\tau_{\%,i} \geq 1$, or equivalently $M_{\tau,i} \leq 0$ denotes a saturated motor. Since the objective is to maximize the actuation margin for all joints the cost function to be *minimized* is the following:

$$J = \|\tau_{\%,1}, \ldots, \tau_{\%,n}\|_\infty \qquad (4.3)$$

That is, cost is represented by the maximum of all torque ratios. The problem has a form similar to the Chebyshev approximate solution of a linear system, which can be stated as follows [Boyd 04]:

$$\text{Minimize } max_{i=1\ldots k} \left| a_i^T x - b_i \right| \qquad (4.4)$$

Where $a_i^T \in \Re^n$, $x \in \Re^n$ and $b_i \in \Re$. The Chebyshev solution is very similar to least-squares – they both provide approximate solutions to the equation $Ax = b$, by minimizing different quantities. In the Chebyshev case the cost function is not differentiable (i.e. it is non-smooth). Therefore instead of attempting to solve it in the form shown by Equation 4.4 it is usually transformed into an equivalent linear program (LP), for which solution techniques abound.

The cost function from Equation 4.3 is structurally similar to Equation 4.4. In

both cases the non-differentiable infinity-norm is present. Unfortunately in Equation 4.3 the argument is nonlinear and non-convex, so LP does not apply. However the transformation process applied to the Chebyshev problem to convert it into a LP can and will be rescued here to obtain cost function smoothness.

The issue of non-linearity can be addressed by use of a nonlinear programming technique (e.g. Sequential Quadratic Programming). Finally, the cost function is non-convex, meaning that it has multiple local minima. Local optimizers can become trapped in these, complicating the successful discovery of the global minimum. To investigate how this affects the problem at hand, exhaustive searches have been conducted on Equation 4.3 for a variety of robot poses. These searches revealed a benign nature with a strong local minimum near the starting pose (Figure 4.4). Therefore, by providing the optimizer with an initial guess corresponding to the starting pose, convergence to the global minimum was achieved in all the cases that were studied.

(a) 1st Step

(b) 2nd Step

(c) 3rd Step

(d) 4th Step

(e) 5th Step

(f) 6th Step

Figure 4.4: **Contours of $\tau_{\%,max}$ for the first 6 steps of a gait. Note the presence of one strong local minimum in all cases, indicated by the green dots.**

With the above discussion in mind, the original problem will be transformed into a smooth, differentiable one which can be solved by means of SQP. This is accomplished with the following equivalent problem:

Minimize:

$$J = t; \qquad \text{t: scalar} \tag{4.5}$$

Given the design vector:

$$\mathbf{X} = \{\Delta x_b, \Delta y_b, \Delta z_b, \Delta \phi_b, \Delta \theta_b, \Delta \psi_b, t\} \tag{4.6}$$

s.t.:

$$t \; \leq \; 1 \tag{4.7}$$

$$\tau_{\%,1} \; \leq \; t$$
$$\vdots \tag{4.8}$$
$$\tau_{\%,n} \; \leq \; t$$

The cost is now a linear function of the design variables, but joint torques τ_i remain nonlinear functions of $(x_b, y_b, z_b, \phi_b, \theta_b, \psi_b)$. Thus the overall problem consists of a linear cost function subject to nonlinear constraints.

The optimization is also subject to *reachability constraints*. Given an initial set of contact points expressed in the robot frame {R}, the new position of each contact point after a body translation and rotation is obtained by applying the transformation matrix in Equation 4.9. The points on the ground will experience a motion *opposite*

to that of the body, as seen in the {R} frame. [1], [2]

$$T = \begin{bmatrix} c\Theta c\Psi & s\Phi s\Theta c\Psi + c\Phi s\Psi & -c\Phi s\Theta c\Psi + s\Phi s\Psi & -\Delta x_b \\ -c\Theta s\Psi & -s\Phi s\Theta s\Psi + c\Phi c\Psi & c\Phi s\Theta s\Psi + s\Phi c\Psi & -\Delta y_b \\ s\Theta & -c\Phi s\Theta & c\Phi c\Theta & -\Delta z_b \\ 0 & 0 & 0 & 1 \end{bmatrix} \tag{4.9}$$

If the optimization variables are $(\Delta x_b, \Delta y_b, \Delta \psi_b)$ this becomes:

$$T = \begin{bmatrix} c\Psi & s\Psi & 0 & -\Delta x_b \\ -s\Psi & c\Psi & 0 & -\Delta y_b \\ 0 & 0 & 1 & 0 \\ 0 & 0 & 0 & 1 \end{bmatrix} \tag{4.10}$$

Defining the maximum reach for all legs $\rho_{max,i}$, and using the transformation matrix T, the reachability constraints can be written as follows:

$$\| \vec{r}_{L,i} - T \cdot \vec{r}_{c,i}^{\,T} \| \leq \rho_{max,i} \tag{4.11}$$

Where:

$\vec{r}_{L,i}$: Location of $\{L\}_i$ expressed in $\{R\}$.

$\vec{r}_{c,i}$: Initial location of contact point i in $\{R\}$.

This is illustrated in Figure 4.5. The points A and B in this figure denote the initial and final foot locations of the leg that takes a step. The remaining static footholds as well as A, B must remain within the reachable area of the appropriate leg (exemplified by the dashed pie wedge).

Equation (4.11) is nonlinear and non-convex due to the presence of trigonometric functions of $\Delta \psi_b$. Summarizing, the properties of the optimization constraints place the problem in the realm of nonlinear optimization. Various techniques exist for solving this optimization problem, and for this work Sequential Quadratic Programming

---

[1] In the interest of readability, s represents the sin() function, and c the cos() function. Similarly, the angular displacements are expressed in short form, with the following equivalence: $\Delta\phi_b \rightarrow \Phi$, $\Delta\theta_b \rightarrow \Theta$, $\Delta\psi_b \rightarrow \Psi$.

[2] The expression has been simplified by recalling that for any angle ζ it holds that $\sin(-\zeta) = -\sin(\zeta)$ and $\cos(-\zeta) = \cos(\zeta)$. The original expression can be found in [Craig 89], p46.

(a) Original pose   (b) Pose after translation, rotation

Figure 4.5: **Reachability constraints for an optimized pose.**

(SQP) was chosen. Specifically a C++ implementation called SNOPT [Gill 02] is used. The SQP algorithm is described in [Nash 96] and others.

At this point the optimization problem is fully defined. Once the set of optimization variables is chosen, the problem can be solved using the technique described above. The following section describes simulation results for a reverse-wave gait being executed by the ATHLETE robot.

4.5 Simulation Results

4.5.1 Description of Experiments

The simulations begin with ATHLETE in the preferred driving configuration on flat, horizontal ground as shown in Figure 4.6. This pose is symmetric, with all the legs in the same configuration, and the top of the body 2m above the ground. In the image, leg 1 is indicated by the red dot. The robot is commanded to walk 5m out face 1 (see Figure 2.5), which is toward the right in this case.

The resulting motion and torque variation is studied for two cases: the reference gait without any optimization, and the gait optimized with $(\Delta x_b, \Delta y_b, \Delta \psi_b)$. This subset of design variables was chosen for the ATHLETE robot because it preserves the body height and roll/pitch angles, providing a stable platform for manned applications.

Figure 4.6: **Starting pose and terrain for the gait optimization simulations.**

4.5.2   Simulator Description

For the purpose of gait analysis and design, a simulation environment called GaitView was developed. The simulator and its supporting libraries were written in C++. The main features that were incorporated into the simulator include:

- Realistic 3D visualization of the robot and its motion, with image capture capabilities.

- Ability to load multiple terrain meshes simultaneously.

- Calculation and visualization of contact forces and joint torques.

- Ability to load and replay telemetry logs from ATHLETE field tests.

- Gait planning and execution.

Figure 4.7 provides two screenshots of GaitView. The user interface was implemented using QT4 [Nokia 09]. This provides a large number of pre-designed widgets which make it easy to extend the interface if new capabilities are required, as was the case many times throughout this research.

Interactive 3D visualization was achieved with OpenGL, via the QGLViewer library [Debunne. 09]. QGLViewer enables very intuitive interaction with the 3D models, including rotation, translation, zoom in/out, fly in/out, redefinition of the center of rotation, image capture, and many others. The library also interfaces easily with

QT, requiring only that the user redefine the *draw()* function to render the models via OpenGL commands.

Some of the drawing functionality in GaitView was inherited from a previous simulator developed by Kris Hauser and other members of Prof. Jean Claude Latombe's research group at Stanford University. Their group also kindly provided the SBL library which was used for individual step planning.

Collision checking is accomplished via the Proximity Query Package (PQP), developed at the University of North Carolina [UNC 99, Gottschalk 96, Larsen 99]. PQP is used to check for self-collisions and collisions with the environment.

Dynamic simulation capabilities are currently not available in GaitView, but could be added in future versions via the Open Dynamics Engine (ODE) [Smith 07].

(a) Force/torque analysis

(b) Telemetry analysis

Figure 4.7: **Two screenshots of GaitView 1.0.**

4.5.3 Unoptimized Reference Gait

A discontinuous, reverse wave gait was chosen as a reference for the work with ATH-LETE because it maximizes the distance between consecutive feet, which is useful for avoiding self-collisions. However, as mentioned before, the technique presented here is not dependent on the use of this specific gait.

The preferred directions of motion for ATHLETE are toward any of the 6 faces of the hexagonal body, because stereo cameras are available looking directly out of each face. The simulation results presented in this section correspond to a motion in the direction of Face 1, as shown in Figure 4.8. For this gait and direction of motion, the sequence of steps is {6-5-4-1-2-3}, with a body shift after each step. The total displacement of the body is 5m, which results in a total of 34 steps (5 complete gait cycles plus 4 extra steps).

Figure 4.9 shows the first 2 gait cycles of the reverse wave gait. Each blue dot represents the position of the center of the body after a body shift. The steps are indicated by curved, solid arrows, and the body shifts by straight, dashed arrows. After the second gait cycle, the motion converges to a regular, periodic pattern. At this point all the body shifts are of equal length, and so are the steps.

Figure 4.8: **Step sequence of a reverse wave gait**

Figure 4.9: **First 2 cycles of a reverse wave gait**

VARIATION OF $\tau_{\%,max}$

In order to establish a point of comparison for the subsequent optimizations the variation of $\tau_{\%,max}$ throughout the reference gait is analyzed here. A special shorthand notation has been devised to clarify what move each data point corresponds to in the plots of $\tau_{\%,max}$. This notation is summarized in the following Table:

Symbol	Meaning
$\uparrow \#$	Lifting of foot $\#$
$\rightarrow$	Forward swing of the lifted foot
$\downarrow$	Planting of the lifted foot
$\leftrightarrow$	Body shift

Table 4.1: **Shorthand notation to indicate moves in plots of** $\tau_{\%,max}$

Figure 4.10 shows this variation for the first 3m of the traverse. This includes a total of 3.5 gait cycles, for a total of 21 steps and an equal number of body shifts. Starting from the third cycle the behavior becomes regular, so the remaining 2m of the traverse are not shown to improve readability.

The following observations can be made about the behavior observed in Figure 4.10 for each of the first three cycles:

First cycle: First it is evident that the peaks correspond to the instances when a foot is in the air. A relatively small variation is observed between the two points of each peak (10% in the worst case). This variation is a result of the CM being shifted during the swing since the legs have significant mass. **Second**, a gradual increase exists from the 1st to the 5th peak. This curious behavior can be attributed to the fact that as the first cycle progresses the spread of the two legs adjacent to the one in motion also increases (verifiable by carefully observing the first 5 steps in Figure 4.9). By the 6th all the feet in contact have taken a step, and the configuration is again more symmetric, causing the observed decrease.

Second cycle: Starting from this cycle the pattern changes and exhibits two high

Figure 4.10: **Variation of $\tau_{\%,max}$ for the reference gait**

peaks followed by a low one – a kind of symmetry between the left and right sides of the body. The critical steps are the first and second ones on each side.

Third+ cycle: Since the chosen gait is periodic, the variation of maximum torque ratio repeats exactly from the third cycle on. For verification the first 3 steps of the third and fourth cycles may be compared.

4.5.4 Full Gait Optimization Using $(\Delta x_b, \Delta y_b, \Delta \psi_b)$

It is now possible to apply the above optimization to each pose along the reference gait studied in §4.5.3. The optimization is applied to this skeleton reverse-wave gait.

As mentioned the poses can be optimized at any level of granularity desired. Here the choice has been made to optimize only the steps. During the execution of a step the torque ratios constantly change because the location of the CG moves as the leg is swept forward, modifying the load distribution among the legs that remain in contact. The percentage torque variation between the lift and drop waypoints, however, is small enough that it was deemed sufficient to optimize the body pose

only at the beginning of each step, when the leg has reached its *lift waypoint* q_L (Figure 4.11). Therefore the body will be shifted to its optimal pose before initiating a step, and will remain there during the entire motion of the stepping leg.

As the results will show, this approach achieves the desired reductions in torque percentages while preventing too much computation. A discussion on how to increase the level of granularity is provided in §4.6.

Figure 4.11: **Stages in the execution of a step – ① Lift, ② Collision-free planned move, ③ Drop. The waypoints of interest are** q_I**: Initial configuration,** q_L**: Lift waypoint,** q_D**: Drop waypoint,** q_G**: Goal configuration.**

OPTIMIZED MOTION

Figure 4.12 shows a comparison of the optimized and reference motions of the robot. Each blue point along the path represents the location of the center of the chassis at the beginning or end of a body shift. The first of these points is the initial location of the body. The line segments connecting these points correspond to the body shifts themselves. In the reference case, each point also corresponds to a step taken with the corresponding leg in the sequence, since steps are executed at the end of each shift. This is also true for the optimized motion, with the exception of the first point, because in this case the robot executes a body shift before executing a step.

As can be seen in the figure, the swaying motion becomes periodic after three gait cycles. This is expected since the reference gait is also periodic. Here the underlying behavior is easier to understand – once the gait becomes periodic near the end of

Figure 4.12: **Comparison of optimized (top) and reference gaits for the ATHLETE robot.**

the 2nd cycle the body is moved away from the stepping side. That is, before the legs on the *left* side of the body take steps, a large sway toward the *right* occurs, and viceversa. Figure 4.13 shows a montage of the first 2 cycles of the optimized sway gait. The behavior just mentioned as well as the directions of the body shifts can be appreciated here.

Figure 4.13: **First 2 cycles of the optimized sway gait**

EFFECT ON SATURATION

The variation of $\tau_{\%,max}$ for the optimized (sway) gait is plotted in Figure 4.14, with the reference values shown for comparison. The following observations can be made from this plot:

1. The sway optimization has succeeded in reducing all the peaks by different amounts. The largest reduction ($\approx 50\%$) is seen at the 1st step of the gait once it has become regular after the 3rd cycle.

2. More importantly, the maximum peak which previously reached saturation has been reduced by 23%, preventing saturation with a comfortable margin.

3. After the 3rd cycle, the reference gait experienced maximum peaks > 90%. By applying sway, the maximum peaks have been reduced to $\approx 70\%$. This is important because the benefit of sway is not limited to the critical 1st cycle, but is seen in the long-term operation of the robot.

4. It can be seen that the distribution of peaks has changed in the steady state. Instead of 2 high peaks followed by a low one, the new pattern is 1 high peak surrounded by 2 low ones. This means that the new critical steps are the second ones on each side, when the adjacent legs are at their maximum spread (see Figure 4.13).

4.6   Increasing Optimization Granularity

The optimization presented in this chapter can be applied to the gait at higher granularity if desired. This process is not difficult, but requires some thought to understand the necessary actions and consequences.

The level of granularity used in the above simulations and experiments assumes that the variation of torques during a step is small. In some cases better results can be obtained by optimizing the body position at several waypoints of the leg swing. Similarly, a choice has been made to execute straight-line body shifts between optimal

Figure 4.14: **Variation of $\tau_{\%,max}$ for the sway gait. The values for the reference gait are shown for comparison.**

poses. It would be possible, however, to find an optimal path between consecutive robot poses to minimize the maximum torque ratios throughout the shift.

OPTIMIZATION OF STEPS

For simplicity the optimization presented above was carried out including reachability constraints for the 4 essential waypoints of a step: initial footfall, lift waypoint, drop waypoint and target footfall. This guarantees that the resulting body shifts will allow execution of the steps without the need for additional moves. In proceeding like this, only one optimization is solved per step. For this optimization, an assumption must be made as to whether the stepping leg is in the initial, lift, drop or target configuration. Since it was observed that higher torque ratios tend to be present at the lift waypoint, this configuration was used during optimization.

The tradeoff is that the variation of torque ratios during step execution is not fully captured. Therefore, the body position might not be optimal for the rest of the waypoints (though it will be close to optimal). A first option for improvement is to

start with two optimizations per step:

1. One with the stepping leg in the lift waypoint configuration, and excluding the drop and target waypoints from the reachability constraints.

2. A second one that excludes the start and lift waypoints, and uses the drop waypoint configuration for the stepping leg.

The above would provide two optimal robot configurations to be connected. If no obstacles (e.g. boulders) are in the vicinity of the stepping leg and the robot is on approximately horizontal ground, it is then possible to generate a C-space motion plan to execute the step, avoiding only a ground modeled as a flat plane. This produces a list of waypoints for that leg, and an optimal body pose can be computed via optimization with the stepping leg at each of these configurations. The start, lift, drop and goal waypoints can be excluded from reachability for these optimizations.

The procedure outlined above will yield optimal body poses for the specific motion plan generated for the leg. However, it says nothing about whether that plan is optimal in the sense of torque percentage minimization, or if a better plan may be found. In any case, it is unclear if a sufficiently large reduction in torque ratios could be obtained to justify the significant computational overhead. This is a possible avenue for future research.

The problem of generating the C-space motion plan for the leg is more difficult if there are obstacles to avoid along the way. In the previous scenario the ground could be modeled as a horizontal plane, meaning that the terrain mesh as seen in the {L} frame is invariant to body shifts. With more complex terrain, this can no longer be assumed to be the case. Thus a set of waypoints for the leg computed from a given body pose may result in collisions once the body is shifted to a slightly different location.

Numerous approaches are conceivable in this case and the tradeoffs should be weighed carefully to prevent unproductive computation. One possibility is to plan the step incrementally: make an initial plan connecting the lift and drop waypoints, then proceed as in the flat horizontal ground case, optimizing the body pose for each

waypoint until a collision is detected, say at waypoint p. At this point, replan to connect p and the drop configuration, continuing as above until a feasible plan is found.

As in the previous case, optimality is only guaranteed in the context of the motion plan obtained. However in very complex terrain finding a feasible plan might already be sufficiently difficult, making further optimization a decision to be weighed very carefully.

OPTIMIZATION OF BODY SHIFTS

Optimal body shifts can be accomplished by discretizing the motion of the body along the desired direction of motion, and finding the optimal values for the remaining degrees of freedom. That is, given a body shift between two consecutive optimal configurations $(x_{b,0}, y_{b,0}, z_{b,0}, \phi_{b,0}, \theta_{b,0}, \psi_{b,0})^*$ and $(x_{b,f}, y_{b,f}, z_{b,f}, \phi_{b,f}, \theta_{b,f}, \psi_{b,f})^*$ it is possible to perform k optimization steps as summarized in Algorithm 1 (the direction of motion is assumed to be x in this example). The resulting sequence of body configurations provide a piecewise-linear approximation to the optimal body shift.

Algorithm 1 Optimize a body shift

Require: k {Optimization granularity}
 1: $\Delta x_b \leftarrow \dfrac{x_{b,f} - x_{b,0}}{k}$.
 2: $x_b \leftarrow x_{b,0}$
 3: **while** $x_b < x_{b,f}$ **do**
 4: $\quad (\Delta y_b, \Delta z_b, \Delta \phi_b, \Delta \theta_b, \Delta \psi_b)_i^* \leftarrow$ Optimize at x_b
 5: $\quad x_b \leftarrow x_b + \Delta x_b$
 6: **end while**

4.7 Summary

This chapter presented an optimization technique to prevent joint saturation in legged robots by means of specialized motions of the body. The resulting sway gait was

shown in simulation to have the benefit of preventing saturation and reducing the peak torque ratios in the steady-state gait.

The results presented here assume that *zero-interaction* walking takes place. Robots equipped with active force control capabilities will be able to obtain the full benefit of the sway gait. In the absence of force control the robot is commanded exclusively through joint angles, and the achievable benefit depends on the accuracy of the robot and ground models, as well as the deviations that these present. The following chapter will examine the sensitivity of the sway gait to variations in contact force magnitude and terrain characteristics.

Chapter 5

Force-Torque Sensitivity Analysis

The previous chapter outlined a technique for torque minimization that relies on the assumption that tangential forces are close to zero, and normal forces conform to those calculated for the mass-spring system balance at a given robot configuration. This chapter examines the effect that deviations from these nominal forces have on joint saturation, and how this translates into terrain properties. The chapter is organized as follows:

§**5.1** derives the general sensitivity equations.

§**5.2** examines the sensitivity variation for the ATHLETE robot during execution of the optimized sway gait.

§**5.3** describes the calculation of tolerable contact force deviations, and how these translate into traversable terrain characteristics.

§**5.4** summarizes the key lessons from the sensitivity analysis.

5.1   Preliminaries

In the absence of an active force control system, the robot is commanded exclusively through joint angles. The joint torques depend on the external forces and moments applied at each foot, and unmodeled external factors can alter these forces. It is assumed that the contact points are unable to exert moments (meaning the moments are all *zero*), so the joint torques are functions of the vertical force f_z and the tangential forces f_x, f_y only.

The analysis begins with the well-known equation relating joint torques to external forces:

$$\vec{\tau} = J^T \vec{F} \tag{2.15}$$

The force/moment vector is of dimension 6×1, and in the case of ATHLETE which has 6 joints per leg, the transpose of the Jacobian is 6×6 and the torque vector is 6×1. The variation of torque as a function of force is linear, and it follows that the (i, j) component of J^T represents the slope of the line relating τ_i to f_j. In other words, $J^T(i, j)$ is the *sensitivity* of joint i's torque to variations in force j. For convenience, this sensitivity is denoted as $S_{i,j}$ [1]:

$$S_{i,j} = J^T_{i,j} \tag{5.1}$$

In the context of preventing joint saturation, Equation 5.1 is insufficient because it relates to the torque value, rather than the percentage of maximum allowable torque for a given joint. To correct this, recall that the percent torque is given as:

$$\tau_{\%i} = \left| \frac{\tau_i}{\tau_{max,i}} \right| \tag{5.2}$$

$$\therefore \tau_{\%i} = \left| \frac{1}{\tau_{max,i}} J^T_{i,j} f_j \right| \tag{5.3}$$

And the sensitivity of $\tau_{\%i}$ to changes in f_j can now be written as:

$$S_{\%i,j} = \frac{1}{\tau_{max,i}} \left| J^T_{i,j} \right| \tag{5.4}$$

---

[1]The index j in $S_{i,j}$ is replaced here with the appropriate letter rather than a numerical index. For example $S_{1,z}$ is the sensitivity of joint torque 1 to f_z. This could equivalently be denoted $S_{1,3}$ if the force components are numbered from $1 - 3$

5.2 Sensitivity Throughout a Gait

It can be seen that Equation 5.4 is a function of the leg's geometry at a given instant in time, scaled by the maximum allowable torque for that joint. A way to think about it is that the moment arms of forces applied at the foot vary with geometry, and so does their impact on the torque of a given joint.

It follows that sensitivity varies throughout the execution of a gait. For this reason, it is necessary to explore how this variation takes place. The equations described in §5.1 can be applied to any walking robot executing a statically-stable gait.

Here the sensitivity for the reference gait of the ATHLETE robot is analyzed and compared to the optimized gait. This is done for two different groups of legs: "forward-facing" and "side-facing". These groups are illustrated in Figure 5.1, and they represent legs that, due to symmetry, experience similar configurations throughout the gait.

Figure 5.1: **Forward and side-facing legs.**

5.2.1 Forward-Facing Legs

Figure 5.2 shows the variation of *maximum* vertical and tangential sensitivities for forward-facing legs during the first 3 gait cycles of the reference and optimized gaits. In both cases, it is evident that the sensitivity in the vertical direction is very small compared to the tangential direction. Furthermore, of the tangential sensitivities the one in the X direction is the highest for most of the gait.

(a) Reference

(b) Optimized

Figure 5.2: **Sensitivity variations for forward-facing legs throughout reference and optimized gaits.**

No significant difference exists between the sensitivities before and after torque minimization. The peak sensitivities remain approximately the same, with only a slight reduction in the peak-to-peak sensitivity for the tangential directions.

5.2.2 Side-Facing Legs

Figure 5.3 shows the sensitivity variations for the side-facing legs. As with the forward-facing legs, it is observed that the vertical sensitivity always remains well below the tangential ones, and that the sensitivity in the $\hat{X}$ direction is greatest.

Comparing as before the sensitivity before and after torque optimization, the peaks in the $\hat{X}$ direction are seem to be basically unaffected. However, the peak sensitivity in the $\hat{Y}$ has increased by about 15%, and in the $\hat{Z}$ direction by about 20%. These increases are not drastic, but are worth keeping in mind as trade-offs of torque minimization.

5.2.3 Discussion

The results of the previous analysis show that variations in the magnitude of contact forces can have a large impact on saturation, especially in the tangential direction.

(a) Reference   (b) Optimized

Figure 5.3: **Sensitivity variations for side-facing legs throughout reference and optimized gaits.**

This has two primary implications for walking robots.

First, it motivates the implementation of active force control when possible. If cost or other reasons limit sensor availability, the priority should be given to tangential force control. Second, it suggests a careful analysis of the factors that may introduce variations in the contact forces. These include terrain imperfections, robot model uncertainty, sensor accuracy and controller accuracy.

The information contained in Figures 5.2 and 5.3 provides a high-level picture of the *gains* in different directions. However this information is insufficient to determine what kind of terrain can be traversed, or to tackle practical aspects of sensor selection or controller tuning. This is owing to the fact that the *magnitude* of the contact forces also plays a central role, so a direction with very low gain but large applied force can just as easily cause saturation. In the next two sections, terrain characteristics and sensor selection will be discussed in more detail.

The procedure to analyze either of these cases is similar: first, the sensitivities at the different stages of the gait must be determined as outlined in the previous section. The magnitudes of the vertical contact forces must also be quantified; this requires only kinematic information if the assumption of zero interaction is made.

With this in hand the analysis can then turn to individual cases: variations in the normal direction only, or normal and tangential needed to induce saturation.

In fact when normal and tangential forces are present they may all contribute to joint saturation. For simplicity the effect of normal forces may be studied independently under the assumption of zero interaction. However, the tangential direction can only be studied for some known distribution of normal forces. This is because tangential forces can only be exerted with the leg in contact with the ground, which implies non-zero normal force.

Normal Forces

Because a vertical nullspace exists for robots with ≥ 4 legs the number of force combinations for static equilibrium is by definition infinite. However, an approximate analysis can be done by looking at each leg independently as follows: *at timestep $\boldsymbol{t}$, given a nominal value of f_z, a sensitivity $S_{F_z,max}$ for the critical joint in the leg, and its corresponding torque limit τ_{max}, how much additional normal force Δf_z^* is needed to drive the critical joint to saturation?* This is discussed in §5.3.1.

Tangential Forces

Looking now at variations of tangential forces *only*, the question to answer is: *at timestep $\boldsymbol{t}$, given a $\boldsymbol{known}$ value of f_z, the sensitivies $S_{i,x}, S_{i,y}, S_{i,z}$ for all the joints in the leg, and the torque limits $\tau_{max,i}$, how much additional tangential force (Δf_x^* $\boldsymbol{or}$ Δf_y^*) is needed to drive the critical joint to saturation?* The analysis is carried out one direction at a time. This is discussed in §5.3.4.

5.3 Acceptable Force Deviations

This section describes the method to calculate the variations in contact forces that can be tolerated by the robot without causing joint saturation. The analysis is applied to the optimized sway gait, and the results will be translated into terrain characteristics in the following section.

5.3.1 Normal Force f_z

When joint i reaches saturation the following equation is satisfied, keeping in mind that gravity torques are present for massive legs [2]:

$$\left| J_{i,z}^T f_{z,i} + \tau_{g,i} \right| = \left| \tau_{max,i} \right| \tag{5.5}$$

This equation can be satisfied with a positive or negative value of $f_{z,i}$. The two values of critical force can be obtained by solving each of the following equations separately for $f_{z,i}$:

$$J_{i,z}^T f_{z,i} + \tau_{g,i} = \tau_{max,i} \tag{5.6}$$

$$J_{i,z}^T f_{z,i} + \tau_{g,i} = -\tau_{max,i} \tag{5.7}$$

It follows that:

$$f_{z,i,1}^* = \frac{\tau_{max,i} - \tau_{g,i}}{J_{i,z}^T} \tag{5.8}$$

$$f_{z,i,2}^* = \frac{-\tau_{max,i} - \tau_{g,i}}{J_{i,z}^T} \tag{5.9}$$

Given that the robot is unable to pull at the feet, only negative reaction forces can appear (expressed in $\{R\}$). Therefore at each time step the critical force for joint i will be the negative one, obtainable as the smallest of the two solutions:

$$f_{z,i}^* = \min(f_{z,i,1}^*, f_{z,i,2}^*) \tag{5.10}$$

For a leg ℓ with n joints, the critical normal force is given by the minimum over

---

[2]In these equations, the Jacobian component $J_{i,z}^T$ is also the sensitivity $S_{i,z}$, as explained at the beginning of this chapter.

all joints:

$$f_{z,\ell}^* = \min(f_{z,i}^*) \qquad\qquad i = 1 \dots n \qquad\qquad (5.11)$$

Finally, the tolerable variation $\Delta f_{z,\ell}^*$ can be calculated as the difference between the critical force and the expected one:

$$\Delta f_{z,\ell}^* = f_{z,\ell}^* - f_{z,\ell} \qquad\qquad (5.12)$$

A value of $\Delta f_z^* < 0$ would arise if a leg already contains a saturated joint.

5.3.2 Acceptable f_z Deviations for the Sway Gait

The critical force f_z^* and acceptable deviation Δf_z^* can now be obtained by means of Equations 5.8 – 5.12. Figure 5.4 shows the value of critical force f_z^* for each of the 6 legs of ATHLETE, during the first 6 steps of the sway gait [3]. The vertical force f_z that the leg would experience in the nominal case is also shown. A greater distance between the curves of f_z and f_z^* means that there is more room for disturbances. Legs 1 and 3 have the smallest margin when the 5th step of the cycle is executed. These legs are adjacent to leg 2 and experience the largest forces at that instant in time. They are also fairly stretched out, causing their critical joints to approach saturation.

---

[3]The special shorthand used in these plots to indicate the type of move that each data point represents was defined in Table 4.1.

Figure 5.4: **Critical forces for the sway gait. The plots show the value of vertical force that would result in saturation (f_z^*).**

From these curves it is possible to determine the critical leg at each time step of the gait. This will be the leg with smallest tolerable Δf_z^*. The critical values for the robot are summarized in Figure 5.5 for the first gait cycle. These are in the range of 430N to 2800N. The minimum tolerable increase in force (430N in this case) is the worst-case scenario during the execution of the optimized gait. Hence it can be used to define the maximum bump size that the terrain should have, as discussed in the following section.

Figure 5.5:   **Tolerable increase in normal force during sway gait execution.**

5.3.3   Terrain Characteristics – Bumps

The analysis presented in the previous section gives an idea of the sensitivity of torque ratio to forces. It is necessary to understand how this sensitivity translates into external factors such as the texture of the ground which is traversed by the robot. When the ground has features that are not present in the model used for planning, contact force variations are likely to occur and change the saturation behavior of the robot.

The mechanism by which these variations happen include: vertical footfall offsets caused by bumps, horizontal footfall offsets caused primarily by robot sag, and redirection of the net contact force as a result of contact slope. The first of these – bump size – is calculated here. Footfall offsets and contact slopes will be covered in §5.3.6 and §5.3.7.

Focusing now on bump sizes, when the actual ground contact point is higher or lower than expected and the robot is commanded in joint space, the vertical contact

force will deviate from the nominal value. A bump will cause a higher than expected force because the robot starts pushing the ground early. A depression will have the opposite effect.

The actual interaction with a real terrain is difficult to predict because various legs may be stepping on bumps or depressions simultaneously, depending on the local ground characteristics, starting pose and gait. Here a simplified analysis is made, assuming that only *one* leg is affected by a bump at any given time. Specifically, the critical leg at each gait event gives the upper bound of acceptable force deviations (Figure 5.5). To translate these force deviations into bump sizes, a linear force-displacement relation is assumed since the contacts have been modeled with linear springs. A bump height h_b will cause an equivalent *additional* deformation of the spring. Therefore, the critical bump height h_b^* is the one that introduces a force equal to the tolerable deviation Δf_z^*:

$$h_b^* = \frac{\Delta f_z^*}{k_z} \qquad (5.13)$$

Due to the force-displacement relation, h_b^* is inversely proportional to the spring stiffness k_z. This makes sense because a very rigid contact point will experience large force variations with small displacements. For ATHLETE k_z depends on the inflation pressure and terrain stiffness. Three spring constants are considered here, in the range of $3-5\frac{kgf}{mm}$ where the robot is normally operated. Figure 5.6 shows the scaling of the forces from Figure 5.5 by these three spring constants.

The tolerable bump ranges in size from 10-15mm. This is only realistic on very benign terrain like the one encountered on the Mars Yard at JPL. The experiments that will be presented in Chapter 7, conducted on such a terrain, were successful at preventing saturation. A lesson apparent from inspecting Figure 5.6 is that lower tire inflation pressures are more likely to succeed because larger bumps can be tolerated.

5.3.4 Tangential Force f_x

The analysis for both tangential components is similar. This section shows only the analysis in X, since it is the direction with the largest gain. Recalling that a

Figure 5.6:   **Tolerable bump size during sway gait execution.**

tangential force can only be applied with non-zero normal force, the equation that describes joint saturation is:

$$\left| J_{i,x}^T f_{x,i} + J_{i,z}^T f_{z,i} + \tau_{g,i} \right| = \left| \tau_{max,i} \right| \tag{5.14}$$

Assuming a known normal force given for example by the zero-interaction solution, this equation can be solved for $f_{x,i}$ to find its critical value. As with the normal force, two solutions exist depending on the direction of the force:

$$f_{x,i,1}^* \;=\; \frac{\tau_{max,i} - \tau_{g,i} - J_{i,z}^T f_{z,i}}{J_{i,x}^T} \tag{5.15}$$

$$f_{x,i,2}^* \;=\; \frac{-\tau_{max,i} - \tau_{g,i} - J_{i,z}^T f_{z,i}}{J_{i,x}^T} \tag{5.16}$$

Unlike before, neither of these solutions is invalidated by the physics of the problem

– tangential forces may be pointing either way. Therefore whichever direction has the smallest magnitude yields the critical force:

$$f^*_{x,i} = \begin{cases} f^*_{x,i,1} & \text{if } \left| f^*_{x,i,1} \right| < \left| f^*_{x,i,2} \right| \\ f^*_{x,i,2} & \text{otherwise} \end{cases} \tag{5.17}$$

Once again for a leg ℓ with n joints, the critical force is given by the minimum over all joints:

$$f^*_{x,\ell} = \min(f^*_{x,i}) \qquad\qquad i = 1 \ldots n \tag{5.18}$$

Assuming the robot is on horizontal ground, the tangential components of the zero-interaction force distribution are all equal to zero. Therefore the tolerable tangential force deviation is simply:

$$\Delta f^*_{x,\ell} = f^*_{x,\ell} \tag{5.19}$$

5.3.5 Acceptable f_x Deviations for the Sway Gait

Figure 5.7 shows the variation of Δf^*_x given f_z for all 6 legs of ATHLETE. The critical time step is again the execution of the 5th step in the gait, which is taken by leg 2. The adjacent legs (1 and 3) are able to tolerate the least amount of tangential force (275N) because they are already heavily loaded by the normal force and their configuration is fairly outstretched.

Figure 5.7: **Critical tangential forces for the sway gait. The plots show the value of tangential force that would result in saturation** (f_x^*).

For the complete robot the tolerable tangential force is determined by the minimum over all legs at each time step. The variation of this critical force is shown in Figure 5.8. The magnitude of the tangential critical force oscillates in the vicinity of 550N, but drops to the previously mentioned critical value when leg 2 is lifted. As expected, the valleys of this plot take place during leg lifts due to the increased loading of the legs that remain on the ground. The following subsections discuss how the critical force translates into acceptable contact point offsets and local terrain slopes.

Figure 5.8:   **Tolerable tangential force during sway gait execution.**

5.3.6   Terrain Characteristics – Footfall Offsets

The appearance of non-zero tangential forces in the nullspace can be caused in different ways. If the robot is commanded in joint space and the actual contact point with the ground is not exactly where anticipated, the contact springs will be loaded laterally as the robot settles into the requested joint angles.

The error in foot placement can in turn be a consequence of sag, in concert with joint space control. With this type of control the motion of the foot is specified by purely geometric means (either the final joint angles, or a sequence of joint configurations that move the foot in a straight line). When the robot sags, the pre-planned motion of the foot will intersect the ground at a location other than the intended one. Then as the robot pushes up tangential loading arises.

The actual magnitude of tangential force induced in this manner is not easy to predict, even assuming that sag can be modeled precisely. This is because the mechanics of the foot-soil interaction may provide a certain degree of leniency. That

is, if the top-most layer of the ground consists of loose soil then a certain amount of slippage will occur as the foot makes initial contact with the ground and begins pushing the body back up. Once the normal force builds up sufficiently to prevent violation of the friction cone no more slippage will occur and the contact point is fixed.

Figure 5.9 shows the lateral offset that can be tolerated by the ATHLETE robot during the sway gait. For the operational inflation pressures of ATHLETE this ranges between 7.5-10mm which is very small compared to the size of the robot. The successful experiments conducted with the robot at JPL demonstrate that this is achievable on benign terrain such as the one found in the Mars Yard, or wherever the deformable surface layer is likely to help.

Figure 5.9: **Tolerable footfall offset during sway gait execution.**

5.3.7 Terrain Characteristics – Contact Slope

Another situation that causes unanticipated tangential forces to appear is if the local slope at the contact point is different than the one assumed by the model used for planning. The local slope redirects the contact force away from the vertical, thus introducing a horizontal component that can contribute to saturation. Figure 5.10 shows the acceptable contact slope, assuming a nominal slope of 0°. For this particular gait the critical value is 7°.

Figure 5.10: **Tolerable contact slope during sway gait execution.**

5.4 Conclusion

The results presented in the previous two sub-sections demonstrate the important role of tangential forces in joint saturation. As found in §5.2 the largest gain for saturation is in the tangential directions. Subsequent analysis showed that this limits

the robot to walk on very benign terrain, with bumps $\leq 10 - 15mm$, footfall position offsets $\leq 7.5 - 10mm$ and local slope variations of $\leq 7°$.

The analysis presented in this chapter suggests that a great benefit can be gained from closed-loop control to achieve the desired values of contact forces accurately. The full benefit of the zero-interaction sway gait presented in Chapter 4 is only realizable if tangential forces are zero as modeled. Furthermore, if force control is available to zero out tangential forces, then any other desired value can also be achieved. Therefore the nullspace of tangential forces can be exploited to obtain larger saturation margins. The potential benefits of active force control and the nullspace are explored in greater detail in the following chapter.

Chapter 6

Gait Optimization With Use of Null Space

As explained in Chapter 2 there are multiple combinations of contact forces that satisfy the static balance constraints. These are collectively known as a nullspace, and can be exploited to reduce proximity to saturation further. This chapter describes a technique to determine the optimal combination of contact forces for a given robot pose, and provides simulation results for different scenarios that make use of this optimization. The chapter is organized as follows:

§**6.1** gives an overview of the solution approach.

§**6.2** illustrates the problem for the case of a single leg.

§**6.3** extends the analysis to optimize the force distribution of the complete robot.

§**6.4** presents simulation results for various scenarios that use force optimization.

§**6.5** summarizes the key insights and tradeoffs of the different approaches.

6.1   Outline of Approach

The process of using the nullspace of contact forces to prevent saturation can be divided into two parts:

1. Determining the optimal distribution of forces among the feet.

2. Applying these forces during gait execution using force control.

The rest of this chapter will focus on the first of these problems: determination of the best possible distribution of forces. With that in mind, the calculation of the best force distribution can be posed as an optimization problem whose cost function consists of the ∞-norm of torque ratios as used in Chapter 4, plus additional terms to reduce the **effort**[1]. Since the resulting cost function and constraints turn out to be linear, the optimization is a linear program. To gain an insight into the potential benefit of exploiting the nullspace, the case of a single leg will be examined first, followed by the application to the complete robot.

6.2 Optimal Forces for a Single Leg

Recall that the torque ratio for joint i is defined as follows:

$$\tau_{\%,i} = \left| \frac{\tau_i}{\tau_{max,i}} \right| \tag{6.1}$$

In this expression, τ_i refers to the *total* torque. If the robot has approximately massless legs, this is simply the torque needed to balance external forces. Otherwise, gravity torques must be added as well.

Note that the above expression is a piecewise-linear function of the contact forces, which are the design variables. For any given joint, piecewise linearity is a result of the absolute value, so the cost function is essentially "V"-shaped. Since the objective is to prevent joint saturation, the cost function to be *minimized* is:

$$J = \|\tau_{\%,1}, \ldots, \tau_{\%,n}\|_\infty \tag{6.2}$$

This is also a piecewise linear function, as will be shown in the next two subsections. As a reminder, Figure 2.5 shows the location and orientation of the $\{L_i\}$ reference frames.

---

[1]Here *effort* is defined as the sum of the magnitudes of contact forces – $\sum_{i=1..n_c} (|f_{x,i}| + |f_{y,i}| + |f_{z,i}|)$.

6.2.1 Force in the X Direction

As mentioned in the previous chapter, it is only possible to exert tangential forces if there is a non-zero normal force applied. For this example the robot is assumed to be in the standard pose shown in Figure 4.6, with all feet on the ground. Because this pose is symmetric, the optimal force components are the same for all legs and satisfy the balance constraints. Thus each leg is carrying $\frac{1}{6}$ of the weight (1470N). With this applied vertical force and no force applied in Y, the variation of $\|\vec{\tau}_\%\|_\infty$ as a function of f_x is shown in Figure 6.1.

Figure 6.1: **Maximum torque ratio vs** f_x**, given** $f_y = 0$N$, f_z = 1470$N**. The minimum is at** $f_x = 22.04$N**.**

It can be seen that $min(\|\vec{\tau}_\%\|_\infty)$ is achieved with a non-zero value of $f_x = 22.04$N. Since this is the required external force, it means that the leg would need to squeeze in the $-X$ direction. A non-zero force component is better than zero interaction because it redirects the *net* force so that the moment arm to the critical joint decreases, reducing the observed torque. If this redirection is taken to an extreme, such that the net force acts exactly through the axis of the critical joint, then a different joint will become the critical one. Therefore an ideal middle ground exists, which can be determined by optimization.

To clarify this, Table 6.1 summarizes some cases of interest. For negative values of

f_x the critical joint is the knee pitch (KP). At the optimal value of f_x the torque ratios of the KP and HP joints have been equalized. A further increase of f_x in the positive direction would make HP the new critical joint as KP approaches zero torque. The optimal tangential force is very small compared to f_z. The exact values depend on the specific configuration of the robot, but the result is consistent with the sensitivity analysis from Chapter 5, which demonstrated that large gains exist in the tangential direction.

f_z(N)	f_x(N)	$\tau_{\%,max}$	Critical Joint
	-30	0.426	KP
1470	0	0.391	KP
	* 22	0.365	KP/HP
	30	0.372	HP

Table 6.1: **Torque ratio variation vs** f_x

6.2.2 Force in the Y Direction

Assuming the same value of normal force as before, it is now possible to examine the effect of a lateral force applied in the Y direction. Figure 6.2 shows the $\|\vec{\tau}_{\%}\|_\infty$ as a function of f_y, with $f_x = f_x^* = 22.04$N, $f_z = 1470$N. The main point of interest is that the curve presents a flat area in the range of -600N $\leq f_y \leq 600$N. This means that in this range the variations of f_y have no effect on the objective function. The reason is that the critical joint (KP) is unaffected by f_y because the force is parallel to the joint's axis. In fact, only two joints are affected by f_y in this configuration – HY and KR. Thus in order for f_y to have an effect on the cost function, one of these two must become the critical joint, which does not happen until the force is very large.

The key insight is that, depending on the configuration of the leg, a component of tangential force may have no effect on cost. Strictly speaking any solution in the flat area has the same cost and would be a valid minimum. However, if a force component does not reduce the cost it is desirable to drive it to zero because this yields the same benefit with the *least effort*. This motivates the augmentation of the

Figure 6.2:   **Maximum torque ratio vs** f_y**, given** $f_x = 22.04\text{N}, f_z = 1470\text{N}$**. The curve is flat in the range of of** $-600\text{N} \leq f_y \leq 600\text{N}$**, meaning that the maximum torque ratio is not affected by** f_y **in this region.**

cost function with a weighted penalty and associated constraints designed to reduce effort, as explained in §6.3.1.

6.3   Optimal Forces for the Robot

The previous section discussed optimal forces for a single leg of the robot. In the specific example that was used these optimal forces would satisfy the balance constraints for the robot because the pose is symmetric. In the general case the legs may be in very different configurations, and if their optimal forces were calculated in isolation the resulting distribution would likely not result in static equilibrium. Therefore it is essential to obtain the optimal force distribution taking all feet into account.

The cost function was defined in Equation 6.2, where n is now the total number of joints under consideration. The problem is subject only to linear constraints, and can be posed as a linear program by means of the following equivalent problem:

Minimize:

$$J = t; \qquad \text{t: scalar} \tag{6.3}$$

Given the design vector:

$$\mathbf{X} = \{t, f_{x1}, f_{y1}, f_{z1}, \ldots, f_{xn}, f_{yn}, f_{zn}\} \tag{6.4}$$

The first set of constraints is given by the torque ratios, which are to be minimized:

$$t \leq 1 \tag{6.5}$$

$$\tau_{\%,1} \leq t$$
$$\vdots \tag{6.6}$$
$$\tau_{\%,n} \leq t$$

Note the similarities with the sway optimization, except that the design vector now consists of the contact forces at the feet. Assuming that the robot is in static equilibrium (or moves slowly enough to analyze its motion as quasi-static), the next set of constraints consists of the force and moment balance of the robot. These equations were previously derived in §2.4.2, and are summarized here for convenience.

$$\Gamma \vec{f} = \begin{bmatrix} -\vec{f}_g \\ \mathbf{0} \end{bmatrix} \tag{2.28}$$

Where Γ is the matrix resulting from stacking the Φ and C matrices:

$$\Gamma = \begin{bmatrix} I & \cdots & I \\ \hline C_1 & \cdots & C_{N_c} \end{bmatrix}_{6 \times 3N_c} \tag{2.29}$$

The final set of constraints is given by the necessary satisfaction of contact friction cones. These constraints actually serve a dual purpose: first, they guarantee that squeezing forces do not cause a foot to slip. Second, without these constraints it would be possible for the optimizer to converge to a force distribution where one or

more feet have $f_z = 0$, but $f_x \neq 0$ or $f_y \neq 0$. This is physically impossible because tangential forces can only be applied if the foot is planted on the ground, which implies $f_z \neq 0$. The situation is prevented here because it would violate the friction cone constraint.

These constraints are expressed in terms of contact friction cones, which represent the maximum valid tangential force f_t for a given value of normal force f_n (Figure 6.3(a)). Assuming that the tangential force is separated into its two components f_x and f_y, the friction cone constraint can be stated as:

$$\sqrt{f_x^2 + f_y^2} \leq |\mu_{s,i} f_z| \tag{6.7}$$

Equation 6.7 is nonlinear, so it is common practice to use a conservative linearization in the form of the square pyramid circumscribed by the exact friction cone (Figure 6.3(b)). This means that, for a given contact friction coefficient $\mu_{s,i}$, the linearized conservative pyramid is within the friction value (Figure 6.3(c)):

$$\mu_{c,i} = \frac{\mu_{s,i}}{\sqrt{2}} \tag{6.8}$$

(a) Friction cones   (b) Friction pyramid   (c) Conservative friction coefficient

Figure 6.3: **Friction cone constraints.**

It is now possible to write separate constraints for f_x and f_y using the conservative

friction coefficient. The basic relation to be satisfied is:

$$|f_{x,i}| \leq |\mu_{c,i}f_{z,i}| \tag{6.9}$$

$$|f_{y,i}| \leq |\mu_{c,i}f_{z,i}| \tag{6.10}$$

The vertical force in this case is known to be $f_z \leq 0$ in the {R} frame, because it is not possible for this particular robot to grasp the ground and pull. Therefore, the above can be broken down into four constraints per foot in contact to eliminate the absolute value operator:

$$f_{x,i} + \mu_{c,i}f_{z,i} \leq 0 \tag{6.11}$$

$$-f_{x,i} + \mu_{c,i}f_{z,i} \leq 0 \tag{6.12}$$

$$f_{y,i} + \mu_{c,i}f_{z,i} \leq 0 \tag{6.13}$$

$$-f_{y,i} + \mu_{c,i}f_{z,i} \leq 0 \tag{6.14}$$

Where

$\mu_{s,i}$: Static friction coefficient at contact point i.

$\mu_{c,i}$: Conservative friction coefficient at contact point i.

For rubber on concrete, μ_s is between 0.8-1.0. This value is used for the simulations in this chapter, since it is adequate for initial indoor experiments with ATHLETE.

6.3.1 Cost Function Augmentation

Although the optimization problem shown above is complete, it is possible to improve the solution further. As mentioned, it is desirable to reduce the net *effort* by driving to zero any forces not producing a benefit. This can be accomplished by adding a weighted penalty for non-zero tangential and normal forces. The first possibility to setup the effort reduction constraints would be:

$$J_a = t + \varepsilon_x \sum_i f_{x,i} + \varepsilon_y \sum_i f_{y,i} + \varepsilon_z \sum_i f_{z,i}$$

However, because f_x and f_y can be positive or negative, this would not always have the desired effect. The real objective is to penalize the sum of *absolute values* of forces. A mechanism similar to the one used for dealing with torque ratios can be applied. For this, auxiliary design variables $t_{x,i}$, $t_{y,i}$ and $t_{z,i}$ are added for each of the n_c feet in contact. The new cost function is the following:

$$J_a = t + \varepsilon_x \sum_i t_{x,i} + \varepsilon_y \sum_i t_{y,i} + \varepsilon_z \sum_i t_{z,i} \qquad (6.15)$$

With the following new design vector:

$$\mathbf{X} = \{t, f_{x,1}, f_{y,1}, f_{z,1}, \ldots, f_{x,n}, f_{y,n}, f_{z,n}, t_{x,1}, t_{y,1}, t_{z,1}, \ldots, t_{x,n}, t_{y,n}, t_{z,n}\} \qquad (6.16)$$

The basic effort reduction constraints to satisfy are:

$$|f_{x,i}| \leq t_{x,i}$$
$$|f_{y,i}| \leq t_{y,i}$$
$$|f_{z,i}| \leq t_{z,i}$$

These are broken down into six constraints per contact point to eliminate absolute values:

$$f_{x,i} \leq t_{x,i} \qquad (6.17)$$
$$-f_{x,i} \leq t_{x,i} \qquad (6.18)$$
$$f_{y,i} \leq t_{y,i} \qquad (6.19)$$
$$-f_{y,i} \leq t_{y,i} \qquad (6.20)$$
$$f_{z,i} \leq t_{z,i} \qquad (6.21)$$
$$-f_{z,i} \leq t_{z,i} \qquad (6.22)$$

The number of constraints has therefore increased by $6n_c$ for n_c feet in contact

with the ground. The additional constraints cause a small increase in computation time, but have the benefit of maximizing distance to saturation with the smallest possible magnitude of forces.

Finally, the ε factors should be selected such that the scaled summations are much smaller than t, in order to avoid affecting the optimal solution much.

6.3.2 Summary of Optimization Equations

In summary, the final set of equations defining the LP for optimal force distribution is as follows.

Minimize:

$$J_a = t + \varepsilon_x \sum_i t_{x,i} + \varepsilon_y \sum_i t_{y,i} + \varepsilon_z \sum_i t_{z,i}$$

Given the design vector:

$$\mathbf{X} = \{t, f_{x,1}, f_{y,1}, f_{z,1}, \ldots, f_{x,n}, f_{y,n}, f_{z,n}, t_{x,1}, t_{y,1}, t_{z,1}, \ldots, t_{x,n}, t_{y,n}, t_{z,n}\}$$

s.t.:

$$
\begin{aligned}
t &\leq 1 &&\text{Torque Constraints}\\
\tau_{\%,1} &\leq t\\
&\vdots\\
\tau_{\%,n} &\leq t
\end{aligned}
$$

$$\Gamma \vec{f} = \begin{bmatrix} -\vec{f_g} \\ \mathbf{0} \end{bmatrix} \qquad\qquad \text{Balance Constraints}$$

$$
\begin{aligned}
f_{x,i} + \mu_{c,i} f_{z,i} &\leq 0 \qquad &&\text{Friction Constraints} \\
-f_{x,i} + \mu_{c,i} f_{z,i} &\leq 0 \\
f_{y,i} + \mu_{c,i} f_{z,i} &\leq 0 \\
-f_{y,i} + \mu_{c,i} f_{z,i} &\leq 0 \\
&\;\;\vdots
\end{aligned}
$$

$$
\begin{aligned}
f_{x,i} &\leq t_{x,i} \qquad &&\text{Effort Reduction Constraints} \\
-f_{x,i} &\leq t_{x,i} \\
f_{y,i} &\leq t_{y,i} \\
-f_{y,i} &\leq t_{y,i} \\
f_{z,i} &\leq t_{z,i} \\
-f_{z,i} &\leq t_{z,i} \\
&\;\;\vdots
\end{aligned}
$$

6.3.3 LP Utilization

The optimal force distribution for a given robot pose can be found by means of the LP optimization described above. There is more than one way to use this optimization in the context of walking gaits. The options are:

- Apply the LP alone to each pose of the reference gait.

- Apply sway optimization and LP combined to each pose of the reference gait. In this case the LP provides the cost for the higher-level sway optimization.

Additionally, since the contact force distribution has tangential and normal nullspace components, these can be exploited one at a time or simultaneously. The following cases are simulated and discussed below:

§**6.4.1:** Reference gait + tangential nullspace $(f_{x,i}, f_{y,i})$.

§**6.4.2:** Reference gait + full nullspace $(f_{x,i}, f_{y,i}, f_{z,i})$.

§**6.4.3:** Sway + tangential nullspace $(f_{x,i}, f_{y,i})$.

§**6.4.4:** Sway + full nullspace $(f_{x,i}, f_{y,i}, f_{z,i})$.

6.4 Simulation Results

The starting conditions for these simulations are exactly the same that were used in §4.5 for sway compensation. The effect of applying only LP will be examined first, followed by the combination of LP and sway.

6.4.1 Tangential LP – No Sway

Figure 6.4 shows the variation of $\tau_{\%,max}$ for the sway gait and the reference gait with LP optimization of tangential forces only [2]. The maximum peak of the unoptimized reference gait was at 103%. LP optimization has reduced this peak to 63% (an overall reduction of 40%). For comparison, the maximum peak with sway only is 80%. The peaks occur during the execution of steps as expected. Since the LP has been applied at each gait time step, including the body shifts, the valleys have also been decreased considerably relative to both the reference and sway gaits.

The normal forces in this case are the zero-interaction reactions, and the tangential forces are calculated by the LP. Figure 6.5 shows the values of these forces for all the legs of the robot. Two plots are provided for each leg: the first shows the variation of all 3 force components for the initial 3 gait cycles of the reference gait with optimal contact forces. The second is a polar plot of the tangential forces for all the same time steps. All the forces are expressed in the $\{L_i\}$ frame.

The behavior of the f_z in this case is given by the zero-interaction solution since this component of the null space is not being actively selected. Each leg presents two f_z peaks per gait cycle. These happen when one of the adjacent legs is picked up

---

[2]The special shorthand used in these plots to indicate the type of move that each data point represents was defined in Table 4.1.

Figure 6.4: **Sway gait vs tangential LP**

(e.g. for leg 1, the peaks appear when legs 2 or 6 are lifted). That is, during the force redistribution that occurs after a foot is picked up, the adjacent legs present the highest forces, and the diametrically opposed leg experiences the lowest force.

The tangential forces remain below 1000N, approximately 2.5 times smaller than the normal force (in fact in most cases they are below 500N). The lower magnitude of tangential forces is expected for two reasons: first, since the robot is on horizontal ground there is no tangential component of the robot's weight. Second, the tangential directions see a larger gain (sensitivity) so smaller forces are required to impact the torque ratios. From the polar plots it can also be seen that in many cases the applied tangential force has only one component (i.e. only f_x or only f_y). These would correspond to situations where the leg's configuration is such that one of the components has no effect on the objective function of the LP. However this is not expected to happen all the time due to the changing geometry of the legs.

Figure 6.5: **Force variations for F_{xy} nullspace applied to the reference gait -$\{L_i\}$**

6.4.2   Full LP – No Sway

Figure 6.6 shows the variation of $\tau_{\%,max}$ for the case when the tangential and normal nullspaces are exploited. The plot for the tangential-only case is also shown for comparison. The maximum peak is now at 49% of saturation, a net reduction of 54% relative to the original 103%. As compared to using only the tangential nullspace, an additional benefit of 14% has been obtained. The difference between the results using tangential-only and full nullspaces is small compared to the 54% reduction from the unoptimized gait. This result is expected because as discussed in the previous chapter the sensitivity in the normal direction is less than in the tangential directions. Thus a larger benefit can be expected to derive from the use of tangential forces.

A behavior observable in this figure is that using the null space has a smoothing effect on the torque ratio curves: the difference between peaks is significantly decreased, and the valleys have very uniform values near 20-25%. Finally the amplitude of the oscillation between peaks and valleys is smaller.

Figure 6.6:   **Tangential LP vs full LP**

Figure 6.7 shows the values of normal and tangential forces for all 6 legs of the

robot. All three force components have now been found by the LP optimization. A very interesting behavior emerges when inspecting these plots: each leg now has two f_z valleys per gait cycle. One of these naturally occurs as before when the leg's turn in the step sequence arrives. The additional valley happens when the *diametrically opposed* leg takes a step, and in most cases corresponds to $f_z = 0$, which means that the leg is picked up twice per gait cycle (the exceptions are legs 1 and 2 which drop to values of 176N and 531N respectively). This means that for the purpose of preventing saturation it is sometimes better to pick up *two* legs simultaneously than just one. For this case the pick up sequence suggested by the optimization is: $6/3 \to 5 \to 4 \to 1/4 \to 2/5 \to 3/6$.

Note that since the gait planner has been setup to execute only one step at a time, this does not mean that e.g. legs 6 and 3 step simultaneously. Instead, it says that it is convenient to lift leg 3 while leg 6 takes a step, and then plant it back at its original location. The key insight, however, is that gaits that step with multiple legs simultaneously can be desirable for saturation reasons in addition to their known benefit of increasing locomotion speed. This means that different *reference* gaits ought to be considered if the global optimum is desired for the specific application. In other words an additional optimization layer to design the reference gait would need to be added, the cost of which would be provided by the LP or the LP+sway combination.

The lifting sequence found by the optimizer in this case is very close to a $6/3 \to 5/2 \to 4/1$ gait, which executes steps with two diametrically opposed legs simultaneously. It is reasonable to assume that such a gait would constitute a better reference gait than the current reverse wave gait from the standpoint of saturation. Investigation of whether this is the case is suggested as future work.

Finally, regarding the direction of the net tangential force, examination of the polar plots shows a larger spread as compared to the case of $f_{x,y}$ null space, where many forces were directed along the X or Y axis. However no significant difference can be observed in their magnitude, which also remains below 1000N in this case.

Figure 6.7: **Force variations for F_{xyz} null space applied to the reference gait.**

6.4.3   Tangential LP With Sway

The torque ratio variation resulting from a combination of sway and tangential nullspace forces is shown in Figure 6.8. The highest peak is at 48% of saturation. This benefit is almost identical to the one obtained with full nullspace LP applied directly to the reference gait. A likely explanation of the similarity is the fact that both methods profit from all 3 force components (by different mechanisms) – in the full-LP case the normal forces are modified through the null space, while in the combined sway + tangential LP this is achieved through the motion of the chassis.

The sway + $f_{x,y}$ nullspace case presents a similar equalization of peaks throughout the gait as the nullspace without sway. It is also interesting to note that, while observation of the peaks of the two curves in Figure 6.8 does not clearly suggest either one being preferable over the other, the valleys are lower for the full nullspace without sway in almost every case. Although this difference is less than 5% it may be worth considering when deciding between the two techniques.

Figure 6.8:   **Full LP vs Sway+Tangential LP**

The resulting motion of the chassis is shown in Figure 6.9 below. Only the first 3 gait cycles are shown here, since the pattern is regular after the 3$^{\text{rd}}$ cycle. As compared to the gait with only sway described in Chapter 4 it can be observed that

the side-to-side amplitude of sway is smaller in the LP case once the robot settles into a regular gait.

Figure 6.9:   **Body path during the initial three cycles of the combined sway+tangential LP gait.**

Figure 6.10 shows the variation of forces for all 6 legs of the robot. Similarly to the case of tangential LP without sway, the net tangential forces are directed along the X or Y direction exclusively a large percentage of the time. The magnitudes of tangential forces stay within 750N, with only a few cases between 750-1000N. It is interesting to note that the peak value of tangential forces coincides in time with the peak value of torque ratio. With the current strategy this corresponds to the 2nd step of the sequence at steady state (i.e. leg 5).

The normal force for each leg presents 2 major peaks per gait cycle as with the previous cases that do not use the vertical null space. These peaks occur when the adjacent legs are picked up.

Figure 6.10: **Force variations for combined sway and F_{xy} null space.**

6.4.4 Full LP With Sway

The largest reduction in the maximum torque ratio can be accomplished by combining body sway and the nullspace in all 3 directions. This is shown in Figure 6.11 below. The maximum peak is at 44% of saturation, a net reduction of 59% from the reference gait value. As was the case with the LP-only cases, the difference between using tangential forces only or the complete nullspace is not very significant (only 4%) in this case). However, as expected, the curve with full nullspace always remains below the one for tangential nullspace. The previously mentioned smoothing effect is also present, and the maximum variation between the lowest and the highest peak is only 5% at steady state.

Figure 6.11: **Sway+Tangential LP vs Sway+Full LP**

The resulting motion of the chassis is shown in Figure 6.12 below. Other than the decrease in sway amplitude it is also worth mentioning the contralateral oscillation, with the body moving to the right of the center line when the legs on the left hand side are stepping, and vice versa. The same behavior is observed in every case where sway is used.

Figure 6.12: **Body path during the initial three cycles of the combined sway+full LP gait.**

The variation of contact forces is shown in Figures 6.13. A behavior similar to the case without sway is observed: the optimization reveals that it is often best to pick up two radially opposed legs simultaneously. The pick up sequence that emerges in this case is: $6 \rightarrow 5 \rightarrow 4/1 \rightarrow 1/4 \rightarrow 2/5 \rightarrow 3/6$. This is again very similar to the $6/3 \rightarrow 5/2 \rightarrow 4/1$ gait, suggesting that the latter might constitute a better reference gait to prevent saturation.

Regarding the direction of the net tangential force, a significant scatter is present for some legs (e.g. legs 2 and 6), while others show some clustering on the f_x, f_y axis. Leg 3 even shows a number of forces directed roughly along the 150° direction. In all, the behavior is different for each of the 6 legs. Except in a case where all legs are in the same configuration, there is no reason to expect symmetric forces between, say, radially opposed pairs. Since each leg will generally be in a different configuration, the balance equations might be satisfied with the force of one leg counteracted by two opposite legs, for example.

Figure 6.13:   **Force variations for combined sway and F_{xyz} null space.**

6.4.5 Friction Requirements

The use of the null space in the tangential direction mandates careful attention to the friction conditions at the contact points. For the simulations presented in the previous sections the friction coefficient was chosen to be $\mu_s = 1.0$, which corresponds to rubber on concrete. The *actual* minimum friction coefficient required varies throughout the gait, and its value at each time step can be obtained from Equation 6.7 given the values of f_x, f_y, f_z returned by the optimizer.

Tangential LP – No Sway

Figure 6.14 shows the variation of required friction coefficient for the case of tangential null space without sway (§6.4.1). In all cases the value of μ_s remains below 0.6, with some legs requiring only about 0.2. The gaps in the plots correspond to the instances when the leg of interest is unloaded ($f_z = 0$), and hence no tangential force is applied.

Full LP – No Sway

The friction behavior for the full null space without sway (§6.4.2) is shown in Figure 6.15. The required friction coefficient in this case is higher than for the tangential-only LP, and for leg 2 reaches a value of 0.95. This means that the net force for that leg will be very close to the edge of the friction cone at that instant in time.

Referring to the plot of force variations for this case, shown in Figure 6.7, the peaks are verified to correspond to cases where the leg is assigned a light vertical load by the optimizer (f_z is small). Although the selected forces satisfy the friction constraint, it is possible that they might be risky if the friction coefficient is not known precisely. In such cases, a more conservative value of μ_s could be selected for the optimization. Another possibility is to make use of the full nullspace only if the specific move is critical from the standpoint of saturation, requiring as much torque reduction as possible.

Tangential LP With Sway

Figure 6.16 shows the minimum required friction coefficient for the tangential null space combined with sway (§6.4.3). The behavior is very similar to the case without sway, with values that remain below 0.6.

Full LP With Sway

Finally, Figure 6.17 shows the variation for the full nullspace plus sway (§6.4.4). The value of μ_s is higher than in the case of tangential-only nullspace with sway, but remains below 0.65.

Figure 6.14: **Minimum μ_s required to prevent slippage when using F_{xy} nullspace.**

Figure 6.15: Minimum μ_s required to prevent slippage when using F_{xyz} nullspace.

Figure 6.16: **Minimum μ_s required for combined sway and F_{xy} nullspace.**

Figure 6.17: **Minimum μ_s required for combined sway and F_{xyz} nullspace.**

6.4.6 Comparison of Approaches

The torque ratio plots shown in the previous sections provide a complete picture of the behavior throughout the gait. From the perspective of preventing saturation the most interesting quantity is the maximum peak because it is the closest that the robot will come to its actuation limits for a given gait. Figure 6.18 summarizes the maximum peaks for the reference gait and all 5 of the optimization approaches previously discussed in this dissertation. These are shown in order of the benefit they provide.

Figure 6.18: **Comparison of peak torque ratios for the gait optimization approaches presented in this dissertation.**

As the figure shows, the 4 approaches that actively use the null space of contact forces outperform the reference and pure sway gaits. The best performance is obtained from combining sway with full use of the null space. This is not surprising since adding more degrees of freedom that modify the torque ratios should result in a higher benefit. A discussion of these results is included in the following section.

6.5   Discussion

It is clear from the analysis presented in this chapter that active use of the null space offers very important benefits. In terms of saturation, the actuation margin is improved by 40-54% when using *only* the null space directly on the reference gait.

Ultimately the selection of the best approach for a specific application depends on a number of factors. For example if the robot must traverse tight spaces, sway may not be acceptable. Pure use of the null space will therefore be the best choice in this case, or wherever sway is not desired. It is also ideal for robots with severely limited actuation, because it largely increases the margin to saturation.

Another consideration is that any approach that makes use of non-zero tangential forces is dependent on a reasonable knowledge of the contact friction coefficient. Otherwise there is a risk of causing a foot to slip as the tangential nullspace is excited. For this work the assumption has been made that this coefficient is the same for all the feet throughout the gait. On very heterogeneous terrain such an assumption may not be valid. In that case a conservative estimate of friction properties can be used, although this may limit the achievable reduction in torque ratios. The safest approach in this case would be the zero-interaction gait.

Chapter 7

Experimental Results

This chapter describes the experiments carried out on NASA's ATHLETE robot to validate the sway optimization technique developed in this dissertation. The chapter is organized as follows:

§**7.1** describes the test site and robot.

§**7.2** outlines the estimation of torques from available robot telemetry.

§**7.3** presents the experimental results for the reference gait.

§**7.4** presents the experimental results for the sway gait.

§**7.5** summarizes some lessons learned during the experiments.

7.1   Description of Experiments

7.1.1   Test Location

The sway optimization technique developed in Chapter 4 was validated on the ATHLETE lunar hexapod, described in Chapter 3. The experiments were conducted at the Jet Propulsion Laboratory's Mars Yard facility in Pasadena, California. An aerial view of this facility is shown in Figure 7.1. The Mars Yard is approximately 50x30m and allows testing on a variety of terrains akin to those encountered on the moon and Mars. The surface is made of compacted brick dust, and is generally fairly rigid with

a thin surface layer of loose dirt.[1]

The locations where the experiments were conducted are labeled Ⓐ and Ⓑ. These locations were found to be sufficiently planar and horizontal, with a maximum slope of 3°. The north portion of the Mars Yard consists of sloping terrain varying from 0° to about 30°. In contrast, the south part contains boulder fields with a mix of real and artificial rocks, which can be easily moved around to match known statistical distributions of boulder size and location on the moon and Mars.

Figure 7.1: **Aerial view of the Mars Yard at JPL (North is up). Experiments for the reference gait were conducted at location Ⓐ in May 2009. The sway-optimized gait presented in Chapter 4 was tested at location Ⓑ in June/July 2009.**

The zero-interaction experiments took place during the months of May, June and July, 2009. The reference gait was tested at location Ⓐ on May 14, 2009. The zero-interaction sway gait was tested at location Ⓑ on June 29, 2009. The experiments were carried out at different locations because of the limited time that the robot was available. The exact initial conditions and observed results for each experiment are described in the following sections.

---

[1]The friction coefficient for rubber on this surface is not readily available, but was not needed for the zero-interaction experiments.

7.1.2   Robot Used

Of the two working prototypes developed by JPL, the same robot (SDM-B[2]) was used for all of the tests described in this chapter. The robot is equipped with pneumatic tires, whose inflation pressures were measured to be in the range of $6 - 10$psi. A detailed description of ATHLETE was provided in Chapter 2.

No experiments with the LP-optimized gait were possible due to time constraints. Experiments of this kind would also greatly benefit from closed-loop force control capabilities not available on either of the two ATHLETE prototypes.

7.2   Joint Torque Estimation

The joint torque values used to evaluate the performance of the sway optimization were estimated by incorporating sensor measurements of joint angles and the robot attitude quaternion as will be described below.

The robot is equipped with an indirect torque sensing system which is described in [Collins 07]. A detailed analysis of the telemetry from this system was carried out, and the torque measurements were observed to have significant biases, rendering them unusable for the purpose of these tests.

The best available estimate of the joint torques is therefore obtained as follows. The torques due to contact forces are calculated from the measured Jacobian and the estimated contact force:

$$\hat{\vec{\tau}}_{ext} = J_m^T \hat{\vec{F}} \tag{7.1}$$

The Jacobian incorporates the joint angles measured by the robot's encoders. The force estimate is calculated as described in Chapter 2, using the spring-mass model. Thus this estimate incorporates the measured joint angles, and the robot pose quaternion indicated by the onboard IMU. The estimated total torques consist of the external plus gravity components, per Equation 2.19. The latter are calculated using the measured joint angles, robot pose and estimated CM locations of the leg's links.

---

[2]SDM-B = Software Development Model B

7.3 Reference Gait

The reference gait for these experiments consists of a discontinuous reverse-wave sequence, with one body shift after every step. The robot was driven to the starting location Ⓐ near the west edge of the Mars Yard and placed in the standard driving pose. The chassis was then commanded to a level orientation (zero roll and pitch) to correct for the local slope, and a height of 2.1m in order to prevent any accidental ground contact. Figure 7.2 shows the robot executing the reference gait.

Figure 7.2: **ATHLETE executing the reference gait. The camera is at location Ⓐ facing southeast, and the robot is walking toward the right of the image, due west.**

The torque estimates for the first 8 steps of the reference gait are shown in Figure 7.3. The maximum torque ratio requested from the robot reaches 104.6% during the execution of the 5th step of the gait, causing saturation of a joint. During this experiment the robot was able to continue walking because it is equipped with mechanical brakes at the joints that are able to support the extra load.

The *modus operandi* in this experiment was to close the brakes before each step in the 5 legs that remain on the ground. In a different scenario, however, these legs might need to correct actively for the sag of the chassis to keep it level, and the motion would be interrupted by a saturated joint. This situation was encountered

during tests with ATHLETE, as shown in Figure 7.4. Here the rear leg has started to step, and one of the adjacent legs has saturated in the process of leveling the chassis.

Figure 7.3: **Torque ratio variation for the reference gait experiment on ATHLETE.**

Figure 7.4: **ATHLETE executing a sag-compensating reference gait. One of the legs has reached saturation causing the motion to stop.**

7.4 Sway Gait

The reference gait from the previous section was optimized by means of sway and executed on the robot. A photograph of ATHLETE executing this sway gait is shown in Figure 7.5.

Figure 7.5: **ATHLETE executing a sway gait**

The variation of maximum torque ratio for the first 8 steps of the sway gait is shown in Figure 7.6, along with the reference torque ratios for comparison. Except in the case of the 8th step, the peaks were reduced by 5-25%. Of special interest is the 5th step, which was improved from 104.6% to 79.2%, a net reduction of 25.4% which prevents saturation with sufficient margin. The previously mentioned 8th step had an observed increase of 4% after optimization. This was likely caused by slight differences in ground texture at sites Ⓐ and Ⓑ.

The ATHLETE robot exhibits significant compliance coming primarily from the compression of the tires. This causes the body to experience changes in height and pose as the forces are redistributed during walking. These height and pose variations may not be acceptable for some applications, for example when a manned habitat is carried by the robot. They can also cause the feet to impact obstacles during step execution if this sag is not estimated with enough precision.

Figure 7.6: **Torque ratio variation for the sway gait experiment on ATHLETE.**

To prevent problems caused by sag the robot can use the legs that remain in ground contact to push up and maintain the body leveled. This mode of walking is more demanding on the joints because the load cannot be absorbed by the brakes, since they need to be open in order to actuate the motors. For this reason the sag-compensating gait is an ideal candidate for optimization.

An experiment was conducted to test this scenario. The robot was driven to location Ⓑ on the Mars Yard and commanded to execute a sag-compensating gait with sway. In contrast to the situation depicted in Figure 7.4, the requested motion was completed successfully without reaching saturation, providing visual confirmation of the predicted benefit of sway optimization. A snapshot of ATHLETE executing this gait is shown in Figure 7.7.

Figure 7.7: **ATHLETE successfully executing a sag-compensating sway gait**

7.5 Lessons Learned

7.5.1 Acceptable Terrain

The main drawback of not having force control is that terrain variations can cause the robot to reach saturation, as discussed in Chapter 5. The experiments with ATHLETE showed that it is possible to achieve successful walking without saturation on benign terrain without active force control. Figure 7.8 exemplifies the kind of terrain that can be accessed this way. Note that it would be acceptable for the terrain to contain boulders, as long as the ground around them is sufficiently planar. Similar terrain exists on lunar and Martian plains, but given the wide variety of conditions likely to be encountered by the robot it would be important for planetary robots to be equipped with force control capabilities.

Figure 7.8: **An example of acceptable terrain for execution of a sway gait without force control.**

7.5.2 Spring Constants and Compliance

The spring-mass model developed for simultaneous estimation of sag and contact forces proved sufficient for the experiments with ATHLETE [Wheeler 10]. In general the model was able to predict the robot's compliance to within a couple of centimeters when measured on a concrete surface. Experiments on the Mars Yard yielded mixed results on this regard – the compliance of the ground compounds with tire deformation to yield a softer net spring. The resulting spring constant proved difficult to calibrate precisely in the model, because it appeared to vary with robot pose and location, probably as a result of soil density variations. A sensor-based system to estimate the spring constant continuously during walking would be useful for future experiments. Such a system may also provide information needed to estimate the friction coefficient of the ground when walking on a slope.

Another factor contributing to spring constant variations is the deformation of the robot's structure itself. The body of ATHLETE can deform significantly under load, as can the different components of the legs. In a sense the model used here lumps all compliances into a single spring constant. A more accurate estimate may be obtained

by finite element analysis of the body components, which can yield load-deflection curves for different loading conditions, which can then be incorporated into an online compliance estimator. This would be a good avenue for future research.

7.5.3 Force Control

The experiments and simulations presented in this thesis strongly indicate the need for force feedback capabilities on walking robots. While the joint-space approach tested on ATHLETE successfully prevented saturation, force control is a requirement to guarantee that the full benefit of the optimization techniques is achieved. Furthermore, a robot exploring a planetary surface will only rarely encounter benign terrain like the one described in §7.5.1, and as a result the risk for joint saturation would continue to exist if the contact forces cannot be adjusted precisely while negotiating more irregular terrain.

7.5.4 Other

In addition to the experiments described in this chapter, walking was also tested on slopes of 7° and 14°, as shown in Figure 7.9. These experiments were intended to test only the reference gait, so no optimization was applied. Even at these relatively shallow inclinations the robot was observed to be very constrained kinematically. In particular, since it was desired to keep the chassis horizontal the legs on the downhill side reached maximum extension very quickly, while the ones on the uphill side had little space to maneuver between the chassis and the ground.

While theoretically walking robots are capable of climbing very steep terrain, this carries an underlying assumption that the orientation of the body is flexible. Indeed keeping the body parallel to the local ground largely alleviates this issue, but it may not always be possible depending on the payload. Geological studies of the moon and Mars suggest that the *maximum* slopes on hills and impact craters can reach up to 35°, depending on the angle of repose of the soil and whether a rocky substrate exists (see e.g. [Heiken 91]). Such slopes would not be traversable with ATHLETE in a level chassis configuration, but may perhaps be accessible if the body pose is relaxed.

(a) 7° slope

(b) 14° slope

Figure 7.9: **ATHLETE walking on slopes of 7° and 14°. The latter starts to place severe kinematic constraints on the motion of the robot.**

During the 14° slope experiment the robot was also observed to slide downhill a short distance ($<$ 5cm) on occasion. This points to the importance of taking into account the contact friction coefficients when designing gaits for steeper terrain. This can be done through friction cone constraints like the ones used in Chapter 6.

Chapter 8

Conclusions and Future Work

The work presented in this dissertation has demonstrated two motion optimization techniques to prevent joint saturation in walking robots. This chapter reviews the main contributions of this work, summarizes the lessons learned, and suggests areas for future research.

8.1   Review of Contributions

- A zero-interaction gait optimization technique was developed that makes use of body sway to prevent joint saturation. The margin to saturation was increased by 20% for the ATHLETE robot. Field trials on the robot were successful, enabling uninterrupted walking even while executing demanding sag mitigation maneuvers.

- A technique to take advantage of the null space of ground contact forces to improve saturation margins further was developed and tested in simulation. The optimal force distribution is found by solving a constrained LP, with observed improvements of up to 60%.

- A method for simultaneous calculation of contact forces and robot sag was developed. The new technique is valid for homogeneous or heterogeneous contact

stiffnesses, and takes into account force redistribution during the lifting and planting of feet.

The applicability of the optimization techniques extends beyond the realm of walking gaits: since they operate on individual poses, they can be applied to other motions executed by limbed robots, including climbing and manipulation. For example, a limbed robot equipped with a drilling tool would experience torque variations while using this tool, and an optimal drilling pose can be obtained by using the techniques presented in this dissertation.

8.2 Lessons Learned

8.2.1 Benefit of Null Space

The use of the null space of forces was observed to produce significant reductions in torque ratios, contrary to intuition. The reduction is achieved because the net contact force is redirected relative to the critical joint of each leg.

8.2.2 Benefit of Simultaneous Steps

The analysis of gaits that use the vertical null space revealed that in some configurations it is better to pick up two legs at the same time. This is a result of a more even distribution of forces among the four legs that remain in contact with the ground.

8.2.3 Relation to Legged Robot Design

Robot design is an iterative process for which a number of tradeoffs must be carefully considered. The work presented here showed that the analyzed gait could be executed with only 40% of the original torques. This information is useful for the sizing of electric motors during the robot design stage. The analysis can be repeated for a number of possible gaits in order to determine suitable motors that work well in the situations that the robot is expected to encounter.

8.3 Future Work

8.3.1 Optimization Extensions

The focus of this research has been on preventing saturation with the largest margin possible at *every step*. Analysis of the various torque ratio plots from Chapter 6 shows that not all moves along the gait come very close to saturation. For these moves it might be desirable to aim for minimum power or maximum stability instead. These competing objectives may be incorporated into the cost function with adequate weights. The effect on the shape of the cost function and the possibility of local minima would need to be evaluated in that case.

Another possible extension is to seek the best of all possible reference gaits by searching over different step sequences and relaxing the assumption that only one foot steps at a time and that these steps are always separated by a body shift.

8.3.2 Combined Walking and Rolling

The possibility of *rollking* as a mode of locomotion for wheel-in-leg robots was mentioned in Chapter 1. Little work has been done on motion planning, optimization and control to enable rollking. The motion in this case would also be subject to torque, power and stability constraints, so extending the techniques presented in this dissertation to accommodate rollking would be a good avenue of research.

8.3.3 Dynamic Robots

A large fraction of the research on multi-legged robot locomotion is currently focused on enabling higher speeds. Joint saturation is particularly dangerous for running robots because it is likely to cause instability. Techniques similar to the ones presented in this work would be useful for running robots.

8.3.4 Footfall Planning

The techniques developed in this thesis assume the existence of a pre-planned reference gait, whose footfall locations must be preserved by the optimization. The method used to design the reference gait is of no consequence to these optimization techniques. However, the location of the reference footfalls does affect joint torques because it determines to a certain extent the leg geometries and force distributions throughout the motion.

Therefore, a benefit can also be obtained by focusing on a careful selection of the initial footfalls (i.e. *footfall planning*), based on a metric of their impact on saturation. Footfall planning is an active area of research for legged robots (e.g.[Hauser 08b]), but the use of proximity to saturation as the main selection criterion has not been explored so far. This would be a promising direction for future research.

8.4 Conclusion

The motion optimization techniques developed in this dissertation have enabled a robot with severely limited actuators to walk successfully under demanding conditions. The development of future robots and their gaits can build upon the tools presented here to achieve safer walking and more efficient designs.

Appendix A

Single Step Motion Planning

The execution of each step for a legged robot requires solution of a motion planning problem, particularly in environments with obstacles. This appendix compares four possible motion planning approaches based on simulation and experimental work on the ATHLETE robot.

§**A.1** provides an overview of the Appendix.

§**A.2** describes the four motion planning algorithms that were compared.

§**A.3** explains the experimental setup for the motion planning comparisons.

§**A.4** shows the comparison results.

§**A.5** summarizes the findings of the experimental study.

A.1 Overview

This appendix describes and compares four different algorithms for generating a single-step sequence of commands for legged robots. The material included here is based on joint work with Dr. Tristan Smith of the Planning and Scheduling group at NASA Ames Research Center. An extended version of this material was presented at the 2009 SMC-IT Conference in Pasadena, California [Smith 09].

Three of the four algorithms search *configuration space ("C-Space")*. Each dimension in configuration space represents the range of angles for one of ATHLETE's joints. A path through configuration space represents a sequence of moves (changes in joint angles) the robot can make to get from one configuration to another.

The first algorithm only tries the straight line between the start and end config-urations, the second is a standard randomized motion planning algorithm, and the third is an A* search through a discretization of configuration space. The fourth and final approach is A* search in *task space*, the three-dimensional Euclidean space in which the robot operates.

A.2 Algorithms

A.2.1 Preliminaries

The goal for each of the algorithms is to produce a sequence of commands to move an ATHLETE foot from one location to another. It is assumed that the position and orientation of the chassis remain fixed, and therefore the configuration of the other five legs can be ignored.[1] This simplification means the planning problem is only concerned with the six-dimensional configuration space representing the joint angles shown in Figure A.1.

The location of the foot can be represented as either:

- A six-tuple in configuration space, c_i, or
- A three-tuple in task space, xyz_i.

In addition, the functions $TO\text{-}TSPACE(c_i, leg_j)$ and $TO\text{-}CSPACE(xyz_i, leg_j)$, are available to convert between the two spaces via the forward or inverse kinematics of the leg. While one location for the foot in task space, xyz_i, could correspond to many different configurations, the implementation of $TO\text{-}CSPACE(xyz_i, leg_j)$ used here is one-to-one and always computes the same c_i for a given xyz_i.

Finally, a function $COLLISION\text{-}FREE(c_i, c_{i+1})$ is available that determines whether the straight line in configuration space between c_i and c_{i+1} is free of collisions; the leg must not collide with itself, other parts of the robot, or the terrain.

As problem input, the following is assumed:

---

[1]Although it might be necessary in tight space to adjust other legs or the chassis in order to reach a goal, such motions are considered part of multi-step walking and are not included here.

Figure A.1: **The joints on an ATHLETE leg.**

- Terrain data. For the experiments presented here, it is auto-generated; in reality, it would be acquired with ATHLETE's 15 on-board cameras.

- The leg, leg_i, to move.

- Current position. This includes the location and orientation of the chassis, and all six joint-angles for each leg. It is assumed that this represents a valid and stable position on the terrain, and that ATHLETE will remain stable when leg_i is lifted.

- A goal position in task space, xyz_{goal}, for leg_i.

Given this data, the start and goal configurations c_{start} and c_{goal}, are computed. c_{start} is obtained by lifting leg_i 10cm above its current position, and c_{goal} is a configuration 10cm above xyz_{goal}. These 10cm buffers are included because a weight-bearing leg must be raised by about this much before it is truly free of the ground, due to the way the chassis sags as the leg is lifted.

The goal for each algorithm is to produce a path $(c_{start}, ..., c_{goal})$ through configuration space such that each edge (c_i, c_{i+1}) is collision free. The solution path can then be converted to a sequence of low-level commands, which move leg_i to c_{goal}.

A.2.2   Straight Line Approach

The baseline algorithm, $SMPL$,[2] simply calls *COLLISION-FREE*(c_{start}, c_{goal}). If the straight line between c_{start} and c_{goal} has no collisions, it is returned as the solution path. If not, the algorithm fails.

A.2.3   SBL

The second approach is a Single-query Bi-directional planner with Lazy collision checking (SBL), and is outlined in Algorithm 2.

Algorithm 2
---
function SBL(c_{start}, c_{goal})

 1: $T1.root = c_{start}$
 2: $T2.root = c_{goal}$
 3: **while** not timed out **do**
 4:   Execute EXPAND-TREE
 5:   $\tau \leftarrow$ CONNECT-TREES
 6:   **if** τ is not empty **then**
 7:      Return *success*
 8:   **end if**
 9: **end while**
10: Return *failure*

SBL is a sampling-based motion planning technique. The search for feasible paths is conducted by sampling configurations between the start and goal, and verifying if (a) they are feasible, and (b) they can be connected without collisions.

The algorithm proceeds by growing two C-Space trees T_1 and T_2 rooted at c_{start} and c_{goal} toward each other. On every iteration one of the trees is selected at random with probability 0.5, and a new milestone m_{new} is added to it (*EXPAND-TREE* step). The planner then checks if a connection can be established between the trees (*CONNECT-TREES* step), and if so it generates a candidate path τ from c_{start} to c_{goal}. This path includes a segment called a bridge, connecting m_{new} to m, the nearest

---
[2]The abbreviation $SMPL$ is used as shorthand for "Simple".

milestone in the opposite tree. If τ is found to be collision-free, success is returned. Otherwise iterations continue until time-out, at which point failure is returned. This means that either no path exists, or SBL was unable to find one.

The *EXPAND-TREE* step proceeds as follows: from the selected tree T, an existing milestone is selected at random with probability $\pi(m)$, which is inversely proportional to the density of milestones of T near m. Then, a collision-free configuration is randomly selected within an adaptively-chosen distance of m, and is added to T as the new milestone m_{new}. This selection strategy distributes the exploration around areas reachable from the root configurations, and at the same time prevents oversampling. It should be noted that only m_{new} is checked for collisions at this stage, not the segment connecting it to m. Segment checks are postponed until they are absolutely necessary in the *CONNECT-TREES* step. This lazy approach has the effect of reducing the total number of expensive collision checks.

The *CONNECT-TREES* step of SBL is executed when the distance between m_{new} and m is smaller than or equal to the distance threshold. At this point the candidate path τ is checked for collisions to a resolution ε by a *TEST-PATH* routine, and τ is returned as the motion plan if it is collision-free; otherwise, iterations continue.

Further details on SBL can be found in the original paper by Sanchez and Latombe [Sanchez 01].

A.2.4   A* Search in Configuration Space

The third approach, CFG uses A* search [Russell 09] through the six-dimensional configuration space for leg_i. Each dimension is discretized into increments of r radians, and a search is conducted over the resulting grid.

Algorithm 3 outlines the specifics of the approach.[3] A queue of nodes is initialized with a node representing the start configuration. Each node n in *queue* stores:

- $n.g$,the distance travelled to get there,
- $n.h$, an optimistic estimate of the distance to the goal, and

---

[3]A slightly modified version of the C++ implementation written by Justin Heyes-Jones: http://www.geocities.com/jheyesjones/astar.html was used

---

Algorithm 3

---

function ASTAR(*start*, *goal*)

1: $start.g = 0$
2: $start.h = \text{DISTANCE}(start, goal)$
3: $start.parent = \text{NULL}$
4: $queue.\text{ADD}(start)$
5: **while** $n = \text{GET-BEST-NODE}(queue)$ and n not NULL and not timed out **do**
6:    **if** n is goal **then**
7:       Return *success*
8:    **end if**
9:    $succs = \text{GET-SUCCESSORS}(n)$
10:    **if** n near goal **then**
11:       $succs.\text{ADD}(goal)$
12:    **end if**
13:    **for all** s in $succs$ **do**
14:       $s.g = n.g + \text{DISTANCE}(n, s)$
15:       $s.h = \text{DISTANCE}(s, goal)$
16:       $s.parent = n$
17:       $queue.\text{ADD}(s)$
18:    **end for**
19: **end while**
20: Return *failure*

- *n.parent*, the node from which n was generated.

At each step, the function *GET-BEST-NODE* returns the node n in *queue* for which $n.g + n.h$ is lowest.[4] Then, n is expanded; *GET-SUCCESSORS* returns the twelve grid nodes (obtained by moving left or right along each of the six dimensions) adjacent to n, which are then added to *queue* with appropriate g and h values.[5]

When *success* is returned, the solution can easily be extracted because each node stores its *parent*.

A.2.5 A* Search in Task Space

Finally, the fourth approach, TSK, uses A* search over a discretized grid in three-dimensional task space. Each point xyz_i represents a position of the foot (which then has a corresponding point, *TO-CSPACE*(xyz_i), in configuration space). Algorithm 3 is still used but *GET-SUCCESSORS*(n) returns the six grid nodes in task space adjacent to n, and *DISTANCE*(n_i, n_j) computes three-dimensional Euclidean distance rather than distance in configuration space. The function *COLLISION-FREE* still checks the line between each pair of nodes in configuration space since the final commands to the robot will be configuration space moves.

Task space search is probably the most intuitive approach, as one can picture the wheel moving through the three-dimensional grid. In addition, the smaller branching factor (6 instead of 12) means the search space is exponentially smaller than that of CFG, which allows a much finer granularity to be used for the grid.[6]

The smaller search space is also a potential disadvantage of this approach. Recall that function *TO-CSPACE*(xyz_i, leg_j) is one-to-one, even though xyz_i could map to multiple configurations. Recall also that to check an edge (xyz_i, xyz_j) in task space,

---

[4]This order in which nodes are explored distinguishes A* search from other graph-search algorithms, and ensures that the resulting solution will be optimal.

[5]In traditional A* search, *GET-SUCCESSORS* will only return a successor s if *COLLISION-FREE*(n, s) passes. However, a lazy version of A* has been implemented, and is described further in §A.2.6.

[6]For example, doubling the granularity increases the search space size by a factor of 8 for task space, but by a factor of 64 for configuration space.

collisions are still checked in configuration space, using *COLLISION-FREE(TO-CSPACE*(xyz_i)*,TO-CSPACE*(xyz_j)*)*. This test might fail even if there exist other valid configurations for xyz_i and xyz_j for which the edge is collision-free. Therefore, there is the risk that this approach, even with very fine resolution, will fail to find solutions that do exist. In effect, only a portion of the configuration space searched by the other approaches is covered.

A.2.6   Optimization 1: Lazy A* Search

For the complex robot of interest in this work, the computationally expensive piece of each A* implementation is the *COLLISION-FREE* function. This is different than typical A* domains, where the computation of g and/or h are most expensive. Therefore, a lazy version of Algorithm 3 has been implemented that changes two aspects of typical A* search:

1. In typical A*, *GET-SUCCESSORS* only returns a neighbor s if *COLLISION-FREE*(n, s) succeeds. The lazy A* returns all neighbors, and therefore avoids calling *COLLISION-FREE* when a node is added.

2. As a result unreachable nodes are included in *queue*. Therefore, *GET-BEST-NODE*(*queue*), instead of simply returning the top node n in *queue*, must call *COLLISION-FREE*$(n.parent, n)$; if this succeeds n can be returned; if it fails, n is discarded, the next node in *queue* is considered, and so on.

This approach means there will be nodes n in *queue* that cannot be expanded because the path from n's parent has collisions. However, the same point in space with a different parent might expand successfully. Therefore, unlike traditional A*, it may be necessary to add a single point in space to *queue* multiple times; this can only be avoided if the same point has been both added *and* successfully expanded.

As a result, it is not at all obvious that this lazy approach is a good idea. On the one hand, unnecessary checking of edges to nodes that never end up getting expanded is avoided. On the other hand, each point in space could have multiple copies in *queue*, making the maintenance (especially sorting) of *queue* more difficult.

In the worst case, where A* expands all nodes in *queue* before finding a solution, this overhead certainly makes the lazy approach more expensive.

For the experiments described in §A.3, the lazy version of A* is an improvement. In configuration space, between 1.3 and 9.7 (depending on the terrain) times more nodes are added on average, while search times are reduced by 43 to 82 percent on average. Similarly, in task space, between 1.2 and 4.8 times more nodes are added, while search times are reduce by 25 to 70 percent. Nonetheless, lazy A* is not always better; for 4 of the 958 instances considered, the lazy A* version of CFG times out (and therefore fails) even though the standard implementation succeeds.

A.2.7   Optimization 2: Path Smoothing

Because SBL is a random algorithm, and returns the first valid path found, the result can be a very inefficient and odd-looking step. For results to be acceptable to human operators a post-processing algorithm to smooth the resulting path was developed. A smoothing approach similar to the one proposed in [Amin 06] was chosen. The implemented algorithm does the following:

1. Expand *path* into a graph by joining every pair (c_i, c_j) of vertices for which *COLLISION-FREE* (c_i, c_j) succeeds.

2. Run Dijkstra search on this graph to find the shortest path from c_{start} to c_{goal}. This has the effect of cutting off unnecessary corners in the original path.

3. Add vertices to *path* by bisecting each edge.

4. Repeat steps 1 through 3 until the improvement made in a given iteration is less than 10%.

Smoothing is used to improve the paths returned by the A* algorithms as well; although they return optimal paths along the discretized grids, there are usually shorter paths that cut corners and pass diagonally through the grid. The smoothing algorithm in configuration space is outlined in Figure A.2.

Figure A.2: **Path smoothing in a hypothetical 2D C-space:** c_{start} and c_{goal} **are separated by a C-obstacle. (1) Motion plan with** N_1 **nodes before smoothing; (2) shortest path found using Dijkstra's algorithm, with** $N_2 \leq N_1$ **nodes; (3) the simplified path is bisected, adding** $N_2 - 1$ **nodes; (4) Dijkstra's algorithm is re-run.**

A.3 Experimental Setup

To compare algorithms, four different types of terrain were generated. For each, a set, L, of representative points on the left side of the leg was selected, and a similar set, R, on the right. Each possible pair, $(l_i \in L, r_j \in R)$, is then considered and stepping is attempted both from l_i to r_j and vice versa, resulting in $|L| \cdot |R| \cdot 2$ problem instances for each terrain. The four terrains, three of which are shown in Figure A.3, are:

Figure A.3: **The** *Bump*, *Step*, **and** *Well* **terrains used in the experiments.**

- *Flat*: Completely flat terrain ($|L| = |R| = 11$). This serves as a baseline.

- *Bump*: Terrain with a 40 cm bump between L and R ($|L| = |R| = 14$). This is probably the most realistic terrain; stepping with ATHLETE is most likely to be done over rocks in the lunar landscape.

- *Step*: Terrain with a 50 cm ledge; L is at the top of the ledge, and R is at the base ($|L| = 15$, $|R| = 6$).

- *Well*: Terrain with two wheel-sized wells surrounded by raised terrain, where L is in one well and R the other ($|L| = 8$, $|R| = 9$). This terrain attempts to generate a difficult example that is quite different from the other terrains.

This results in a total of 958 problem instances. The algorithms were configured as follows:

- Search fails if a solution is not found within 5 minutes.[7]

- Each A* approach was run with two granularities. $CFG(1.0)$ and $CFG(0.33)$ use 1 radian and 0.333 radians,[8] respectively, while $TSK(0.2)$ and $TSK(0.1)$ use 0.20 m and 0.10 m, respectively. Roughly speaking, the coarser granularity was intended to make the search time comparable to SBL while the finer granularity allows better answers to be found, but more slowly.

- The attempt is made to reach the goal node from a search node in A* (see line 11 in Algorithm 3) if the distance to the goal is less than 2 radians in configuration space, and 40 cm in task space.

- Since each run of SBL produces a different result, an average of the SBL results over 10 runs for each problem instance is used.

---

[7]This seems like a long time to wait for a solution to a single step; that it has been acceptable in practice points out how time-consuming the stepping process currently is.

[8]Note that the high dimensionality of configuration space forces us to use very coarse granularities in this space; 1 radian is almost 60 degrees.

A.4   Experimental Results

Figure A.4 shows the fraction of problem instances solved by each approach. As expected, $SMPL$ often fails and is not really a viable approach. Besides $SMPL$, there are very few failures. SBL and $TSK(0.1)$ succeed on every instance. $TSK(0.2)$ fails on 13 of the $Bump$ instances. $CFG(1.0)$ cannot solve 23 of the 144 $Well$ instances because no solution exists using the coarse grid, while $CFG(0.33)$ times out on 4 of the 180 $Step$ instances.

Figure A.4: **Success ratios.**

Figure A.5 shows average runtimes. These are small on average, with $SMPL$ obviously the fastest, and the finer granularity searches taking generally the longest. One notable exception is the case of the $Well$, where $CFG(1.0)$ is the slowest algorithm. This is almost certainly caused by an increase in the number of collision checks required to find a sequence of large C-Space swings that can maneuver within the constrained space of the well.

Figure A.6 shows the length of the resulting configuration space paths, before and after smoothing.[9] Surprisingly, although $CFG(0.33)$ is best and TSK is worst

---

[9]For the rest of the results presented here, $SMPL$ is excluded; because it only succeeds on the

Figure A.5: **Runtimes, split into search and smoothing times.**

before smoothing, those results are almost completely negated by smoothing, with SBL doing best for three of the four terrains. Smoothing also helps TSK become competitive on this metric, although it still does poorly on the $Bump$ terrain.

Figure A.7 shows the average distances in task space for each approach. Here, $TSK(0.1)$ is the clear winner, outperforming all other algorithms on all data sets, before and after smoothing. Finally, Figure A.8 shows the maximum values for each terrain, confirming that SBL and $CFG(1.0)$ occasionally produced very long paths, even after smoothing.

A.5 Conclusion

This appendix outlined four different algorithms for taking a step with ATHLETE. Three approaches, $SMPL$, SBL, and CFG, search in configuration space while TSK searches in task space. Each algorithm was tried on a total of 958 problem instances spread across 4 types of terrain.

As expected $SMPL$ is extremely fast, but untenable due to its high failure rate.

easiest instances, results for that algorithm are skewed.

Figure A.6: **Configuration space distances.**

Figure A.7: **Task space distances.**

CFG produces short paths in configuration space, but suffers from the high dimensionality of its search space; the fine-grained version can run for minutes on difficult instances, while the faster version is too coarse to get good results.

SBL also runs quickly, but produces a wide range of path lengths in both configuration and task spaces; these variances have been sufficiently eliminated by adequate tuning of the post-SBL smoothing. TSK results are most consistent; the finer grained

Figure A.8: **Maximum distances in task space for each terrain.**

version is the only approach other than SBL to solve all instances, runtimes are comparable to SBL, and configuration space distances are only slightly worse than other methods. TSK consistently get the shortest task space distance, arguably the most important metric.

The results of this work show that SBL with smoothing and TSK are comparable approaches for the planning of steps with 6-DOF legs. All the experiments presented in this dissertation were conducted using SBL with smoothing.

Bibliography

[Alexander 84]   R. Alexander. *The gaits of bipedal and quadrupedal animals.* The International Journal of Robotics Research, vol. 3, no. 2, page 49, 1984.

[Alexander 89]   R. M. Alexander. *Optimization and gaits in the locomotion of vertebrates.* Physiological Reviews, vol. 69, no. 4, page 1199, 1989.

[Altendorfer 01]   R. Altendorfer, N. Moore, H. Komsuoglu, M. Buehler, H. B. Brown, D. McMordie, U. Saranli, R. Full & D. E. Koditschek. *Rhex: A biologically inspired hexapod runner.* Autonomous Robots, vol. 11, no. 3, pages 207–213, 2001.

[Amin 06]   J. N. Amin, J. D. Boskovic & R. K. Mehra. *A Fast and Efficient Approach to Path Planning for Unmanned Vehicles.* In AIAA Guidance, Navigation, and Control Conference and Exhibit, pages 20–22, 2006.

[Bessonov 73]   A. P. Bessonov & N. V. Umnov. *The analysis of gaits in six-legged vehicles according to their static stability.* In Proc. Symp. Theory and Practice of Robots and Manipulators, 1973.

[Blackman 10]   Christine Blackman. *Stanford's robotic Audi to brave Pikes Peak without a driver.* http://news.stanford.edu/news/2010/february1/shelley-pikes-peak-020310.html, February 2010.

[Boyd 04]   S. P. Boyd & L. Vandenberghe. Convex optimization. Cambridge Univ Pr, 2004.

[Bretl 05]   Timothy Bretl. *Multi-Step Motion Planning: Application to Free-Climbing Robots.* PhD dissertation, Stanford University, 2005.

[Bretl 06]   Timothy Bretl. *Motion Planning of Multi-Limbed Robots Subject to Equilibrium Constraints: The Free-Climbing Robot Problem.* The International Journal of Robotics Research, vol. 25, pages 317–342, 2006.

[Buckley 07]   David Buckley. *History Makers - 1868 Dederick's Steam Man.* http://www.davidbuckley.net/DB/HistoryMakers.htm, 2007.

[Cheng 91]   F. T. Cheng & D. E. Orin. *Optimal force distribution in multiple-chain robotic systems.* IEEE Transactions on Systems, Man and Cybernetics, vol. 21, no. 1, pages 13–24, 1991.

[Cobano 08]   J. A. Cobano, R. Ponticelli & P. G. de Santos. *Mobile robotic system for detection and location of antipersonnel land mines: field tests.* Industrial Robot: An International Journal, vol. 35, no. 6, pages 520–527, 2008.

[Collins 07]   C. Collins. *Stiffness Modeling and Force Distribution for the All-Terrain, Hex-Limbed Extra-Terrestrial Explorer (ATHLETE).* In Proc. ASME 2007 International Design Engineering Technical Conferences & Computers and Information in Engineering Conference, Las Vegas, Nevada, USA, 2007.

[Cox 70]   W. Cox. *Big muskie.* The Ohio State Engineer, pages 25–52, 1970.

[Craig 89]   J. J. Craig. Introduction to robotics: Mechanics and control. AddisonWesley, 2nd edition, 1989.

[de Santos 05]   P. Gonzalez de Santos, J. Estremera, E. Garcia & M. Armada. *Including joint torques and power consumption in the stability margin*

of walking robots. Autonomous Robots, vol. 18, no. 1, pages 43–57, 2005.

[de Santos 06] P. Gonzalez de Santos, E. Garcia & J. Estremera. Quadrupedal locomotion: An introduction to the control of four-legged robots. Springer-Verlag New York, Inc. Secaucus, NJ, USA, 2006.

[Debunne. 09] Gilles Debunne. *libQGLViewer.* http://www.libqglviewer.com/, 2009.

[Dederick 68] Zadoc Dederick & Isaac Grass. *Improvement in Steam-Carriage, United States Patent 75874*, March 1868.

[Erden 06] M. S. Erden & K. Leblebicioglu. *Analysis of Wave Gaits for Energy Efficiency.* Signal Processing and Communications Applications, 2006 IEEE 14th, pages 1–4, 2006.

[Erden 07] M.S. Erden & K. Leblebicioglu. *Torque Distribution in a Six-Legged Robot.* Robotics, IEEE Transactions on, vol. 23, no. 1, pages 179–186, 2007.

[Fu 87] K. S. Fu, R. C. Gonzalez & C. S. G. Lee. Robotics: control, sensing, vision, and intelligence. McGraw-Hill, Inc. New York, NY, USA, 1987.

[Full 02] R. Full. *Unlocking the Secrets of Animal Locomotion.* http://berkeley.edu/news/media/releases/2002/09/rfull/locomotion.html, 2002.

[Gabrielli 50] G. Gabrielli & T. Von Karman. *What price speed.* Mechanical Engineering, vol. 72, no. 10, page 775781, 1950.

[Garcia 02] Elena Garcia, Joaquin Estremera & Pablo Gonzalez de Santos. *A comparative study of stability margins for walking machines.* Robotica, vol. 20, pages 595–606, 2002.

[Gill 02]   P. E. Gill, W. Murray & M. A. Saunders. *SNOPT: An SQP algorithm for large-scale constrained optimization.* SIAM Journal on Optimization, vol. 12, no. 4, pages 979–1006, 2002.

[Gottschalk 96]   S. Gottschalk, M. C. Lin & D. Manocha. *OBBTree: A hierarchical structure for rapid interference detection.* In Proceedings of the 23rd annual conference on Computer graphics and interactive techniques, pages 171–180. ACM, 1996.

[Gregorio 97]   P. Gregorio, M. Ahmadi, M. Buehler, S. B. Design & Q. Montreal. *Design, control, and energetics of an electrically actuated legged robot.* Systems, Man and Cybernetics, Part B, IEEE Transactions on, vol. 27, pages 626–634, 1997.

[Hauser 08a]   K. Hauser. *Motion Planning for Legged and Humanoid Robots.* PhD dissertation, Stanford University, Stanford, CA, September 2008.

[Hauser 08b]   K. Hauser, T. Bretl, J. C. Latombe, K. Harada & B. Wilcox. *Motion planning for legged robots on varied terrain.* The International Journal of Robotics Research, vol. 27, no. 11-12, page 1325, 2008.

[Heiken 91]   G. Heiken, D. Vaniman & B. M. French. Lunar sourcebook, a user's guide to the moon. Cambridge University Press, 1991.

[Hildebrand 65]   M. Hildebrand. *Symmetrical Gaits of Horses.* Science, vol. 150, pages 701–708, 1965.

[Hirose 85]   S. Hirose, T. Masui, H. Kikuchi, Y. Fukuda & Y. Umetani. *Titan III: A quadruped walking vehicle.* In Robotics Research-The Second International Symposium, page 325331, 1985.

[Hirose 91]   S. Hirose, K. Yoneda, K. Arai & T. Ibe. *Design of prismatic quadruped walking vehicle TITAN VI.* In Fifth International Conference on Advanced Robotics, 1991.'Robots in Unstructured Environments', 91 ICAR., pages 723–728, 1991.

[Hirose 95]   S. Hirose & H. Takeuchi. *Roller-walker: A proposal of new leg-wheel hybrid mobile robot.* In Proceedings of the International Conference on Advanced Robotics, page 917922, 1995.

[Hirose 98]   S. Hirose & K. Kato. *Quadruped walking robot to perform mine detection and removal task.* In Proceedings of the 1st International Conference on Climbing and Walking Robots, Brussels, Belgium, pages 261–6, 1998.

[Hirose 99]   S. Hirose & K. Arikawa. *Development of quadruped walking robot TITAN-VIII for commercially available research platform.* Journal of the Robotics Society of Japan, vol. 17, no. 8, pages 1191–1197, 1999.

[Hirose 01]   S. Hirose, H. Tsukagoshi & K. Yoneda. *Normalized energy stability margin and its contour of walking vehicles on rough terrain.* In Proceedings, IEEE International Conference on Robotics and Automation, 2001., volume 1, 2001.

[Jiang 04]   W. Y. Jiang, A. M. Liu & D. Howard. *Optimization of legged robot locomotion by control of foot-force distribution.* Transactions of the Institute of Measurement & Control, vol. 26, no. 4, page 311, 2004.

[Kar 01]   D. C. Kar, K. Kurien Issac & K. Jayarajan. *Minimum energy force distribution for a walking robot.* Journal of Robotic Systems, vol. 18, no. 2, 2001.

[Kato 73]   I. Kato. *Development of WABOT 1.* Biomechanisms, pages 173–214, 1973.

[Kato 01]   K. Kato & S. Hirose. *Development of the quadruped walking robot, TITAN-IX mechanical design concept and application for the humanitarian de-mining robot.* Advanced Robotics, vol. 15, no. 2, pages 191–204, 2001.

[Kerr 86]   Jeffrey Kerr & Bernard Roth. *Analysis of Multifingered Hands.* The International Journal of Robotics Research, vol. 4, no. 4, pages 3–17, January 1986.

[Kugushev 75]   E. I. Kugushev & V. S. Jaroshevskij. *Problems Op Selecting a Gait for an Integrated Locomotion Robot.* In Fourth International Conference on Artificial Intelligence, pages 789–793, Tbilisi, Georgia, USSR, 1975.

[Kumar 89]   V. R. Kumar & K. J. Waldron. *A review of research on walking vehicles.* In The robotics review 1, page 266. MIT Press, 1989.

[Kumar 90]   V. Kumar & K. J. Waldron. *Force distribution in walking vehicles.* Journal of Mechanical Design, vol. 112, page 90, 1990.

[Kurazume 03]   R. Kurazume, A. Byong-won, K. Ohta & T. Hasegawa. *Experimental study on energy efficiency for quadruped walking vehicles.* In 2003 IEEE/RSJ International Conference on Intelligent Robots and Systems, 2003.(IROS 2003). Proceedings, volume 1, 2003.

[Larsen 99]   E. Larsen, S. Gottschalk, M. C. Lin & D. Manocha. *Fast proximity queries with swept sphere volumes.* 1999.

[Li 09]   C. Li, P. B. Umbanhowar, H. Komsuoglu, D. E. Koditschek & D. I. Goldman. *Sensitive dependence of the motion of a legged robot on granular media.* Proceedings of the National Academy of Sciences, vol. 106, no. 9, page 3029, 2009.

[Liu 07]   J. Liu, M. Tan & X. Zhao. *Legged robots–an overview.* Transactions of the Institute of Measurement & Control, vol. 29, no. 2, page 185, 2007.

[LLC 08]   Harmonic Drive LLC. *Ultra Flat SHD Series Gearheads.* http://www.harmonicdrive.net/products/gearheads/shd-gearheads/, 2008.

[Marhefka 97]   D. W. Marhefka & D. E. Orin. *Gait planning for energy efficiency in walking machines.* In 1997 IEEE International Conference on Robotics and Automation, 1997. Proceedings., volume 1, 1997.

[Marhefka 98]   D. W. Marhefka & D. E. Orin. *Quadratic optimization of force distribution in walking machines.* In 1998 IEEE International Conference on Robotics and Automation, 1998. Proceedings, volume 1, 1998.

[McGhee 67]   R. B. McGhee. *Finite state control of quadruped locomotion.* Simulation, vol. 9, no. 3, page 135, 1967.

[McGhee 68a]   R. B. McGhee. *Some finite state aspects of legged locomotion.* Mathematical Biosciences, vol. 2, pages 67–84, 1968.

[McGhee 68b]   R. B. McGhee & A. A. Frank. *On the stability properties of quadruped creeping gaits* 1.* Mathematical Biosciences, vol. 3, no. 3-4, pages 331–351, 1968.

[McGhee 79]   R. B. McGhee & G. I. Ishwandi. *Adaptive locomotion of a multilegged robot over rough terrain.* IEEE Transactions on Systems, Man, and Cybernetics, vol. 9, pages 176–182, 1979.

[McGhee 85a]   R. B. McGhee. *Vehicular legged locomotion.* Advances in Automation and Robotics, vol. 1, pages 259–284, 1985.

[McGhee 85b]   R. B. McGhee, D. E. Orin, D. R. Pugh & M. R. Patterson. *A Hierarchically Structured System for Computer Control of a Hexapod Walking Machine.* In Theory and practice of robots and manipulators: proceedings of RoManSy'84, the Fifth CISM-IFToMM Symposium, page 375. The MIT Press, 1985.

[Messuri 85]   D. A. Messuri & C. A. Klein. *Automatic body regulation for maintaining stability of a legged vehicle during rough-terrain locomotion.*

IEEE Journal of Robotics and Automation, vol. 1, pages 132–141, 1985.

[Miller 06]   Teresa Miller, Timothy Bretl & Stephen Rock. *Control of a Climbing Robot Using Real-Time Convex Optimization.* In Symposium on Mechatronic Systems, Heidelberg, Germany, 2006.

[Morrison 68]   R. A. Morrison. *Iron Mule Train.* In Mobility testing: proceedings of the off-road Mobility Research Symposium, page 381. Cornell Aeronautical Laboratories, 1968.

[Mosher 68]   R. S. Mosher. *Test and evaluation of a versatile walking truck.* In Mobility testing: proceedings of the off-road Mobility Research Symposium, page 359. Cornell Aeronautical Laboratories, 1968.

[Muybridge 87]   E. Muybridge. *Animal locomotion.* University of Pennsylvania, 1887.

[Muybridge 57]   E. Muybridge. Animals in motion. Dover Publications, 1957.

[Nash 96]   S. G. Nash, A. Sofer & J. R. Shinnerl. Linear and nonlinear programming. McGraw-Hill New York, 1996.

[Nokia 09]   Nokia. *Qt - A cross-platform application and UI framework.* http://qt.nokia.com/, 2009.

[Okhotsimski 79]   D. E. Okhotsimski, V. S. Gurfinkel, E. A. Devyanin & A. K. Platonov. *Integrated Walking Robot.* Machine intelligence, page 313, 1979.

[Okhotsimski 80]   D. E. Okhotsimski. *Motion control system development for a mobile robot.* Automatic control in space, pages 251–256, 1980.

[Petternella 74]   M. Petternella, S. Salinari, N. delle Ricerche & V. Eudossiana. *Feasibility Study on Six-legged Walking Robots.* In Proceedings, page 33. IIT Research Institute., 1974.

[Playter 06]   R. Playter, M. Buehler & M. Raibert. *BigDog*. In Proceedings of SPIE, volume 6230, page 62302O, 2006.

[Russell 09]   S. J. Russell & P. Norvig. Artificial intelligence: a modern approach. Prentice hall, 2009.

[Rygg 93]   Lewis A. Rygg. *Mechanical Horse, United States Patent 491927*, February 1893.

[Sanchez 01]   G. Sanchez & J. C. Latombe. *A single-query bi-directional probabilistic roadmap planner with lazy collision checking*. In Int. Symp. Robotics Research, pages 403–417. Springer, 2001.

[Siciliano 08]   B. Siciliano & O. Khatib. Springer handbook of robotics. Springer-Verlag New York Inc, 2008.

[Silva 03]   M. F. Silva, J. A. T. Machado & A. M. Lopes. *Comparison of fractional and integer order control of an hexapod robot*. Proceedings of the VIB, 2003.

[Silva 05]   M. F. Silva, J. A. T. Machado & A. M. Lopes. *Modelling and simulation of artificial locomotion systems*. Robotica, vol. 23, no. 05, pages 595–606, 2005.

[Silva 06]   M. F. Silva, J. A. T. Machado & A. M. Lopes. *Energy Efficiency of Quadruped Gaits*. In Climbing And Walking Robots: Proceedings of the 8th International Conference on Climbing and Walking Robots and the Support Technologies for Mobile Machines (CLAWAR 2005), page 735. Springer, 2006.

[Silva 07]   M. F. Silva & J. A. T. Machado. *Kinematic and dynamic performance analysis of artificial legged systems*. Robotica, vol. 26, pages 19–39, 2007.

[Smith 07]   R. Smith. *Open Dynamics Engine*. http://www.ode.org/, 2007.

[Smith 09]   T. B. Smith & D. Chavez-Clemente. *A Practical Compari-son of Motion Planning Techniques for Robotic Legs in Environ-ments with Obstacles.* In Proceedings of the Third IEEE Inter-national Conference on Space Mission Challenges for Information Technology-Volume 00, pages 155–162. IEEE Computer Society, 2009.

[Solnit 04]   Rebecca Solnit. River of shadows: Eadweard muybridge and the technological wild west. Penguin (Non-Classics), March 2004.

[Song 89]   S. M. Song & K. J. Waldron. Machines that walk: The adaptive suspension vehicle. Mit Press, 1989.

[Sun 74]   S. S. Sun. *A Theoretical study of gaits for legged locomotion sys-tems.* PhD thesis, Ohio State University., 1974.

[Tomovic 61]   R. Tomovic & W. J. Karplus. *Land Locomotion Simulation and Control.* Proceedings Third International Analogue Computation Meeting, Opatija, Yugoslavia, pages 385–390, 1961.

[Tsujita 04]   K. Tsujita, M. Kawakami & K. Tsuchiya. *A study on optimal gait pattern of a quadruped locomotion robot.* In 2004 IEEE Interna-tional Conference on Systems, Man and Cybernetics, volume 1, 2004.

[UNC 99]   UNC.   *PQP   -   A   Proximity   Query   Package.* http://gamma.cs.unc.edu/SSV/, 1999.

[Vukobratovic 04] M. Vukobratovic & B. Borovac. *Zero-moment point-thirty five years of its life.* International Journal of Humanoid Robotics, vol. 1, pages 157–173, 2004.

[Waldron 86a]   K. Waldron. *Force and motion management in legged locomotion.* IEEE Journal of Robotics and Automation, vol. 2, no. 4, pages 214–220, 1986.

[Waldron 86b]   K. Waldron & R. McGhee. *The Adaptive Suspension Vehicle.* IEEE Control Systems Magazine, vol. 6, no. 6, pages 7–12, 1986.

[Wheeler 10]   D. Wheeler, D. Chvez-Clemente & V. SunSpiral. *FootSpring: A Compliance Model for the ATHLETE Family of Robots.* In Proc. of the 10th International Symposium on Artificial Intelligence, Robotics and Automation in Space (i-SAIRAS), Sapporo, Japan, August 2010.

[Wilcox 07]   B. H. Wilcox, T. Litwin, J. Biesiadecki, J. Matthews, M. Heverly, J. Morrison, J. Townsend, N. Ahmad, A. Sirota & B. Cooper. *Athlete: A cargo handling and manipulation robot for the moon.* Journal of Field Robotics, vol. 24, pages 421–434, 2007.

[Zielinska 04]   Teresa Zielinska. *Development of Walking Machines: Historical Perspective.* In International Symposium on History of Machines and Mechanisms, pages 357–370. Springer Netherlands, 2004.

[Zoppi 06]   Zoppi & Molfino. *Equilibrium analysis of multi-limbs walking and climbing robots.* Autonomous Robots, vol. 21, pages 199–210, November 2006.